



Tomas Bata University in Zlín

Faculty of Technology

Doctoral thesis

Preparation and characterisation of fillers for polymer nanocomposite layers usable in electronics

Author: **Thaiskang Jamatia, M.Sc.**

Degree programme: P 2808 Chemistry and Materials Technology

Degree course: 2808V006 Technology of Macromolecular Compounds

Supervisor: Assoc. Prof. Ing. et Ing. Ivo Kuřitka, Ph.D. et Ph.D.

Consultants: Mgr. David Škoda, Ph.D.
Assoc. Prof. Ing. Jarmila Vilčáková, Ph.D.

Zlín, September 2020

© Thaiskang Jamatia

ACKNOWLEDGEMENT

I am very thankful to my supervisor Assoc. Prof. Ivo Kuřitka, Ph.D. et Ph.D., for his continual guidance, patience and opportunity for the doctoral study at the Centre of Polymer Systems (CPS) and the Faculty of Technology (FT), Tomas Bata University in Zlin. The unending support, advice, knowledge etc., I received from him was very helpful throughout my doctoral study. Most importantly, the time spent with him for the discussion, expertise and ideas of the research work was invaluable.

My sincere gratitude to my consultant David Škoda, Ph.D., for his directions and opinions on experimentations, characterisations and interpretations of various data. Assoc. Prof. Jarmila Vilčáková, Ph.D. is acknowledged for consultations in the field of electrical property measurements. I would also extend my gratitude to my group members Pavel Urbánek, Ph.D., for various spectroscopic analysis, Lukáš Münster, Ph.D., for TEM analysis, and especially to Jakub Ševčík, Ph.D., for the fabrication of the diodes and investigations of the prepared PLED devices. I thank Lukáš Kalina, Ph.D., Brno University of Technology, for analysing some of the samples using X-ray photoelectron spectroscopy (XPS). Further, I extend my gratitude to the rest of the group members. Special thanks to Prof. Dr. Markus Niederberger, ETH Zurich, for allowing me to work in his research lab for two months.

I am much obliged to my family for their unending love, care and support right from the beginning until the completion of my doctoral study. I also thank my friends and colleagues for their help. I enjoyed my time with them in the laboratories, and I consider myself blessed to be a part of the Multifunctional Nanomaterials research group.

Finally, I am thankful to the funding agencies Ministry of Education, Youth and Sports of the Czech Republic - Program NPU I (LO1504) and Internal Grant Agency of Tomas Bata University in Zlin IGA/CPS/2017/008, IGA/CPS/2018/007 and IGA/CPS/2019/007, without which the work would not proceed.

CONTENT

ABSTRACT/Keywords	3
ABSTRAKT/Klíčová slova	4
1. INTRODUCTION	5
1.1 Research motivation.....	5
1.2 Liquid-phase synthesis of metal oxide nanoparticles	6
1.3 Microwave synthesis of nanoparticles	11
1.4 Band gap engineering.....	13
1.5 Surface modification	14
1.6 Nanocomposite and device preparation	15
2. AIMS OF THE DOCTORAL THESIS.....	19
3. EXPERIMENTAL METHODS AND INSTRUMENTATIONS.....	20
3.1 Analytical techniques	20
3.2 Materials.....	24
3.3 Synthesis of undoped ZnO, the role of water and capping agent ...	25
3.4 Synthesis of doped ZnO	28
3.5 Fillers in a conjugate polymer.....	29
3.6 PLED device fabrication	30
4. RESULTS AND DISCUSSIONS	31
4.1 Undoped ZnO nanoparticles, the role of water and capping agent..	31
4.2 ZnO nanoparticles with different precursor molar concentration....	38
4.3 Fe-doped ZnO nanoparticles.....	49
4.4 Al-doped ZnO nanoparticles.....	62
4.5 PLEDs as proof-of-concept.....	72
5. CONCLUSION	82
CLOSING REMARKS	86
REFERENCES	88
LIST OF TABLES	107
LIST OF FIGURES	108
LIST OF ABBREVIATIONS.....	111
LIST OF SYMBOLS	113
CURRICULUM VITAE.....	115
LIST OF PUBLICATIONS	117

ABSTRACT

The work centred on the one-pot microwave-assisted polyol synthesis of undoped and Fe- and Al-doped ZnO nanoparticles from zinc acetate precursor diethylene glycol (DEG) solution in 15 minutes. The microwave reactor is advantageous over conventional heating due to its rapid and uniform heating of the reaction mixtures. The main advantage of the polyol synthesis is its ability to reduce metal ions and passivation of surface defects in ZnO nanoparticles. The roles of small stoichiometric amounts of water and oleic acid (OA) as a capping agent in the synthesis were studied. The average particle size of undoped ZnO nanoparticles increases with the addition of multiples of equivalent amounts of water to the precursor solution. Also, the addition of the long-chain organic ligand, OA, yielded well-dispersed products without agglomerations. Moreover, it allowed fine dispersion of ZnO and doped ZnO nanoparticles in toluene which is necessary for the preparation of nanocomposites.

Doping of the ZnO nanoparticles was carried out for altering the band gap of the semiconductor nanoparticles to modify its optical and electronic properties. Fe^{3+} source ions were reduced to Fe^{2+} ions, and incorporated to the host crystal lattice of nanoparticles. This p-doping decreased the UV luminescence intensity of the host nanoparticles. Addition of Al^{3+} ion source to the reaction mixture resulted in n-doping of the host nanoparticles imparting them enhanced UV luminescent intensity.

The particle crystallinity and size of the nanocrystallites were analysed by X-ray diffraction (XRD), and transmission electron microscopy (TEM) images confirmed the morphology and size of the nanoparticles produced. Ultraviolet-visible spectroscopy (UV-Vis) and fluorescence measurement were conducted to analyse the optical properties of the nanoparticles. Diffuse reflectance (DR) UV-Vis measured the reflectance, and the band gap was estimated by Tauc plot. Brus' model was utilised to study the relation between the size of the semiconductor nanoparticles and its electronic structure.

Finally, polymer light-emitting diodes (PLEDs) were prepared to demonstrate the ability of the tailored nanoparticles as fillers for polymer-matrix nanocomposite-based electronic devices. The dispersions of pure or variously doped ZnO nanoparticles in toluene solutions of poly[2-methoxy-5-(2'-ethylhexyloxy)-1,4-phenylene vinylene] (MEH-PPV) were spin-cast to obtain thin nanocomposite films serving as emissive layers in PLEDs. Electroluminescence (EL) was increased by the introduction of the nanoparticles. Specifically, Fe-doping decreased the opening bias while Al-doping enhanced the EL intensity greatly. Moreover, the chromaticity characteristics were improved by nanoparticles addition as well.

Keywords: microwave, polyol, zinc oxide, doping, nanoparticles, MEH-PPV, nanocomposites, polymer light-emitting diode.

ABSTRAKT

Práce se soustředí na jednokrokovou mikrovlnami asistovanou polyolovou syntézu nedopovaných a Fe- a Al-dopovaných nanočástic ZnO z octanu zinečnatého jako prekurzoru rozpuštěného v diethylen glykolu, která trvá vždy jen 15 minut. Mikrovlnný reaktor je výhodnější než konvenční, díky rychlosti a uniformitě ohřevu reakční směsi. Hlavní výhodou polyolové syntézy je schopnost redukovat ionty kovů a pasivace defektů na povrchu ZnO nanočástic. Byla studována role malých stechiometrických množství vody, a také kyseliny olejové (OA) jako povrch modifikujícího činidla, při syntéze. Průměrná velikost částic nedopovaného ZnO vzrůstá s přidáním násobků molárně ekvivalentního množství vody do roztoku prekurzoru. Přídavek organického ligandu s dlouhým řetězcem, OA, vedl ke vzniku dobře dispergovaného produktu bez aglomerátů, navíc to umožňuje připravit disperze nanočástic ZnO (dopovaných i nedopovaných) v toluenu, což je nutné pro přípravu nanokompozitů.

Dopování ZnO nanočástic bylo prováděno kvůli modifikaci zakázaného pásu polovodičových nanočástic pro úpravu jejich optických a elektronických vlastností. Fe^{3+} iony ze zdrojové soli se redukovaly na Fe^{2+} a byly přijaty do hostitelské krystalové mřížky nanočástic. Toto p-dopování potlačilo intenzitu UV luminiscence nanočástic. Přídavek zdroje Al^{3+} do reakční směsi vedl k n-dopování hostitelských nanočástic a nárůstu intenzity jejich UV luminiscence.

Krystalinita a velikost nanokrystalitů byly analyzovány rentgenovou difraktometrií (XRD) a transmisí elektronová mikroskopie (TEM) ověřila morfologii a velikost připravených nanočástic. Optické vlastnosti nanočástic byly analyzovány spektrometrií v ultrafialové a viditelné oblasti (UV-Vis) a měřeními fluorescence. Difuzně reflektanční (DR) UV-Vis měření reflektance umožnilo stanovení šířky zakázaného pásu z Taucova grafu. Brusova rovnice byla využita jako model pro studium vztahu velikosti nanočástice a jejich elektronické struktury.

Naposledy byly vybrány polymerní světlo emitující diody (PLED) jako příkladné elektronické prvky, aby se na nich demonstrovaly účinky tailorovaných nanočástic jako plniv pro nanokompozity s polymerní maticí pro využití v elektronice. Disperze čistých nebo různě dopovaných ZnO nanočástic v toluenových roztocích poly[2-methoxy-5-(2'-ethylhexyloxy)-1,4-fenylene vinylene] (MEH-PPV) byly nanášeny rotačním litím tak, aby se připravila tenká nanokompozitní vrstva sloužící po dohotovení přípravku jako samotná emisní vrstva v PLED. Intenzita elektroluminiscence se přidáním nanočástic do aktivní vrstvy zvyšovala. Přídavek Fe-dopovaných nanočástic snížil otevírací napětí diod, zatímco přídavek Al-dopovaných nanočástic zvýšil intenzitu EL. Navíc byly přidáním nanočástic vylepšeny chromatické charakteristiky diod.

Klíčová slova: mikrovlny, polyol, oxid zinečnatý, dopování, nanočástice, MEH-PPV, nanokompozit, polymerní světlo emitující dioda.

1. INTRODUCTION

1.1 Research motivation

Nanoscience is the study of matter at the nanometre range ($1 \text{ nm} = 10^{-9} \text{ m}$). The scale of nanometre ranges from 1 to 100 nm. At this length, a material tends to have physical and chemical characteristics related to its size. Moreover, the classical Newtonian mechanics is not applicable; instead, it is the quantum mechanical system, which is at play here. It was in 1971 the term nanotechnology was coined by Norio Taniguchi. However, the idea was conceptualised in 1959 by Richard Feynman at an American Physical Society meeting in Caltech. One of the main reasons why the study of matter at the molecular and atomic level is important is due to its high surface-to-volume ratio. This phenomenon should not be surprising when materials at nanometre range display chemical and physical properties different from the bulk materials. It is due to the relatively larger surface area to the volume that the surface of a nanoparticle is more exposed, resulting in its high chemical reactivity. One of the examples being the different colours gold (Au) nanoparticles possess at different nanometre dimensions. In this context, the same Au nanoparticles with different sizes exhibit different colours, Fig. 1.1.



Fig. 1.1 Colloidal Au nanoparticle with different particle sizes [1].

Nanoscience and nanotechnology are found in various fields of science and technology due to its cutting-edge applications in medicines [2], gas sensing [3], agriculture [4], food packaging [5] etc. In the past few decades, there has been an increasing number of ongoing research of the semiconductor nanoparticles. As stated earlier, in the nanometre range (1-100 nm), materials behave differently from the bulk. The same nanomaterial exhibit different properties based on the size and shape of the nanomaterials; it is due to this fact, there are numerous researches in the field of semiconductor nanomaterials in both academia and industries. The semiconductor nanocrystals exhibit size-dependent properties. When the dimension of bulk material is reduced to nanometre range (1-100 nm), quantum confinement is achieved. As a result, the density of the electronic states becomes discrete at the edges of the band structure, resulting in the alteration of the electrical and optical properties of the bulk material [6].

In order to tap or harness these potentials of nanomaterials, researchers have continuously worked on the control and manipulation of preparation of nanocrystals with varied shapes and sizes [7–10]. There are fundamentally two different approaches to nanoparticle synthesis, top-down and bottom-up techniques. In the first method, external energy is employed to breakdown material into small particles of nanometre dimensions. Ball milling is one such example of a top-down technique for nanoparticle synthesis. Further, in the field of nanoelectronics, a high-energy electron beam is targeted onto a sample, e-beam lithography, to etch out unwanted materials or particles; it reduces the material to a nanometre dimension. This technology is widely concentrated on lithographic patterning. The bottom-up technology utilises physical and chemical forces for the synthesis of nanoparticles. The gaseous phase method of preparation involves chemical vapour deposition (CVD) and physical vapour deposition (PVD). These methods minimise the formation of organic side-products. However, the requirement of vacuum environment renders these deposition techniques expensive. Besides that, wet-chemical synthesis has attracted the most number of attentions due to its relatively simplistic and economical approach, Fig. 1.2. Here, the chemical reduction of reaction precursors by thermal decomposition is widely used. Several kinds of metal and metal oxide nanoparticles have been synthesised by this synthesis procedure [11–14]. In principle, it is the chemical reduction of metal precursors at an elevated temperature where metal ions is reduced to 0 oxidation states (e.g. Zn^{2+} to Zn^0). Additionally, the surface of synthesised nanocrystals can be coated by long-chain organic molecules or polymers during or after the synthesis. This is carried out to achieve monodisperse particles in liquid media [15, 16]. These surfactants form layers on the nanocrystals and further prevent agglomerations and provide colloidal stability. The other important roles played by them are- stopping uncontrolled growth of nanoparticles, and they are also key to achieving different morphologies of nanocrystals like nanorods, nanowires, nanocubes etc. [17–21].

Doping is the addition of impurities to a crystal lattice for altering and manipulating the optical and electrical properties of a nanocrystal. Depending upon the requirement and applications of synthesised nanocrystals, doping levels can be achieved. The colloidal nanocrystals can then be further processed into blending with a conjugated polymer. This nanocomposite solution is used in the fabrication of organic electronics such as polymer light-emitting diodes (PLEDs), organic photovoltaics (OPVs) [22–25].

1.2 Liquid-phase synthesis of metal oxide nanoparticles

The liquid-phase synthesis of nanomaterials is a widely used method mainly due to its processibility and reproducibility. Nucleation and growth are the two basic steps in the wet-chemical synthesis of nanoparticles. Knowledge regarding the mechanism for the synthesis of nanoparticles is crucial in regulating the size and morphology. However, for several reaction systems, the mechanism is not

understood unambiguously. Many theories like LaMer mechanism, Ostwald and Digestive ripening and Finke-Watzke two-step mechanism have been proposed to explain the nucleation and growth of nanoparticles in a solution [26–29]. In addition, the concentration of the metal precursor is vital for nanoparticle synthesis. After the concentration of the precursor reaches a supersaturation, nucleation process occurs up to a critical value. It is then followed by the growth of the nuclei via diffusion of the monomers in the solution.

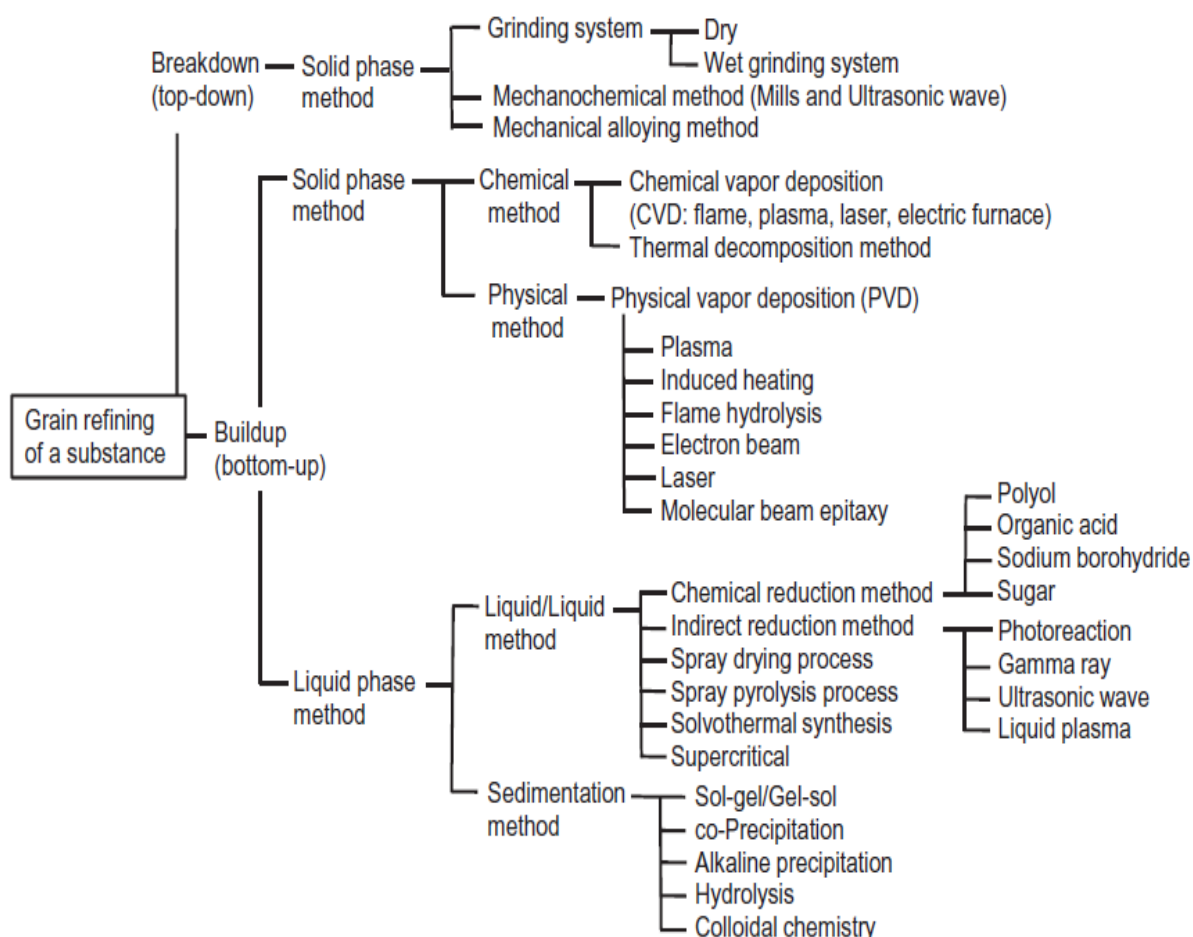


Fig. 1.2 Top-down and bottom-up approaches of nanoparticle synthesis [30].

As briefly mentioned earlier, the synthetic route offers a wide range of versatility in controlling, to some extent, the size and morphology of the synthesised nanoparticles. In order to achieve that, the reaction parameters play a vital role in engineering the desired characteristics of the nanocrystals. Several liquid-phase synthesis methods are available in the literature like, co-precipitation method [31, 32], hydrothermal [33, 34], solvothermal [35, 36], sol-gel [37, 38], polyol [39, 40]. These synthetic methods produce nanoparticles with high crystallinity as the reaction is conducted at the high-temperature condition.

Following works can be reminded in closer detail to exemplify the variability of above-mentioned methods. Kumaresan *et al.* hydrothermally grew ZnO nanoparticles at a high temperature, (150 °C) the reaction for 3 hours [41]. By varying the pH of the reaction conditions, spindle-like, hexagonal disk, porous nanorods and flower-like structures were obtained. The photocatalytic activity of the prepared samples was investigated for Rhodamine B (RhB) dye that displayed 94 % degradation and good stability for five cycles. The solvothermal synthesis of nanoparticles is an established technique for preparing metals, metal oxides and metal-organic frameworks. Unlike hydrothermal synthesis, where water is the solvent, and high boiling point organic solvent is used in the solvothermal method. A facile solvothermal synthesis of Zn-doped Fe₃O₄ was carried out by Liu *et al.* The magnetic and thermodynamic effects of the doped nanoparticles at different molar concentrations of Zn was studied. The average particle size from TEM analysis was in 11 to 24 nm range. One of the highlights of the work was a thermodynamic investigation of the doped magnetic nanoparticles. The results suggested that at low temperatures, the ferromagnetic characteristic changes to antiferromagnetic with increased doping from 0 to 1 [42].

In another work, phosphorus-doped LaFeO_{3-δ} perovskite oxide was synthesised by Cao *et al.* The research group used the citric sol-gel method, and both ethylene glycol and polyethylene glycol were separately used as a solvent. The investigation was also carried out by experimenting at different calcination temperatures. The doped perovskite oxide was used to study its ethanol sensing properties [43]. The research group headed by Fievet *et al.* first developed the polyol synthesis of metal powders in micrometre and submicrometre size range in 1989 [44]. The pioneering work by this research group developed in the late twentieth century attracted the metal-synthetic industry as this new technique was found to reduce ions of noble metals. The polyol technique is also widely used in the preparation of highly crystalline and monodisperse nanoparticles without subsequent thermal treatment. Ramamoorthy *et al.* investigated the growth of Co nanoparticles synthesised by one-pot polyol synthesis technique [45]. The growth of the obtained ferromagnetic nanoparticles was investigated by heterogeneous nucleation process; iridium or ruthenium chloride was the nucleating agent used.

With regard to the ZnO based nanoparticle systems studied in this work, synthesis of undoped ZnO nanopowders and its doped counterparts with modified band gap is of special interest. Zinc oxide (ZnO) is a versatile semiconductor nanoparticle material attracting many researchers. The wide direct bandgap (3.3 eV) and large excitons binding energy at room temperature (60 meV) enable it to be applicable for many applications. Moreover, the optical and electrical properties of the nanoparticle can be tuned by the addition of impurity into the ZnO crystal structure. Doping ZnO with different types of elements opens up more possibilities of tuning its characteristics and fitting it with the applications accordingly. Metals as dopants for ZnO have drawn interests due to its relative simplicity and versatility that has found application:

a) Transition metals

There are works reported in the literature when ZnO nanoparticle was doped with transition metal atoms (Fe, Co, Ni, Cr, V, etc.) [46–52]. In addition, ZnO doped with these metals have found applications in optoelectronic devices [53], solar cells [54], gas sensors [55], etc. On top of that, doping of ZnO with transition metal ions is due to its thermal and chemical stability. Doping with iron seems to be the most efficient.

b) p-block metals

Doping ZnO semiconductor nanoparticle with trivalent (Al^{3+} , Ga^{3+} and In^{3+}) atoms from the 13th group enhances its optical properties [56–58]. There are several reported works on the synthesis of ZnO nanoparticles doped with these group 13 elements [58–61]. Aluminium doped ZnO nanoparticles, in general, has found many applications as gas sensors [62], catalysts [63], electrode [64] etc. The doping of ZnO with Al is n-type doping as it creates deficiency of valence electrons. This, in turn, increases the number of charge carriers which is beneficial for application in optoelectronic devices like solar cells and organic light-emitting diodes.

Referring to point a), there are many works available in the literature where ZnO nanoparticles were doped by transition metal ions. Moreover, different synthesis techniques have been utilised to synthesise ZnO nanoparticles doped with these metal ions, such as combustion method [65], sol-gel [66], co-precipitation [67] etc. Among all the metals, Fe has received much attention as it is considered a promising p-type dopant [68]. Likewise, Igbal *et al.* prepared Fe-doped ZnO nanocrystals from zinc nitrate and iron chloride by wet chemical synthesis in an autoclave at 120 °C for 15 hours. [69]. In this work, different concentration of Fe dopant was employed and its effect investigated. It was found that nanoparticles, nanorods and nanowires were observed at different doping concentrations. In addition to the change in morphology, the gap between the conduction and valence band also reduced with more dopant concentration. Ciciliati *et al.* demonstrated an improvised sol-gel synthesis technique. In their work, the solvent used was a solution of PVA (10% w/v) where the reaction mixtures were heated at 300 °C for 2 hours. It was also observed that with increasing Fe dopant percentage, the bandgap of ZnO increased [66]. In another work, Bi-doped ZnO nanoparticle was synthesised by the sol-gel method [70]. An investigation was carried out to study the impact of Bi dopant on the crystallite size, microstructure, crystal defect and morphology of ZnO nanoparticle. With increasing Bi content, the crystallite size increased due to the agglomeration of small crystallites. It can be concluded that the addition of the dopant increased the crystallinity with reduced crystal defect. In another work, Ovhal *et al.* utilised the principle of sonochemistry where a reaction mixture is carried out under powerful ultrasound radiation. The Fe-doped ZnO was synthesised by ultrasonic precipitation method was conducted at room temperature at a frequency of 20

kHz. The dopant influenced the crystal structure, lattice strain, particle size and optical properties [71]. Additionally, in work by Singhal *et al.* (109), the doping of ZnO with Fe was synthesised in hexadecylamine (HDA) at 200 °C for 2 hours. A stable colloidal dispersion in toluene and chlorine was made possible due to the presence of the amine group. HDA served both as solvent and ligand, where the amino group bound to the surface of the Fe-doped ZnO [72]. Wang *et al.* [54] investigated the superparamagnetic behaviour of as synthesised Fe-ZnO at room temperature. The nanoparticles doped with Fe was synthesised by polyol technique refluxed at 278 °C for 38 minutes [73]. In other investigation, non-hydrolytic microwave-assisted preparation of $\text{Fe}_x\text{Zn}_{1-x}\text{O}$ ($x = 0.02\text{--}0.45$) in benzyl alcohol was published [74]. The benzyl alcohol route is a widespread technique based on the decomposition of metal acetates in benzyl alcohol which acts as a reagent, solvent, and capping agent. It must be stressed out that homogeneity and stability of semiconductor nanoparticle dispersions is a decisive feature for further applications of these materials. Moreover, Skoda *et al.* synthesised a ZnO nanoparticles by polyol technique in a microwave reactor. A colloidal dispersion was achieved by dispersing the oleic acid-capped ZnO in toluene [75]. Of late, in another work by Skoda *et al.*, ZnO was doped with another transition metal cobalt. Further, a nanocomposite solution was prepared by mixing Co-doped ZnO and MEH-PPV. The nanocomposite solution served as an emissive layer in the fabrication of polymer light-emitting diode (PLED) [76].

Referring to point b) In Al-doped ZnO (AZO), one can find applications in the preparation of transparent conductive electrode that can find an alternative to indium tin oxide (ITO). The electrical conductivity of the AZO material depends on the doping concentration and grain size as well [77, 78]. The advantage of using AZO thin film over indium-doped tin oxide is that AZO is economical, abundant and non-toxic. As the prices of ITO material is increasing and as well as the demand, there is a need of an alternative to the current ITO material. Due to rapid realisation and development of optoelectronic devices, there is ever increasing demand for ITO, especially as a transparent electrode in flat panel displays, smart windows, polymer-based electronic devices, solar cells etc.

The wet-chemical synthesis of AZO nanoparticles is an efficient synthetic technique. The first AZO nanoparticles were synthesised about four decades ago. Since then, numerous researchers have worked on its synthesis with several potential applications. Avadhut *et al.* investigated the structure of Al-doped ZnO by nuclear magnetic resonance spectroscopy (NMR). A microwave reactor was used to synthesise the doped ZnO semiconductor nanocrystals. In the polyol synthesis of AZO nanoparticles at 248 °C, a nanoparticle suspension was obtained. The researchers cast the AZO on a glass substrate by spin coating and their optical and electrical properties studied. The solid-state NMR of the core-shell structure provided an insight into the particle structure and its functionalities [79]. In another work, Kelchtermans *et al.* synthesised AZO with different reaction parameters. In the investigation, one reaction was carried out by

solvothermal technique and the other in reflux. Moreover, benzylalcohol was the solvent used in solvothermal synthesis, and the reflux under ambient condition was carried in benzylamine. The two synthesis route resulted in different morphologies, nanorods for the solvothermal synthesis and nanoparticles for the reflux reaction condition [80]. One-pot synthesis of porous AZO transparent conductive oxides (TCOs) was reported by Bo *et al.* [81]. The three-dimensional AZO nanoparticles were prepared by flame spray pyrolysis by regulating the porosity and hierarchy from nanoparticle aerosols. The porosity was controlled by optimising the height above the flame burner from 6 to 20 cm. The study revealed that the porous AZO thin films could potentially be used as light-sensitive gas sensors with room temperature response of 1.92 to 1 ppm ethanol concentrations. Another interesting work was carried out by Zhang, silver nanowire (AgNW), polyvinyl butyral (PVB) and aluminium-doped ZnO (AZO) composite were prepared [82]. The composite was cast on top of each other layer-by-layer by doctor-blade coating on a glass substrate at low temperature. The multi-layered composite film displayed high transmittance in the visible range with the highest percentage (94%) at 550 nm. The sheet resistance of the film measured was $21 \Omega \text{ sq}^{-1}$. The PVB layer sandwiched between the Ag nanowire (AgNW) and AZO is for good adhesion of AgNW onto the glass substrate. The AgNW ink was poorly bound to the glass substrate. The multi-composite layer was used as a transparent conducting electrode for polymer solar cells (PSCs) that exhibited high transparency, low sheet resistance and good thermal stability.

1.3 Microwave synthesis of nanoparticles

The use of microwave irradiation in chemical synthesis was first reported in 1986 by Richard Gedye *et al.* [83]. They used a microwave reactor to synthesise organic compounds. Since then, this technology has rapidly increased to most areas of synthetic chemistry, nanoparticle synthesis, in particular. It paved a new way to efficiently synthesise metal oxide, metal sulphides, metal selenides nanoparticles etc. [84–88]. One of the main advantages of using microwave irradiation over conventional heating is the rapidness with which a reaction occurs. Apart from this, the yield of the product is higher and side reactions are avoided.

The principle of this technology is based on the absorption of the radiation in a suitable frequency range for efficient conversion of the electromagnetic energy into heat. Generally, the frequency range of the microwave irradiation is 0.3 to 300 GHz. This electromagnetic radiation has the main applications in radio technology. Moreover, commercial and domestic microwave reactors operate at the frequency of 2.45 GHz, thus, avoiding interference of the frequency bands.

Microwave synthesis of organic compounds is quite popular, but the wet synthesis of nanoparticles is not well-established yet. As stated earlier, the heating in the microwave synthesis is different from conventional heating, like oil bath, as the heating is uniform and efficient. Apart from this, shorter reaction time and

good yield are the other two advantages of synthesising nanoparticles with microwave reactor [21]. Conventional heating is not as effective as the microwave reactor as it heats the walls of the reactor or apparatus and then the reactants by conduction or convection, Fig. 1.3. As a result, the reactants take a longer time to heat up, leading to non-uniform heating of the reactants. The illustration below compares the conventional heating with microwave heating with respect to time.

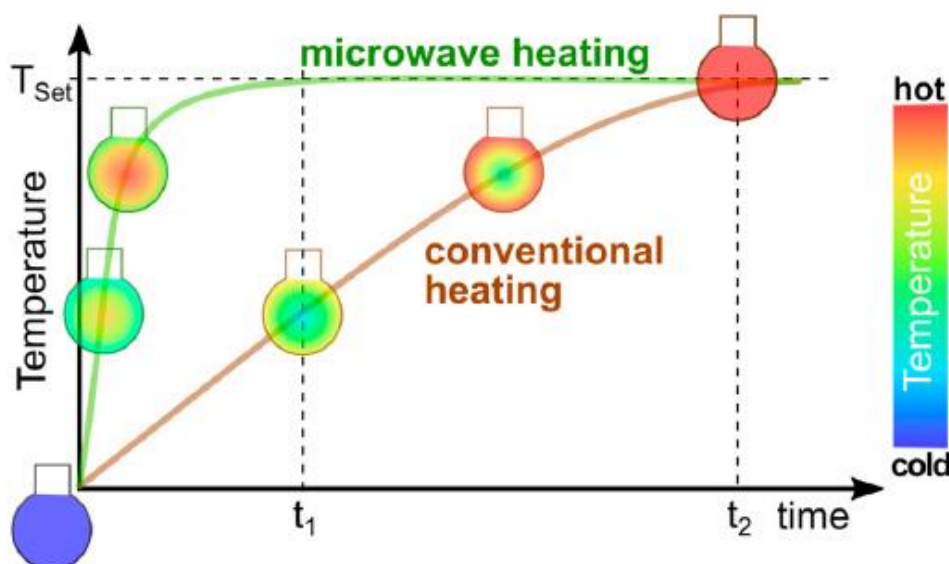


Fig. 1.3 Difference between conventional and MW-heated reaction as a function of time ($t_1 < t_2$) [89].

The microwave heating of a matter is based on the absorbing ability of the solvent or reagents. This can be termed as loss tangent or dielectric loss; this is the measure of conversion efficiency of the electromagnetic radiation into heat. The dielectric loss or loss tangent is represented as [90]:

$$\tan \delta = \frac{\epsilon''}{\epsilon'} \quad 1.1$$

ϵ'' = dielectric loss is the measure of the conversion of electromagnetic radiation into heat.

ϵ' = dielectric constant is the ability of a material to be polarised by the electric field.

A material or solvent with high $\tan \delta$ value is necessary for the material as it has a high capacity to absorb microwaves because it increases the microwave penetration depth. The $\tan \delta$ value is a function of microwave frequency and temperature. The microwave chemistry is based on the heating of a matter, and it has two heating mechanisms: dipolar polarisation and ionic conduction, Fig. 1.4. Microwave irradiation of polar molecules leads to the alignment of ions or dipoles

with the electric field. During this process of alignment, heat is generated due to the rotation or friction of molecules. This is the dipolar heating mechanism by microwave. For ionic conduction, the oscillations of the ions in a solvent due to microwave irradiation creates heat, resulting in the rise of temperature in the solution [90].

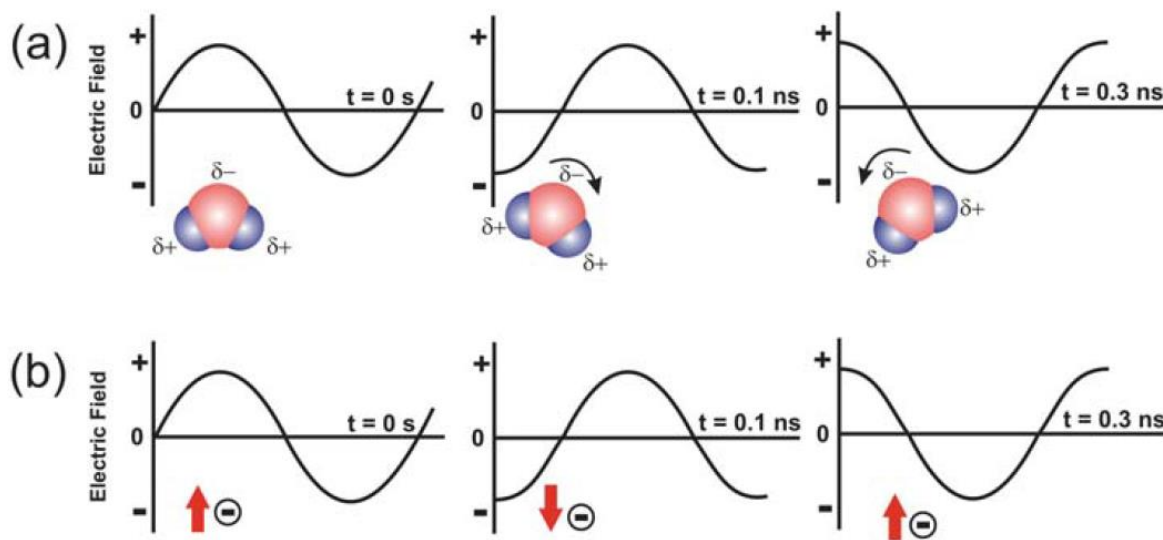


Fig. 1.4 (a) Dipolar heating mechanism (b) ionic heating mechanism [91].

The above-described mechanism is an appropriate model for processes in homogeneous phase. The peculiarity of (nano)particle synthesis is the inhomogeneity of the multiphase-system concerning the mechanisms of the radiation absorption and relative permittivity of various phases. It can be hypothesised, that the microwave energy from a constant intensity irradiation source is delivered monotonously to an initially homogeneous reaction system until a critical point when the phase composition of the system changes and new differently (potentially better) absorbing phase (or interphase) appears. Then, the channel of energy dissipation may be changed, and a new dynamics prevails in the system. Such a switching event results in a stepwise process. Examples of suddenly occurring events are already known from hot-spot and run-away phenomena in microwave heating. Unlike these negative phenomena, a beneficial transition step may result in high-quality of the product due to simultaneous triggering of a synthetic step. It was observed in the previous work of our research group [92, 93].

1.4 Band gap engineering

The band gap widening and the emergence of the fine structure of the conductive and valence bands in nanoparticles is a size scale phenomenon not observed in bulk crystals. It is a result of quantum confinement of electronic states in the sufficiently small (nano) objects, as depicted in Fig. 1.5 [94]. Hence, it is

possible to control the band gap width just by the particle size. Nevertheless, some additional degrees of freedom in control of the density of states, charge carrier concentration and other properties are desirable. Doping of the material represents such a possibility. Doping is the intentional addition of impurities to materials for manipulation, control and acquiring improved properties. It is essential for semiconductors that would otherwise be electrically insulating or less conducting. The important role played by dopants in the semiconductor nanoparticle synthesis has generated research on several applications, especially in the fabrication of electronic and optoelectronic devices [81, 95–97]. The tuning of band gap of semiconducting material is of good research interest as it changes the properties of the semiconductor. In addition, doping of the semiconductor is one way of achieving that. When a dopant is added to the semiconducting nanomaterial, the energy band gap of the nanoparticle is either widened or reduced; depending upon the type of dopant used.

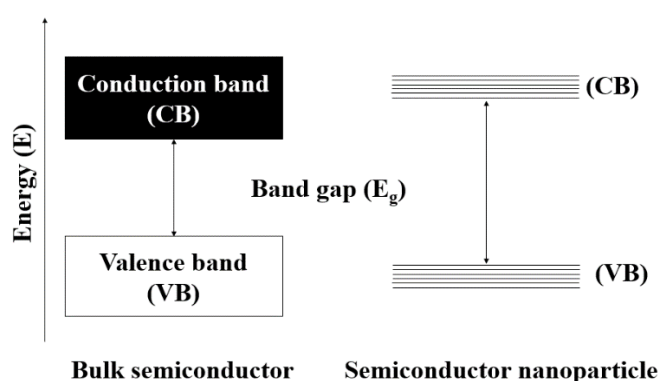


Fig. 1.5 Illustration of the increase in band gap in nanometre range.

A dopant can only be successfully incorporated into the host crystallite lattice when, during the reaction, the growth of the host crystal and the deposition of the dopant is balanced [98]. The addition of impurity enhances not only the band gap, but also the luminescent properties. Also, a material is said to be successfully doped only when the dopant replaces the host atoms rather than just getting adsorbed on the nanocrystal surface. A dopant with more than one or more valence electrons than the host atoms is n-type doping, and the one with one less valence electron is p-type doping. Subsequently, n-type doping has more number of electrons as charge carriers, and in p-type doping, holes form the majority of the carriers [99]. Going ahead, the progress in doped nanocrystals would require optimizing the synthetic control of the dopants and study of its phenomena.

1.5 Surface modification

Wet-chemical synthesis is one of the most popular syntheses of nanoparticles due to its simplicity and reproducibility. Furthermore, capping agents are used to control the growth and particle size in this synthesis method [100]. These long-

chain organic ligands are the basic component for attaining control over size and shape of nanoparticles. In addition, understanding the surface chemistry of the nanoparticle-ligand interphase is necessary in order to procure tailor-made nanoparticle characteristics. Other than preventing agglomeration of the nanoparticles during synthesis, the surface-coated nanoparticles can also facilitate in acquiring stable dispersion in solvents [101]. These stabilising agents are amphiphilic in nature, having both hydrophilic group (head) and hydrophobic group (tail). The head and tail parts of the molecule are characterised by functional groups. One of the functional groups anchors onto the surface of a synthesised metal or metal oxide nanoparticles. This, in turn, reduces surface energy checking particle or grain growth and formation of clusters. Some of the common functional groups that constitute a part of capping agents are amino (—NH_2), thiol group (—SH), carboxyl group (—COOH), and sulphate (—OSO_3^-) as in sodium dodecyl sulphate (SDS). Many organic molecules have been used to functionalise the reactive surface of nanoparticle [102–105]. The capping agent can control the growth and shape of a nanoparticle. Oleic acid, oleylamine, (trioctylphosphine oxide) TOPO, (triethanolamine) TEA etc. are some of the examples of the capping agents. In typical liquid-phase synthesis, colloidal nanocrystals are prepared and surface-functionalised during the reaction with the help of a ligand that binds to the particle surface. Nanocrystal has a large surface-to-volume ratio which plays a major role in determining the properties of a nanocrystal. During nanoparticle growth, a capping agent (a long chain organic molecule) forms a layer around the nanoparticle and controls growth of the nanoparticle. It forms a shield around the nanoparticles and reduces surface energy. This leads to the prevention of agglomeration of the usually high surface-energy nanoparticles, and dispersion of single nanoparticles can be obtained in the ideal case. As mentioned, the capping of nanoparticles enables it to disperse in liquid media for further processing due to their interaction with the (liquid) environment. This colloidal dispersion can be used as building blocks for bridging scales from nanoparticles to materials for various purposes.

Most importantly, capping agents enable the nanoparticles to disperse in non-polar solvents. In the context of applications of the surface-modified nanocrystals, especially with the solution-processing of the stable dispersion, it has its pros and cons. Looking at the brighter side of it, as discussed in the current topic, the stable dispersion enables it to be applicable in optoelectronic device fabrication [76]. One of the disadvantages of coating the surface, particularly in the device performance, would be the long-chain organic molecules. These molecules affect the device operation, if they form an insulating (barrier yet monomolecular) layer, thus intervening transfer of charge carriers.

1.6 Nanocomposite and device preparation

Research on electronic properties of nanocomposite materials has been growing due to its potential applications in optoelectronic devices like organic

light-emitting diodes (OLEDs) [106, 107] and organic photovoltaic cells (OPV) [108], etc. For example, Zhang et al. utilised a one-step microplasma synthesis of Au nanoparticles in PEDOT:PSS/aqueous, (poly(3,4-ethylenedioxythiophene) polystyrene sulfonate) solution at room temperature. This nanocomposite has potential application as fuel-cell electro-catalyst. Similarly, MEH-PPV, poly[2-methoxy-5-(2'-ethylhexyloxy)-1,4-phenylene vinylene], was mixed with TiO₂ and their photoelectrochemical and optical properties were analysed by Habelhames et al. The bulk heterojunction displayed an increase in its performance after the incorporation of TiO₂ nanoparticles [28]. The most studied polymer nanocomposite component is the p-type MEH-PPV which imparts hole charge carrier mobility along its polymer chains [109]. In contrast to that, ZnO is an n-type of semiconductor with electrons involved as charge carriers. Therefore, the composites of ZnO nanoparticles and MEH-PPV are advantageous due to the balance they provide in electrons and holes density, respectively [110].

Recent developments have demonstrated that hybrid inorganic-organic systems (n-type ZnO nanoparticles and conductive polymer) are very interesting for UV LED and OLED applications [111, 112]. Important to this work is the fact that a single layer of nanocomposite active layer is more efficient than two separate layers of MEH-PPV and ZnO nanoparticles [113]. In that work conducted by Petrella et al., it was found that the single-layer heterojunction displayed about 93% photocurrent increase compared to the double layer heterojunctions. Consequently, it led to faster charge transfer rates due to the formation of a larger number of interfaces. On the other hand, this hybrid system has another advantage as the OLED can have emission in the entire visible spectrum [114]. Adding to the pros of the organic-inorganic heterostructures, it is also possible to tune the emission of the fabricated OLED. The blending of MEH-PPV with ZnO nanoparticles further improves the efficiency of electron injection into the p-type MEH-PPV polymer [106]. Correspondingly, tailoring of the semiconductor nanoparticles was achieved by doping it with transition metals which helps in tuning the optical properties with improved light efficiency and emission of optoelectronic devices [97].

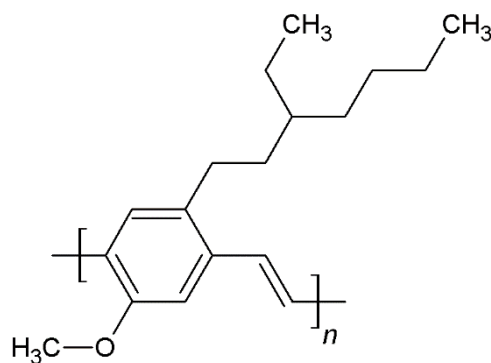


Fig. 1.6 Molecular structure of MEH-PPV.

Fillers are particles used to fill cavities in a material in order to improve the processing behaviour and to design create improved materials with unprecedented physical or chemical properties. The use of inorganic nanomaterials as filler for a polymer, e.g. MEH-PPV (Fig. 1.6), in nanocomposites preparation, is of immense research interest and has attracted many researchers over the last few decades. Polymer nanocomposites are a combination of macromolecular compound, i.e. a polymer, and nanosized particles that results in the polymer having enhanced physical properties with potential applications in diverse fields, mainly in nanoelectronics [115, 116]. Such combinations of organic and inorganic composites have technological applications due to their good processibility and process repeatability.

Dispersions of inorganic semiconductor nanoparticles can be blended with the solution of conducting polymers to obtain a liquid precursor of nanocomposites. Such mixture can be used for the preparation of thin nanocomposite films with interesting and enhanced properties with potential applications, mainly in optoelectronic devices. The nanocomposite is a bridge between nanoparticles and the actualisation of its applications. Notably, it has raised a great deal of scientific and technological interests. One such example is the fabrication of polymer light-emitting diode (PLED) via solution processing [76]. The assembling of optoelectronic devices using organic polymers is economical, relatively easy processing, lightweight etc. With the polymer-filler hybrid functioning as an active material, it provides numerous applications, including flexible displays. It has gained attention due to its potential technological advantages. It could provide an alternative to its inorganic counterparts like the conventional semiconductor (silicon, gallium, indium etc.). The processing of the devices using these semiconductor materials require sophisticated techniques with high production costs which are in contrast to the utilisation of organic-inorganic fillers. Having said that there are some physicochemical challenges attached to the use of the hybrid nanocomposites. The low glass transition temperature of the polymer and the instability of its long molecular chains still renders it not suitable for its long-term usability.

From the practical point of view, the solution process fabrication of PLED device is economical and is widely researched upon because of its simplicity in comparison to the physical deposition technique where it requires high vacuum condition which is not available in our laboratories. A simple technology of the fabrication of devices is a must under such conditions. Prepatterned ITO serves as an anode (work function 4.7 eV) and works as a hole-injecting layer. The anode is covered by PEDOT:PSS, the hole transporting layer. On top of the hole transporting layer, the nanocomposite is deposited. Both layers are easily spin-cast from liquid dispersions. The simplest sputtering technique for the deposition of a metallic cathode is available for non-oxidising metals. The best choice among them, Mg, has low work function (3.66 eV) and injects electrons. The emissive layer or the active layer is sandwiched between the two electrodes and is the

meeting point of electrons and holes. This leads to the emission of the active layer. It is the conjugate polymer MEH-PPV that is responsible for the emission of the diode. Since MEH-PPV is a p-type conjugate polymer and ZnO an n-type semiconductor, this combination improves the ratio between electrons and holes. Doping of ZnO nanoparticles may help balance the charge carriers. It is expected that the device performance will increase. Thus, the hybrid heterojunction devices fabricated by the solution-process casting of the layers should provide better performance than their solely polymer-based counterparts [117].

2. AIMS OF THE DOCTORAL THESIS

The thesis focuses on the microwave-assisted polyol synthesis of pure and doped ZnO nanoparticles suitable for application in the fabrication of PLED devices. The aim of the thesis is divided into five specifically addressed points:

1. The first goal is to investigate the effect of minor stoichiometric water content associated with the use of hydrate precursors and the effect of a suitable capping agent in the microwave-assisted polyol synthesis of ZnO nanoparticles. This includes two studies:
 - a) Study of the role of the minor water content in the ZnO nanoparticle formation.
 - b) Study of the effect of oleic acid employed as a capping agent during nanoparticle synthesis.
2. In the second goal, the effect of the different molar concentration of zinc precursor on the final product properties in the microwave-assisted polyol synthesis of ZnO nanoparticles is to be studied.
3. Thirdly, the goal is to develop a microwave-assisted polyol synthesis of Fe doped ZnO nanoparticle material and characterise the products with specific attention paid to the oxidation state of the dopant. Iron is a transition metal element, and its doping character to ZnO may depend on the preparation method.
4. The fourth goal is in developing a microwave-assisted polyol synthesis of Al-doped ZnO nanoparticle and characterisation of the product. Aluminium belongs to group 13 and is an n-type dopant to ZnO.
5. Finally, the goal is to demonstrate and analyse the performance of PLED diodes using prepared nanoparticles as fillers to the emissive MEH-PPV layer. Neat MEH-PPV polymer-based PLED is used as a reference diode.

3. EXPERIMENTAL METHODS AND INSTRUMENTATIONS

3.1 Analytical techniques

3.1.1 X-ray diffraction (XRD)

X-ray diffraction (XRD) crystallography technique utilises high-energy X-rays for analysing the atomic and molecular structure of crystalline material. When X-ray is incident on a crystal lattice of a sample, the rays that constructively get scattered is recorded by the instrument to form peaks in intensity. It is the regular arrangement of crystal lattice on the order of angstrom which is equivalent to the wavelength of the X-rays make it possible for the rays to interact with the lattices in the crystal. And, the condition in which the constructive rays from the crystal interact with the X-rays is given by Bragg's law:

$$n\lambda = 2d \sin \theta \quad 3.1$$

where, n is an integer, λ is the wavelength of the incident X-ray, d is the spacing between diffracting planes or interplanar spacing, θ is the angle of the incident ray.

To check the crystallinity of the prepared materials, XRD diffraction patterns were recorded on Rigaku Miniflex 600 with CoK_α ($\lambda = 1.7903 \text{ \AA}$) X-ray tube (40 kV, 15 mA) using a PDF (powder diffraction files) database for phase identification. Moreover, the average crystalline particle size was calculated using Scherrer's formula,

$$d = \frac{K\lambda}{\beta \cos \theta} \quad 3.2$$

where d is the crystallite size, K is a grain shape-dependent constant (0.9), λ is the wavelength, θ is a Bragg reflection angle, and β is the full-width half-maximum corrected by the subtraction of the instrumental broadening.

3.1.2 Transmission electron microscope (TEM)

The transmission electron microscope is a powerful electron microscope to study the average particle size, morphology, topology and composition of crystalline material. Unlike the optical microscope, an electromagnetic lens is used in this microscopic analysis for accelerating the high energy electrons emanating from the electron gun into the sample. This instrument utilises the energetic coherent electron beams that interact with a sample in a vacuum chamber. The specimen is typically a layer on an ultrathin grid of about 100 nm

thickness. When the beam strikes the specimen, the beam gets transmitted through the specimen, and the image gets focused by the objective lens on a fluorescent screen or charge-coupled device camera (CCD).

The transmission electron microscopy images of the samples were taken on a TEM JEOL JEM 2100 operated at 300 kV (LaB6 cathode, point resolution 2.3 Å equipped with OLYMPUS SYS TENGRA camera (2048 x 2048 pixels). Furthermore, the particle size distributions were evaluated with Olympus Soft Imaging Solutions software. Also, for the TEM sample preparation, carbon-coated Cu grids (300 mesh) were used where colloidal solutions on the Cu grids were dropped (few μL) and kept for drying for 1 hour at 80 °C.

3.1.3 Scanning electron microscope (SEM)

The scanning electron microscope (SEM), like the transmission electron microscope, uses energised electrons from an electron gun due to the application of high voltage. This imaging technique does not pass through the sample; instead, the electron beam hit the sample and penetrates the sample to a depth of a few micrometres. As the electron beam strikes the sample and interacts with it, secondary electrons, backscattered electrons and other rays are produced. All these signals get directed toward the detector and converted to images which are displayed on a computer screen.

EDS stands for Energy Dispersive X-ray spectroscopy. It is an elemental analysis technique for determining the chemical composition of a sample. The EDS analysis in SEM operates in two steps. In the first step, the accelerated electron strikes the sample, and the energy from it is passed on to the atoms sample. These atoms acquire the energy, and an electron is knocked out from one of the shells of the atom. The ejection of electron results in the creation of a hole. In the following stage, an electron from a higher energy state gets attracted to the positively charged hole and fills the gap of the lower-energy shell. This leads to the emission of an X-ray photon of characteristic wavelength from the atom. This emission of the X-ray radiation from the specimen allows the EDX instrument to determine the elemental composition of the sample generated in the form of spectral peaks on a computer screen.

The scanning electron microscopy images of the samples were done on a Nova NanoSEM (FEI) microscope with a Schottky field emission electron source (0.02–30 keV) and a TLD detector. The presence of Fe dopant was determined by a scanning electron microscope (SEM) Vega II/LMU (Tescan, Czech Republic) equipped with a backscattered electron (BSE) detector, secondary electron (SE) detector and energy dispersive X-ray (EDX) analyzer (Oxford Instruments INCA). Correspondingly, the hydrodynamic diameters and size distributions were recorded on a Malvern Zetasizer ZS.

3.1.4 Fourier-transform infrared spectroscopy (FT-IR)

The Fourier-transform infrared spectroscopy (FT-IR) is a spectroscopic technique that is employed to study and analyse both organic and inorganic compounds. It detects a range of functional groups due to the absorption of the infrared spectrum by a solid, liquid or gas specimen. The FT-IR utilises a broadband light source containing full-spectrum of wavelength. This spectral beam is then shone on to series of mirrors (Michelson interferometer). The mirrors are configured in a way that each wavelength of beam is periodically blocked and transmitted. Then, the modulated beam is passed through the sample where the beam gets absorbed as a function of the molecular structure of the sample. The computer process (Fourier transform) the data and converts the raw data into a spectrum with a distinctive molecular fingerprint.

The infrared absorption spectra of the powdered samples were studied with FTIR spectra in the region 4000-400 cm^{-1} , Thermo NICOLET 6700 using an ATR technique with a diamond crystal.

3.1.5 Ultraviolet-visible spectroscopy (UV-Vis)

The absorption spectroscopy measures the electron transition from a ground state to the excited state. This technique operates in the ultraviolet and visible region. When a sample is irradiated with light, the sample absorbs photons. This leads to the excitation of the electrons from the ground states to higher energy states in molecules. Similarly, the transition between the conduction band and valence band is an equivalent in the solid phase. The underlying principle of the UV-Vis spectra follows the Beer-Lambert Law. According to Beer and Lambert, when a monochromatic beam of light is incident on a sample solution, the amount of light passing through it is proportional to the concentration of the solution and the incident radiation. The relation between the incident light, the optical length path and the concentration of the sample is given as:

$$A = \epsilon cl \quad 3.3$$

where, A is the absorbance, ϵ is the molar absorption coefficient ($\text{M}^{-1} \text{cm}^{-1}$), c is the molar concentration (M), l is the optical path length (cm).

Thus for a fixed optical path length, the concentration of the absorber can be quantified in a solution. In determining the absorption spectra of the nanoparticles, the spectra were recorded on a Perkin-Elmer Lambda 1050 spectrometer.

Moreover, measurements of diffuse reflectance UV-Vis (DR-UV-Vis) were used to study the light absorptivity and diffuse reflectivity of the powdered samples. DRUV-Vis spectra were recorded on a Perkin-Elmer Lambda 1050 spectrometer as well. Later, from the Tauc plot, the optical band gaps were calculated.

The band gap energy for dried nanopowder samples were determined from diffuse reflectance spectra. The Kubelka-Munk function was employed for the calculation of the band gaps.

$$F(R) = \frac{(1 - R)^2}{2R} \quad 3.4$$

In the above equation, $F(R)$ represents Kubelka-Munk function, R is the absolute reflectance of the powdered nanoparticles [118]. The extrapolation of Tauc plot, $[F(R).h\nu]^2$, on the y-axis and the photon energy $h\nu$, on the x-axis, gives us the band gap of the semiconductor nanoparticles. $F(R)$ represents the Kubelka-Munk remission function, h is the Planck's constant and ν is the energy of the photon. Here, the value of n is 1 as ZnO has a direct band gap.

3.1.6 Fluorescence spectroscopy

Fluorescence spectroscopy technique measures the emission of a sample when it is irradiated with monochromatic light (mostly ultraviolet light) and emitting light at longer wavelengths within its emission band. Absorbance spectroscopy is the complementary technique of fluorescence technique. In fluorescence, a monochromatic light excites the specimen when it absorbs the light; the transition is from the valence band to the conduction band. It is followed by the emission of light due to de-excitation. When electrons are powered up from the valence band to the conduction band due to high energy photon, the electrons leave behind holes at the valence band. And, when the excited electrons from the conduction band de-excite to the valence band, light is emitted in the longer wavelengths. Moreover, the energy of a photon is given by this relation:

$$E = h\nu \quad 3.5$$

where, E is the energy of the incident photon, h is Planck's constant ($6.626 \times 10^{-34} \text{ m}^2 \text{ kg/s}$), and ν is the frequency of the incident photon.

The energy difference required to excite an electron from the valence band to the conduction band is the energy bandgap of the material. The emission spectra of the samples were recorded at room temperature in the photoluminescence (PL) spectrometer FLS920, Edinburgh Instruments (excitation laser 332.2 nm, Xe lamp excitation 515 nm)

3.1.7 Dynamic light scattering (DLS)

Dynamic light scattering (DLS) is an analytical method for measuring the particle size dispersed in a solvent. In this instrumental technique, monochromatic laser light is directed towards the particles dispersed in a solvent. The interaction

of the laser with the particles scatters the light in several directions. Depending on the size of the particles, the intensity of the scattered light varies. This change in the intensity of the scattered light due to Brownian motion is estimated by the Stokes-Einstein equation:

$$d(H) = \frac{kT}{3\pi\eta D} \quad 3.6$$

where, $d(H)$ is the hydrodynamic diameter of the particles in the liquid media, k is the Boltzmann's constant, T is the absolute temperature, η is the dynamic viscosity and D is the translational diffusion coefficient (referred to the random movement of the particles in the solvent). The hydrodynamic diameter value is dependent not only on the particle size and shape but also on factors like its surface properties (including eventual coating) and solvation shell. Consequently, the hydrodynamic diameter measured from the DLS technique is higher than the average particle size observed from transmission electron microscopy (TEM).

3.1.8 Thermal analysis

Further, to study the thermal behaviour of the samples, simultaneous thermogravimetric analysis and differential scanning analyses TGA/DSC were performed on a Setaram LabSys Evo instrument in Al_2O_3 crucibles in the flow of air 60 ml min^{-1} and a heating ramp $10 \text{ }^\circ\text{C min}^{-1}$ up to $1000 \text{ }^\circ\text{C}$.

3.1.9 Profilometry

A profilometer Dektak XT-E (Bruker) with a 1 nm resolution was used to measure thicknesses of the thin films.

3.1.10 Diode characterisation

In order to study the electroluminescence spectra, the measurements were recorded on a UV/Vis spectrometer Avantes Avaspec 2048 using an integration sphere with 50 mm diameter. Finally, the I-V characteristics were measured by a multimeter HP 34401A and a power supply system HP 6038A.

Conversions of the recorded spectra to colour coordinates and plotting of the chromaticity diagrams were performed using the free version of a commercial software ColorCalculator released by OSRAM SYLVANIA. More details can be found in the following reference web page (<https://www.osram.us/cb/tools-and-resources/applications/led-colorcalculator/index.jsp>).

3.2 Materials

De-ionised water, zinc acetate dihydrate ($\text{Zn}(\text{OAc})_2 \cdot 2\text{H}_2\text{O}$, p.a., $M_w = 219.51 \text{ g/mol}$), anhydrous Zinc acetate ($\text{Zn}(\text{OAc})_2$, $M_w = 183.48 \text{ g/mol}$), iron

acetylacetonate (Fe(III)(Acac)_3 , 99 %, $M_w = 324.31 \text{ g/mol}$), aluminium acetylacetonate (Al(Acac)_3 , 99 %, $M_w = 353.17 \text{ g/mol}$), indium acetylacetonate (In(Acac)_3 , 99 %, $M_w = 412.14 \text{ g/mol}$) and MEH-PPV Poly[2-methoxy-5-(2-ethylhexyloxy)-1,4-phenylenevinylene] ($M_w = 40000\text{--}70000 \text{ g/mol}$) were purchased from Sigma-Aldrich. Diethylene glycol (p.a., DEG), oleic acid (OA, p.a. $M_w = 282.46 \text{ g/mol}$), toluene (p.a.), methanol (p.a.) were purchased from PENTA Czech Republic, and PEDOT:PSS (poly(3,4-ethylenedioxythiophene) polystyrene sulfonate) supplied from Heraeus (CleviosTM P AI 4083).

3.3 Synthesis of undoped ZnO, the role of water and capping agent

3.3.1 General synthesis protocol

In a typical synthesis, $\text{Zn(OAc)}_2 \cdot 2\text{H}_2\text{O}$ or Zn(OAc)_2 was used as the ZnO precursor. The calculated amount of the precursor (3.6 mmol of $\text{Zn(OAc)}_2 \cdot 2\text{H}_2\text{O}$ and Zn(OAc)_2 for all the reactions except for ZnO series), was mixed with 50 ml diethylene glycol (DEG) and eventually with a weighed amount of oleic acid as a capping agent in a Teflon-lined container. Further, the reaction mixture was then put in a microwave reactor, turned on, and the power applied was typically 100 % for 15 min. The temperature raise was sigmoidal up to 250 °C. Later, when the reaction was complete, the white suspension (brownish suspension for Fe-ZnO) for pure and Al-doped ZnO was centrifuged and washed with methanol and dried at 80 °C. In addition, some part of the precipitates from the Teflon container was dispersed in 50 cm³ of toluene to form a colloidal dispersion.

3.3.2 Role of water molecules

The aqueous wet-chemical synthesis of metal oxide nanoparticles includes the thermal decomposition of the metal oxide precursor in the presence of water. The polyol synthesis is ideal for the synthesis of nanoparticles, mainly metal oxide nanoparticles. With this synthetic technique, there is control in size and morphology of the prepared material at the time of chemical reaction. The manipulation in the nanoparticles during the synthesis is achieved by optimising the temperature, type of precursor and its concentration and reaction duration [119]. Moreover, the water molecules play a role in the synthesis of particles of nanometre range. In general, the presence of water impacts the particle size and morphology [39, 120]. The ability of the water molecules to solubilise the metal precursor is also beneficial. However, in non-hydrolytic synthesis, the OH group could be donated by the solvent or from the hydrated part of the metal salts indicating that a reaction can be conducted without the addition of water molecules [121]. In the aqueous synthesis of metal oxide nanoparticles, the oxygen molecules for the formation of the oxidic compound is provided by the water molecules [122]. Mainly, for the formation of metal oxide nanoparticles,

the reduced metal precursor bonds with oxygen atom supplied by the water. However, the presence of water inhibits reduction and favours the hydrolysis of a metal precursor. The general mechanism for the formation of metal oxide nanoparticles is hydrolysis and condensation.

For a non-hydrolytic approach, the water molecule is either supplied *in situ* from the hydrated metal precursor or intrinsically from the organic medium. There are various mechanisms in the literature on the non-hydrolytic approach of nanoparticles, and a concrete mechanistic approach is yet to be distinguished. This approach is also advantageous in attaining monodisperse colloidal nanoparticles with controlled size and morphology. The general methodology of the formation of metal oxide nanoparticles is a thermal reduction and hydrolysis of the metal oxide precursor.

The section focuses on the role of water molecules in the synthesis of ZnO nanoparticles using a microwave reactor. $\text{Zn}(\text{OAc})_2 \cdot 2\text{H}_2\text{O}$ and $\text{Zn}(\text{OAc})_2$ were used as ZnO nanoparticle precursor. Diethylene glycol (DEG) was used as a solvent. Three sets of reactions were performed to functionalise the metal oxide nanoparticle surface. The scheme of the reactions is shown in the table below (Table 3.1), to study the role of water. There are two sets of samples, ZOA and ZNP. The acronym NW means no water (anhydrous acetate), CW means crystal water (dihydrate acetate) and 2 or 4 means addition of water to the reaction mixture in the stoichiometry equivalent amount 2 or 4, respectively. Another three sets of reactions were performed to study the role of oleic acid in ZnO nanoparticle synthesis, which is described in the next section.

Table 3.1 Scheme of reactions to study the role of water and oleic acid.

Sl no.	Sample name	ZnO precursor	Water molecules	Oleic acid
1	ZOA-CW	$\text{Zn}(\text{OAc})_2 \cdot 2\text{H}_2\text{O}$	Yes	Yes
2	ZNP-CW	$\text{Zn}(\text{OAc})_2 \cdot 2\text{H}_2\text{O}$	Yes	No
3	ZNP-NW	$\text{Zn}(\text{OAc})_2$	No	No
4	ZOA-NW	$\text{Zn}(\text{OAc})_2$	No	Yes
5	ZNP-4W	$\text{Zn}(\text{OAc})_2 + 4\text{H}_2\text{O}$	Yes	No
6	ZOA-4W	$\text{Zn}(\text{OAc})_2 + 4\text{H}_2\text{O}$	Yes	Yes

3.3.3 Role of capping agent

For the application of nanoparticles, control in the size and morphology of nanoparticle is essential. And, the synthesis of nanoparticles using a wet-chemical technique enables the use of surfactants to regulate the size and morphology of nanoparticle [123]. Oleic acid (OA) used as the capping agent is a long-chain amphiphilic molecule covalently bonded to a polar head and a non-polar hydrocarbon tail. The polar head interacts with the surface of the metal or metal oxide atom and the alkyl moiety with the solvent, Fig. 3.1. Due to the amphiphilic nature of the surfactant, it is a key component in the synthesis of nanoparticles in preventing the formation of clustered nanoparticles. The polar head group of OA, carboxyl group (-COOH), interacts with the hydroxide group (OH) on the surface of ZnO nanoparticles. Apart from keeping aggregation in check, the long-chain organic ligand imparts colloidal stability to the nanoparticles. As most nanoparticles are unstable in an environment coalescing or agglomeration etc. are the undesirable results we want to avoid. Therefore, the functionalisation of the surface of the nanoparticles enables stability to the nanoparticles and regulate growth and final particle size [124, 125]. In the absence of a surfactant, nanoparticles would form a continuous phase. Moreover, proper knowledge and understanding of the role played by a surfactant would open ways to manipulate the size and morphology of a nanoparticle by selectively choosing the right surfactant and varying its molar concentrations. In this work, three sets of reactions were performed to functionalise the metal oxide nanoparticle surfaces. The scheme of the experiments is shown in the table above, Table 3.1. Like the previous reactions, diethylene glycol (DEG) was used as a solvent, and the reaction conditions were as it was in section 3.3.1.

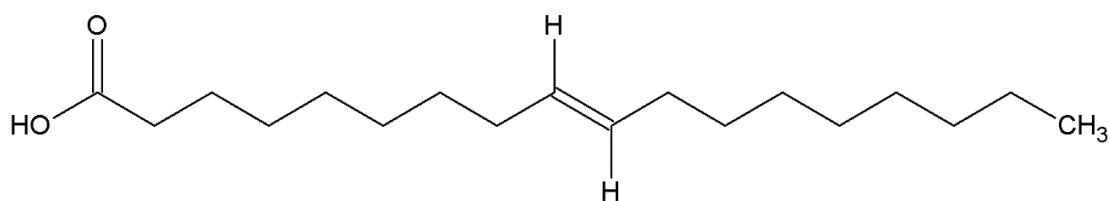


Fig. 3.1 Molecular structure of oleic acid.

3.3.4 ZnO nanoparticles with different particles sizes

The synthesis of nanocrystals in controlling its size has good and various applications due to its size-dependent properties. Several works are available in the literature where researchers optimised the reaction conditions in order to prepare nanocrystals of different sizes. It is, however, challenging to manipulate the growth during the reaction just by optimising the molar precursor concentration of a metal or metal oxide nanoparticles. Much work has been published in this field [126–128]. In this set of reactions, ZnO nanoparticles were

prepared from different molar concentrations of $\text{Zn}(\text{OAc})_2 \cdot 2\text{H}_2\text{O}$ (1 mmol, 2 mmol, 4 mmol and 8 mmol in 50 mL of the solvent), Table 3.2. The reactions were continued as described in the above-mentioned synthesis.

Table 3.2 Reaction scheme of ZnO nanoparticles at varied ZnO molar precursor concentrations.

Sl no.	Sample name	ZnO precursor	ZnO precursor molar conc. (mol/dm^3)	Capping agent
1	ZnO-1	$\text{Zn}(\text{OAc})_2 \cdot 2\text{H}_2\text{O}$	0.02	OA
2	ZnO-2	$\text{Zn}(\text{OAc})_2 \cdot 2\text{H}_2\text{O}$	0.04	OA
3	ZnO-3	$\text{Zn}(\text{OAc})_2 \cdot 2\text{H}_2\text{O}$	0.08	OA
4	ZnO-4	$\text{Zn}(\text{OAc})_2 \cdot 2\text{H}_2\text{O}$	0.16	OA

3.4 Synthesis of doped ZnO

Addition of impurities on the atomic level into the host phase is expected to modify the absorption and fluorescence property of ZnO nanoparticles. Variation in the optoelectronic properties is observed in the semiconductor nanoparticles [96, 129, 130]. Doping with transition metals like Fe^{3+} and Co^{2+} , alter the electronic structure of the host material [76, 131]. Moreover, ZnO is an n-type semiconductor and doping it with other electron-rich impurities increases the charge carriers of the semiconductor. The type of synthesis also plays a role in achieving efficient doping of semiconductor nanoparticles. As discussed previously, usage of the microwave reactor is an excellent method to synthesise nanoparticles, especially doped nanoparticles. The high-temperature reaction using the reactor and its rapid heating makes it efficient for getting better doping percentage [132–134]. The microwave radiation employed is effective as the synthesis is carried out under a controlled reaction environment (temperature, pressure and time) [135]. In addition, the use of high-boiling point polar solvent plays a crucial role in the rapid heating of the reaction mixture. The chapter focuses on the synthesis of doped-ZnO nanoparticles and the study of the dopants used. Fe, and Al are the metal atoms used for doping. For preparing doped ZnO nanoparticles, $\text{Zn}(\text{AOc})_2 \cdot 2\text{H}_2\text{O}$ was used as a precursor. A change in the band gap was observed in the semiconductor nanoparticles as evidenced in absorbance and emission spectra. Therefore, the semiconductor nanoparticles were successfully synthesised with the ultimate goal of tailoring the band gap.

The synthesis procedure is the same as mentioned in Section 3.3.1 with the difference in the addition and the amounts of dopants used prior to heating in the microwave reactor. For Fe-, and Al-doped ZnO nanoparticles, 1 %, 5 % and 10 % dopants were used and their optical and electrical properties examined. The percentage of doping relates to the degree of the zinc atom substitution in the formula $D_xZn_{(1-x)}O$, where D stands for dopant. Thus, 5 % means $x = 0.05$ for example. Iron and aluminium acetylacetonates were used as the source compounds for the doping. The labelling of the samples are as follows: Fe-1 Z, Fe-5 Z, Fe-10 Z, Al-1 Z, Al-5 Z and Al-10 Z for 1%, 5% and 10 % dopants respectively, Table 3.3.

Table 3.3 ZnO nanoparticles synthesis doped with Fe, Al and dopants.

Sl no.	Sample name	Dopant	Dopant (%)	Capping agent
1	Fe-1 Z	Fe	1	OA
2	Fe-5 Z	Fe	5	OA
3	Fe-10 Z	Fe	10	OA
4	Al-1 Z	Al	1	OA
5	Al-5 Z	Al	5	OA
6	Al-10 Z	Al	10	OA

3.5 Fillers in a conjugate polymer

In the preparation of nanocomposite, a dispersion obtained firstly is as follows, 10 mg of MEH-PPV polymer was dissolved in 3.5 ml of ZnO, Fe- Z, and Al- Z series of nanocolloidal solutions containing 10 mg of nanoparticle powder so that the polymer-to-nanoparticle ratio was 1:1 by weight. The solutions, ZnO/MEH-PPV, $Fe_xZn_{1-x}O$ /MEH-PPV, and $Al_xZn_{1-x}O$ /MEH-PPV were subjected to ultrasonic treatment and stirred overnight for obtaining fine dispersions. The prepared mixture was used as a precursor for thin film preparations by spin coating the solution on an ITO-coated glass substrate at 800 rpm for 15 seconds. The samples were then kept for drying in a vacuum oven at 100 °C for 2 hours. The solutions can be identified as, continuing from the previous notations, by adding letters ME (e.g. ZnO-1 ME for undoped ZnO nanoparticles and, Fe-1 ZME, and Al-1 ZME for Fe-doped and Al-doped respectively). Also, for comparison purpose, thin films were prepared from neat MEH-PPV and with the nanocomposite solutions from ZnO, Fe- and Al-doped ZnO samples.

3.6 PLED device fabrication

The compositions of the PLED device are electrodes (anode and cathode), hole-transporting layer (HTL) and an active layer. Indium tin oxide (ITO) is the anode that injects holes through an HTL layer made from (PEDOT:PSS) into the active layer from ZnO/MEH-PPV or doped ZnO mixed with MEH-PPV. Electrons are injected to the active layer from Mg cathode deposited on the top of the device structure. The scheme of the device is depicted in Fig. 3.2. As in the previous samples, the notations for the PLED device for ZnO, Fe-ZnO and Al-ZnO are represented as an example ZnO-1/MEH-PPV, Fe-1 Z/MEH-PPV, and Al-1 Z/MEH-PPV respectively.

Spin coating (Laurell WS-650-MZ-23NPP) method was used to prepare thin films of nanometer size thicknesses. In the device fabrication process, the HTL layer (PEDOT:PSS) was coated on a pre-patterned ITO-coated glass substrate to obtain a homogenous thin film. Later, the prepared nanoparticle dispersions (ZnO/MEH-PPV), were deposited onto the HTL layer by spin coating at 1000 rpm and dried in a vacuum oven at 150 °C in order to prepare the active layer. It is then followed by the sputtering of magnesium on the top of the layered structure. An instrument used for sputtering was Quorum Technologies Q300TT. Finally, the device was encapsulated by epoxy resin in order to protect the deposited layers from moisture and prevent contamination. The fabrication of the polymer light-emitting diode (PLED) was performed in a glove box JACOMEX GP Concept, keeping a relative partial pressure of H₂O and O₂ below 10 ppm.

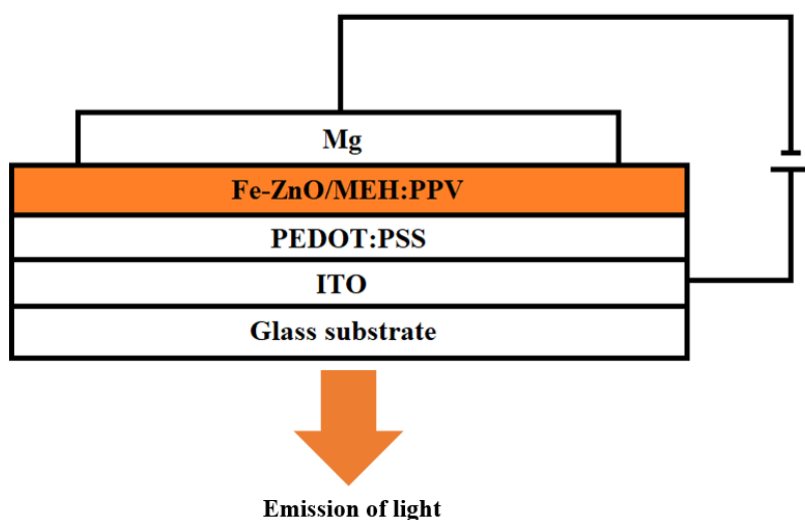


Fig. 3.2 Schematic diagram of Fe-doped ZnO PLED device [131].

4. RESULTS AND DISCUSSIONS

The results and discussions are organised into sections according to the fivefold aims of the thesis. The first four chapters represent original research on nanoparticle synthesis and properties, while the fifth chapter is added to demonstrate the application potential of the synthesised particles in LEDs.

4.1 Undoped ZnO nanoparticles, the role of water and capping agent

In this study, hydrated and anhydrous zinc oxide precursors were used to synthesise ZnO powders. When anhydrous ZnO precursor was used, equivalent molar amount(s) of de-ionised water was added to compare the products obtained.

Oleic acid was introduced to the reaction mixture directly to obtain the product in one step. ZnO nanoparticles preparation without the capping agent was used as a reference. After the reaction, the synthesised nanoparticles are to be dispersed in toluene. Such dispersions are intended for preparing nanocomposite by blending it with the solution of conducting polymer MEH-PPV.

4.1.1 XRD analysis

The XRD patterns of the samples are shown in Fig. 4.1. All the peaks have hexagonal wurtzite crystal structure in line with the database (JCPDS 36-1451). The average sizes of the diffracting nanocrystallite structure were determined by using Scherrer's formula, Equation 3.2. Precision about ± 1 nm is expected. Therefore, the values are rounded to units. In both cases (ZNP and ZOA sample series), the crystalline core of the nanoparticle is taken into account in this analysis and the presence or absence of the surfactant shell on the surface of the particle does not influence the obtained values. The thickness of an oleic acid monolayer can be roughly estimated in the range 2-3 nm. Samples ZOA-CW (11 nm) and ZOA-NW (9 nm) have a small crystallite size difference, but the size of crystallites in sample ZOA-2W (18 nm) is two times bigger than those in sample ZOA-NW (9 nm), Table 4.1. The reason could be attributed to the addition of de-ionised (DI) water which could have led to the growth of crystals during nanoparticle formation [136]. In ZOA-CW, the water molecules present in the form of dihydrate do not seem to influence much at the time of particle synthesis. However, water molecules do play a significant role as it assists the hydrolysis of the zinc precursor in the initial stage of the synthesis. The ZNP samples show similar yet less pronounced patterns. The particle size increases in the series as well, from ZNP-NW (9 nm), ZNP-CW (13 nm) up to ZNP-4W (16 nm). It seems that there is a cooperative effect of the presence of water and capping agent in the reaction mixture.

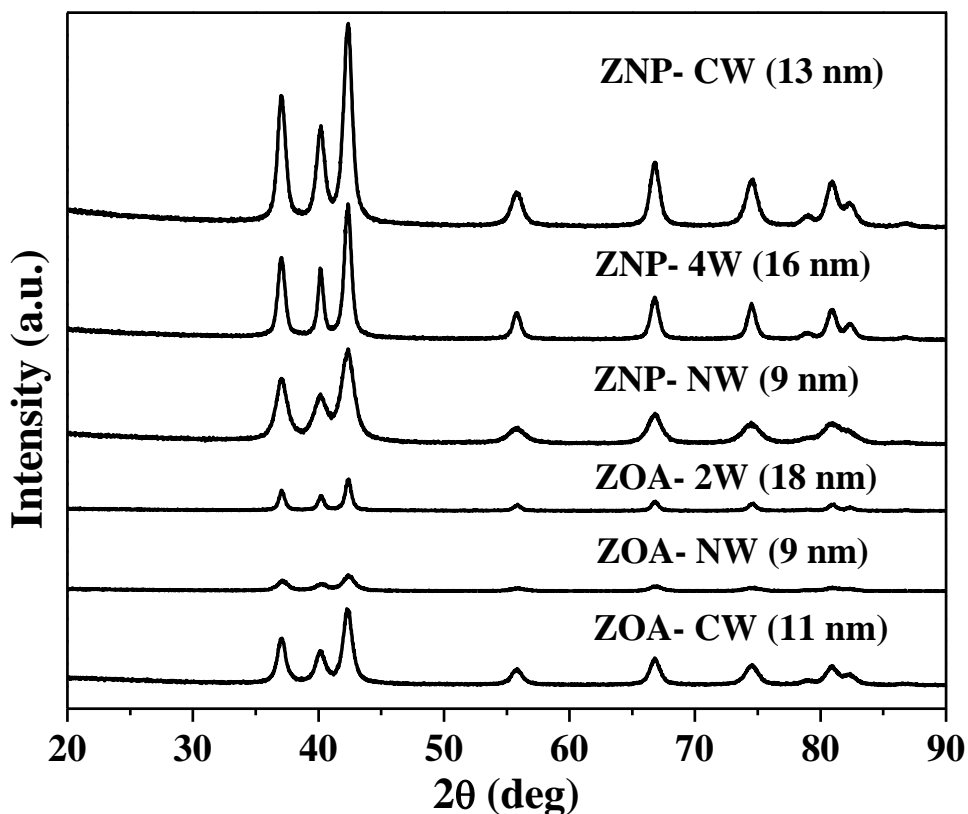


Fig. 4.1 XRD diffractogram of ZnO nanoparticles.

4.1.2 TEM analysis

TEM analysis revealed a striking contrast when ZnO was synthesised with and without the capping agent, i.e. oleic acid. When the capping agent is used, it forms an organic layer on the surface of the nanoparticle. The layer reduces the surface energy, and the particles can be dispersed well in a non-polar solvent. TEM confirms the importance of the organic ligand used, Fig. 4.2. The images of the ZNP samples show the formation of clusters when synthesised without oleic acid. Expectedly, the presence of oleic acid was manifested in the other set of samples (ZOA-2W, ZOA-NW and ZOA-CW) due to uniform distribution of particles as no agglomeration was observed.

As published in the literature [100] and elaborated in the case of iron oxide (Fe_2O_3) nanoparticles for cationic surfactants, a surfactant used as capping agent has a role to play in controlling the size of the nanoparticles. The particle size is given by the ability of the constitutive ion(s) to penetrate the surfactant layer. This single parameter depends on the length of the alkyl chain of the surfactant. The role of oleic acid (18 carbon atoms long chain, anionic surfactant) was confirmed for ZnO in this study as well. Moreover, a synergy with the presence of water molecules was manifested in this experiment when the effect was studied for small stoichiometric concentrations. Studies previously published for the ethanol/water system did not reveal such effect due to a large concentration of water in the system and without the addition of a surfactant [120]. In the waterless system, there is no effect of the surfactant on the particle size since the hydrolysis

of the precursor is too limited and, thus, the ionic permeability is not the governing mechanism. When some molar amount of water molecules are present in the system, the role of the surfactant becomes more pronounced. We can hypothesise that its presence (water) simply helps the transport of ions or that the water molecules concentrates inside the cores of micelles formed by the surfactant. The latter hypothesis would relate to the size of particles with initial micelle size and precursor hydrolysis. On the other hand, the effect on the agglomeration of particles is crucial as one may expect, and the TEM analysis well documented it.

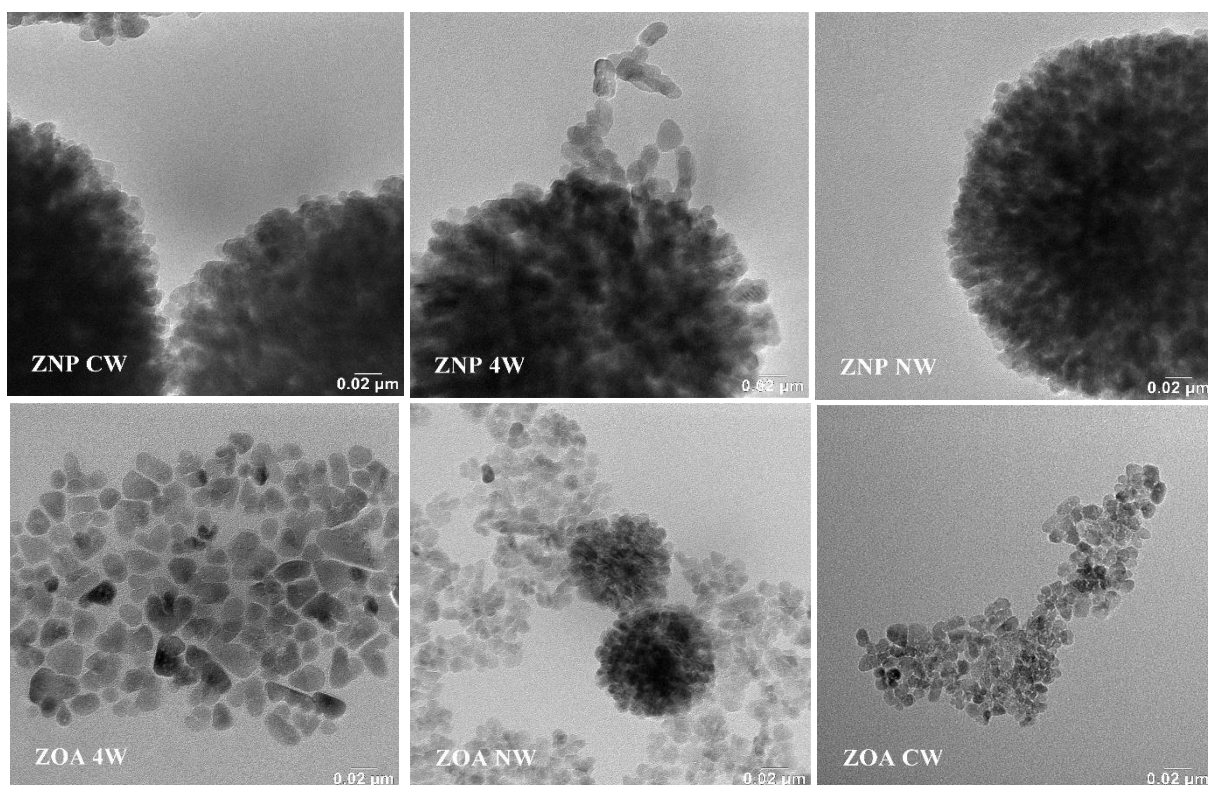


Fig. 4.2 Analysis of water and oleic acid on different ZOA and ZNP samples observed in TEM images.

4.1.3 UV-Vis and DRUV-Vis spectroscopy

The diffuse reflectance spectra of undoped ZnO samples (both ZNP and ZOA series) measured at room temperature are shown in Fig. 4.3. It can be seen from the graph that pure ZnO samples prepared in the absence of water (ZNP-NW and ZOA-NW) has higher reflectance compared to the ones synthesised with water. To determine the band gaps of the samples, Tauc plots (Fig. 4.4) were used as obtained from DRUV-Vis spectra. The extrapolation of Tauc plot, $[F(R) \cdot hv]^2$, on the y-axis and the photon energy hv , on the x-axis, gives us the band gap of the semiconductor nanoparticles as described in Equation 3.4. The band gap widths of the samples can be seen in Table 4.1. The variation in the band gap observed for samples ZOA is eminent. From the table below, the estimated band gap of ZOA NW is 3.22 eV and, it increases with increasing molar stoichiometric

content of water molecules. However, the band gaps of ZNP samples are similar despite varying molar amount of water molecules.

Table 4.1 Average particle size and band gaps of different ZnO samples.

Sl no.	Sample name	Average particle size (nm)	Band gap (eV)
1	ZOA-CW	11	3.34
2	ZNP-CW	13	3.23
3	ZNP-NW	9	3.25
4	ZOA-NW	9	3.22
5	ZNP-4W	16	3.22
6	ZOA-4W	18	3.18

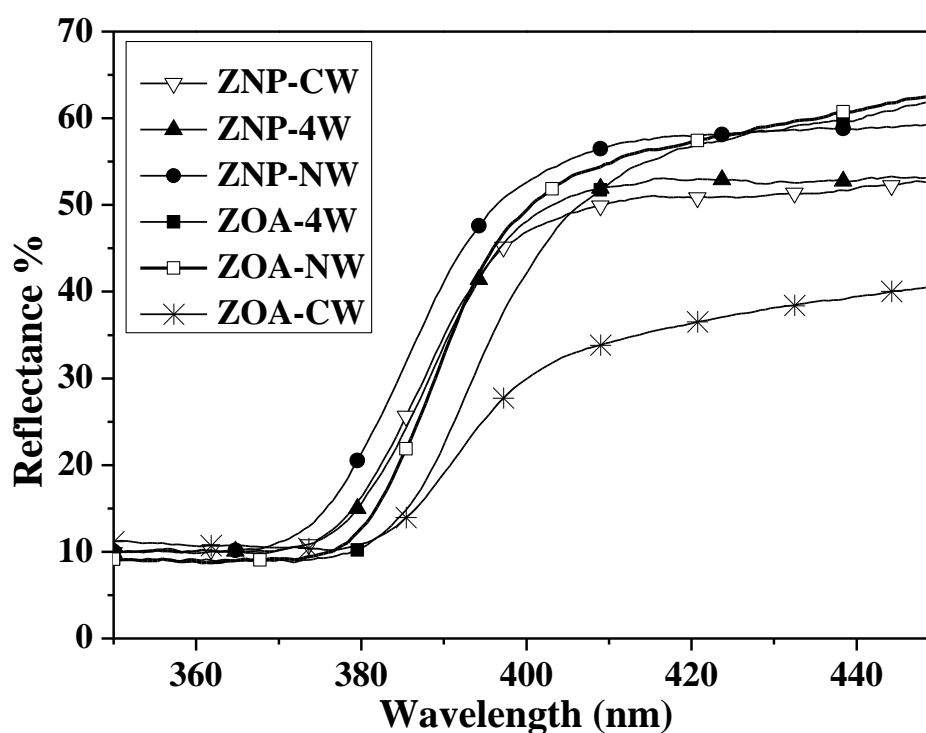


Fig. 4.3 DRUV-Vis of powdered ZnO nanoparticles in different reaction conditions.

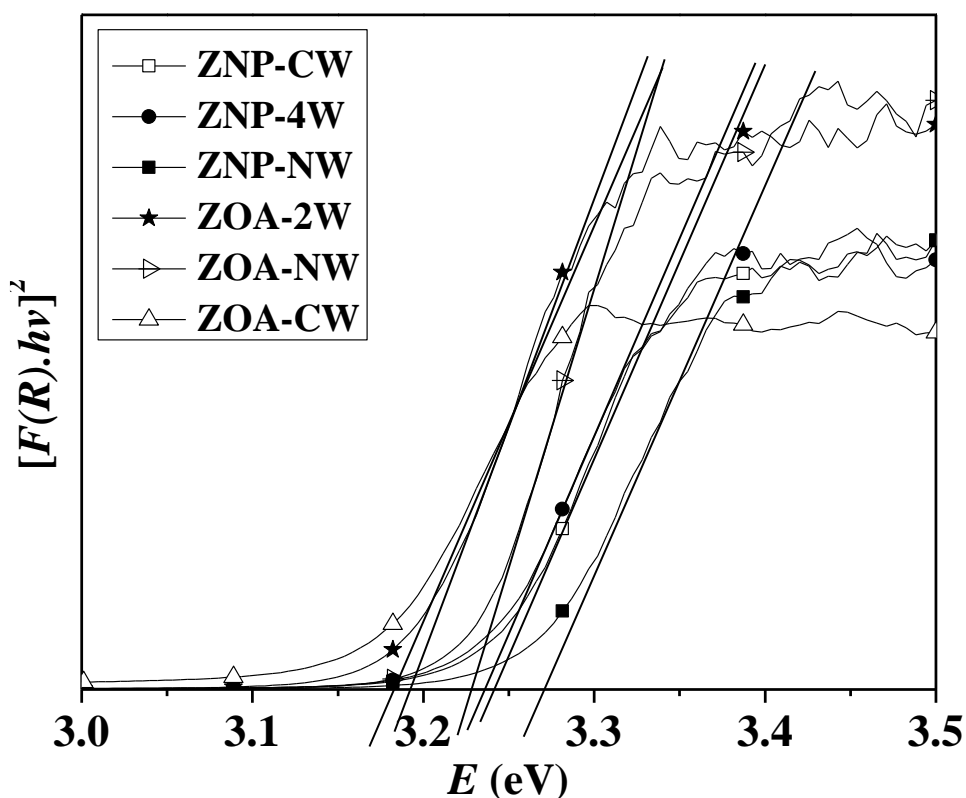


Fig. 4.4 Tauc plot of ZNP and ZOA powdered sample.

4.1.4 Photoluminescence spectroscopy

The fluorescence spectra of ZnO nanoparticles, usually, consist of two characteristic peaks. The near-band-edge (NBE) emission around 380 nm corresponds to band gap excitonic emission. This relatively sharp peak is manifested in spectra of well-crystallised material. The second emission peak falls in the visible region 500 to 800 nm [137]. This broadband emission is due to the imperfections caused by various defects in the crystal. Emission in the green-yellow region is associated with the singly ionised oxygen vacancies.

In these set of samples, the normalised photoluminescence (PL) spectra (excitation at 332 nm) of ZNP and ZOA sample series is depicted in Fig. 4.5. The emission in the UV region (372 nm to 381 nm) is due to the near-band-edge transition (NBE). The tails in ZNP samples (354 nm to 364 nm) are due to the scattering of the monochromatic laser source. The excitation laser light is much more scattered by the large nanoparticle aggregates than by the individual nanoparticles present in dispersions of ZNP samples. A blue shift can be seen in the case of ZNP samples. No broadband emission in the visible region was observed which testifies for good crystallinity of prepared nanoparticles and low concentration of active defects. At least, surface defects (vacancies) can be naturally expected in nanoparticles. However, they can be passivated by both OA surfactant and DEG solvent residuals.

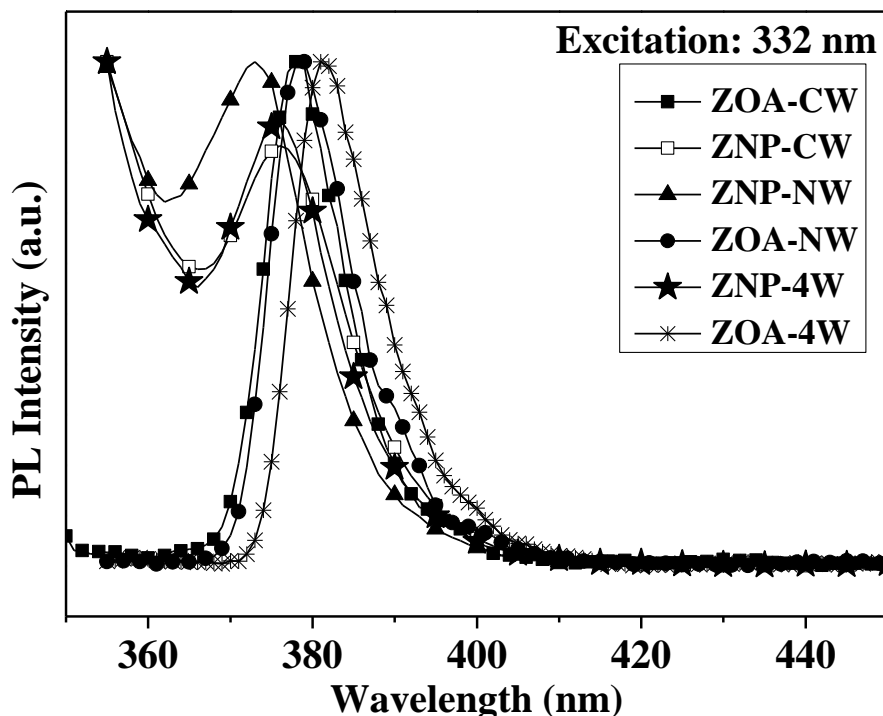


Fig. 4.5 Normalised room temperature PL emission spectra of pure ZnO samples.

4.1.5 FT-IR spectroscopy in MIR and FAR region

Fig. 4.6, and Fig. 4.7 show the FT-IR in the MIR (mid-infrared) and FIR (far infrared) region of the undoped ZnO series (ZNP and ZOA) of samples. From the graph in Fig. 4.6, all samples exhibited strong vibrational stretching below 500 cm^{-1} [138]. It is actually a shoulder of the FIR peak, as seen in Fig. 4.7., where the maximum absorbance of ZnO is observed in $322\text{ to }373\text{ cm}^{-1}$ region. The broad absorption band observed around 3375 cm^{-1} is due to hydroxyl group (—OH) stretching vibration. It can be both from water molecules or surface hydroxyl groups. These groups could be from the dihydrate of ZnO precursor, the addition of deionised water, or residual solvent traces [139]. Alternatively, it could be due to adsorbed moisture on the surface of nanoparticles.

Additionally, the $\text{—CH}_2\text{—}$ group vibrations in the hydrocarbon moiety were observed at 2920 and 2853 cm^{-1} . These absorption bands are weak in the spectra of ZNP samples (manifesting only residues of the solvent) but very well defined and intensive in the spectra of ZOA samples due to the presence of hydrocarbon chains in oleic acid. The carboxylate group stretching vibrations peaks were found to be at 1557 and 1420 cm^{-1} [139]. Also, a difference between ZNP and ZOA samples can be found. While the peak doublet is of low resolution in ZNP samples testifying for inorganic carbonates on the nanoparticle surface, the peak doublet has fine structure indicating well-defined carboxyl groups of oleic acid attached to the surface of the nanoparticles, as can be expected according to its function as a capping agent.

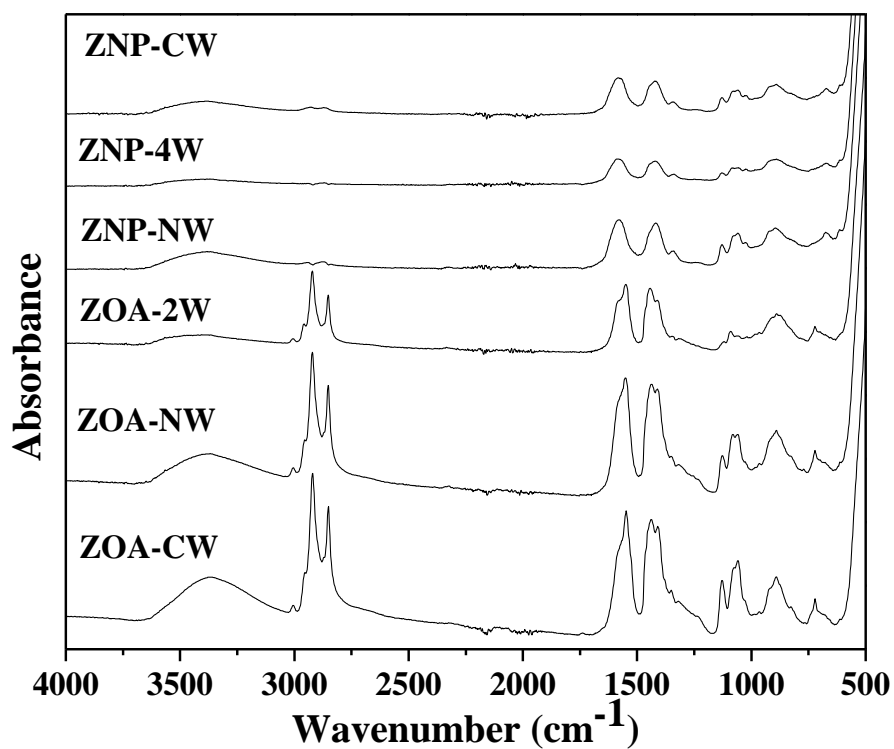


Fig. 4.6 FT-IR of ZnO nanoparticles in MIR region.

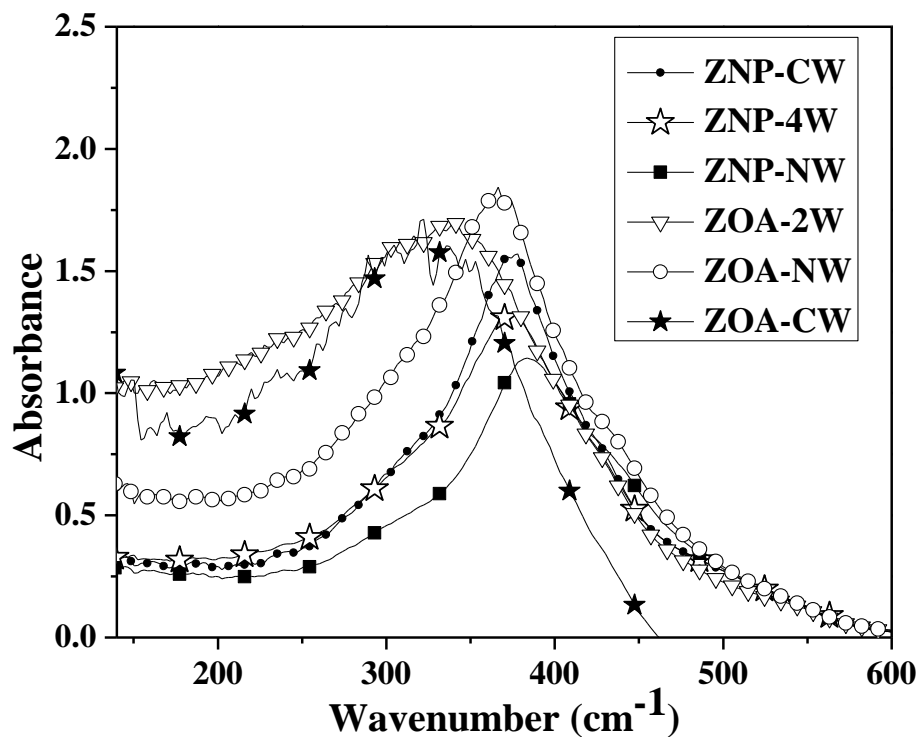


Fig. 4.7 FT-IR spectra of ZnO ZNP and ZOA samples in FIR (far infrared) region.

4.2 ZnO nanoparticles with different precursor molar concentration

ZnO nanoparticles with different particle sizes come with varied properties. The other set of samples (ZnO-1, ZnO-2, ZnO-3 and ZnO-4) are undoped ZnO prepared with different ZnO precursor molar concentrations, Table 3.2

4.2.1 XRD analysis

The results of the XRD analysis of ZnO nanoparticles are shown in Fig. 4.8. The observed diffraction patterns match well with standard JCPDS file for ZnO (JCPDS 36-1451) of wurtzite hexagonal crystal structure. Presence of no other crystalline phase was manifested. In order to determine the average crystallite size of the powdered samples, Scherrer's equation was employed, Equation 3.2. The full-width half maxima (FWHM) of the most intense peak, (101), was chosen to calculate the average crystallite size of the samples. The average crystallite sizes were calculated to be 7 nm, 9 nm, 12 nm and 17 nm for ZnO-1, ZnO-2, ZnO-3, and ZnO-4 respectively. It is also clear from the diffractograms that with an increase in the average crystallite size, the intensity of the peaks is more pronounced. Moreover, the sharpness of the peaks indicates high crystallinity of the as-synthesised nanoparticles, except for the smallest crystallites in sample ZnO-1. Note that, the crystallite size analysed from XRD spectra may differ from particle size from TEM micrograph [140].

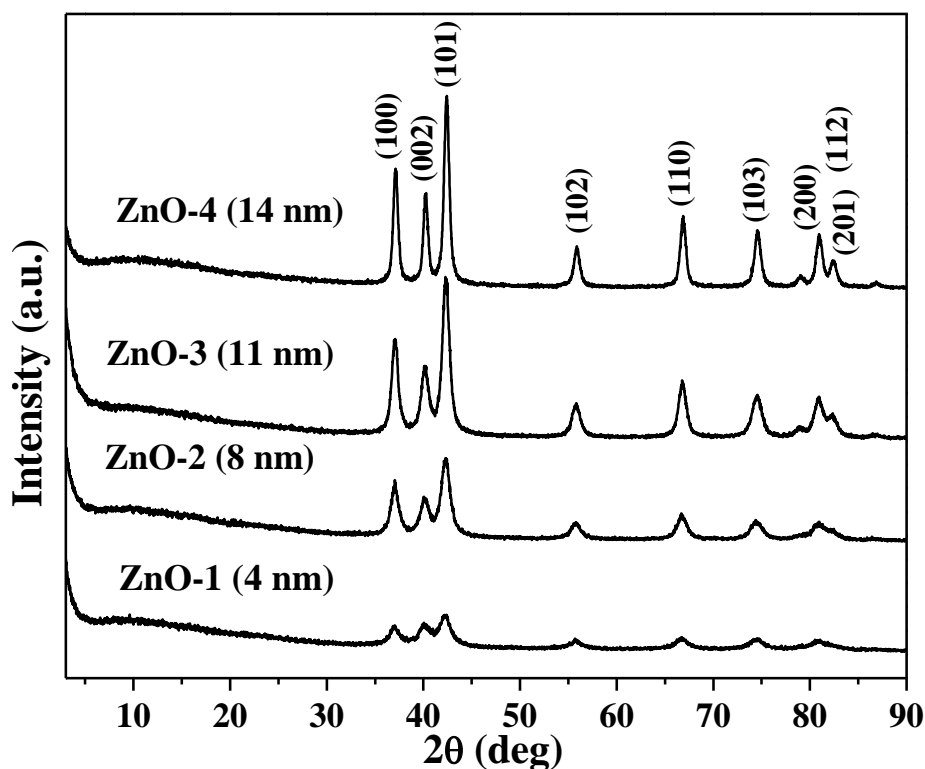


Fig. 4.8 XRD peaks of ZnO-1, ZnO-2, ZnO-3 and ZnO-4 [141].

4.2.2 TEM micrograph analysis

The morphology and size distribution was studied by taking the TEM image of ZnO nanoparticles, Fig. 4.9. The figures below document increasing particle size with increasing ZnO precursor molar concentration from 0.02 mol/dm^3 to 0.16 mol/dm^3 . The fine dispersion of the nanoparticles is also confirmed by this characterisation technique. In addition, the nanoparticle sizes from the TEM images correspond with the obtained XRD values, see Table 4.2. It can be due to the positive influence of the precursor concentration on both the nucleation rate and the nanoparticle growth rate. Although one would expect the particle diameter obtained from TEM to be larger than that from XRD analysis, they seem to be non-distinguishable within the estimation error. It can be due to poor stability of the OA shell under the conditions of TEM observation. Concerning the stability of the dispersed nanoparticles, the TEM results are further substantiated by the light scattering technique of the dispersed nanoparticles, as explained in the following section.

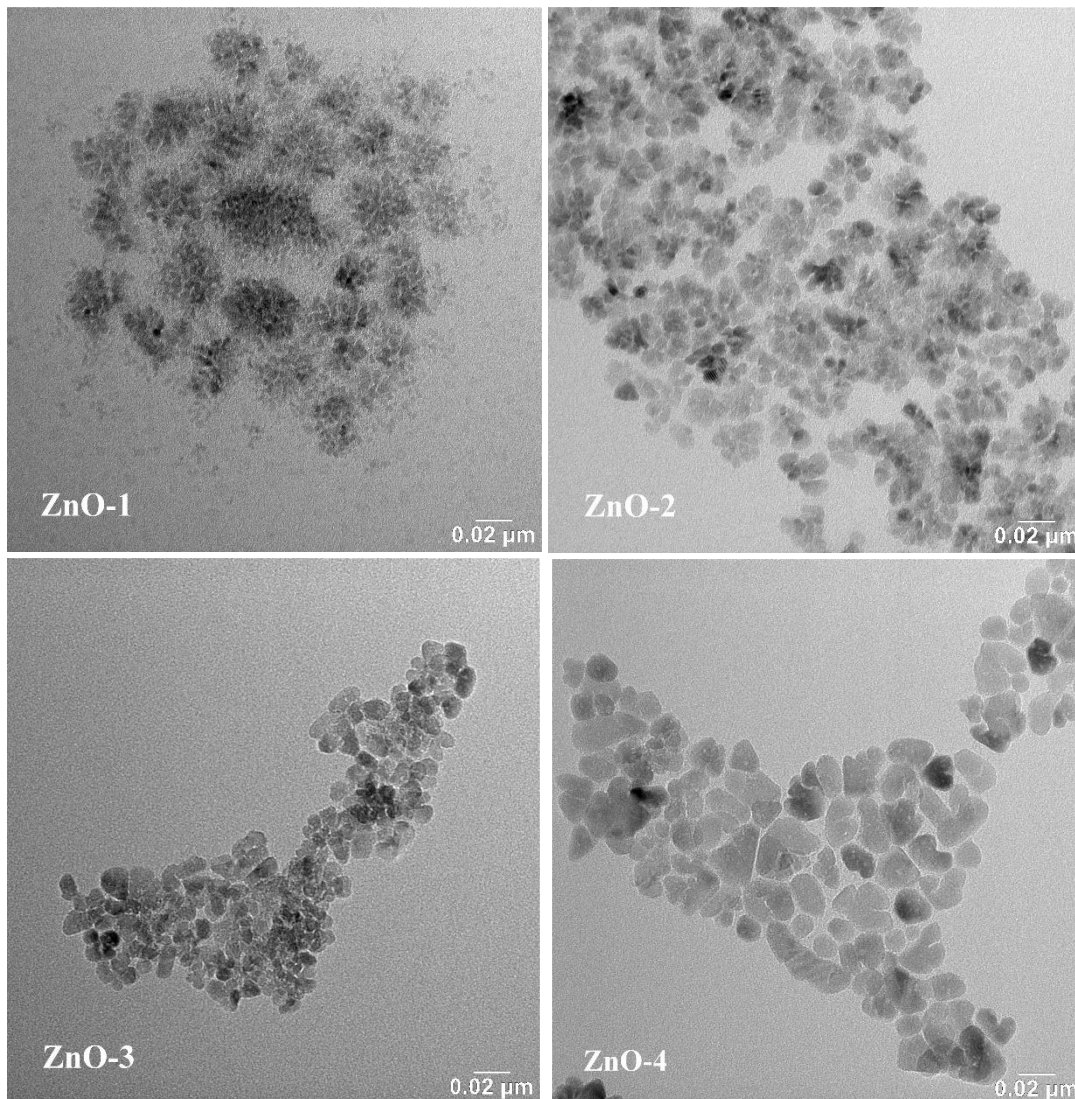


Fig. 4.9 TEM micrographs of ZnO samples [141].

4.2.3 Analysis of hydrodynamic diameter of ZnO colloidal samples

With dynamic light scattering (DLS) technique, the dispersion of different average particle size ZnO in toluene was analysed, Fig. 4.10, Fig. 4.11, Fig. 4.12, and Fig. 4.13. This characterisation method tells us about the stability of the synthesised nanoparticles in a liquid medium, toluene in this study. As seen from the figures, the hydrodynamic diameter of the ZnO samples is significantly bigger when compared to the average particle size analysed by TEM micrographs. This is due to the interaction of the surface-modified ZnO with its surrounding environment. The long-chain organic molecule, oleic acid, bound to the surface of the nanoparticles, enables colloidal stability by interacting with toluene. As can be seen from the graph, ZnO-1 sample has a hydrodynamic diameter about 52 nm and the rest of the samples in 40-46 nm ranges, also refer Table 4.2. This is expected as the recorded average particle size of ZnO-1 is about 4 nm. Due to its large surface-to-volume ratio, they tend to form agglomerates leading to a larger hydrodynamic diameter of the samples.

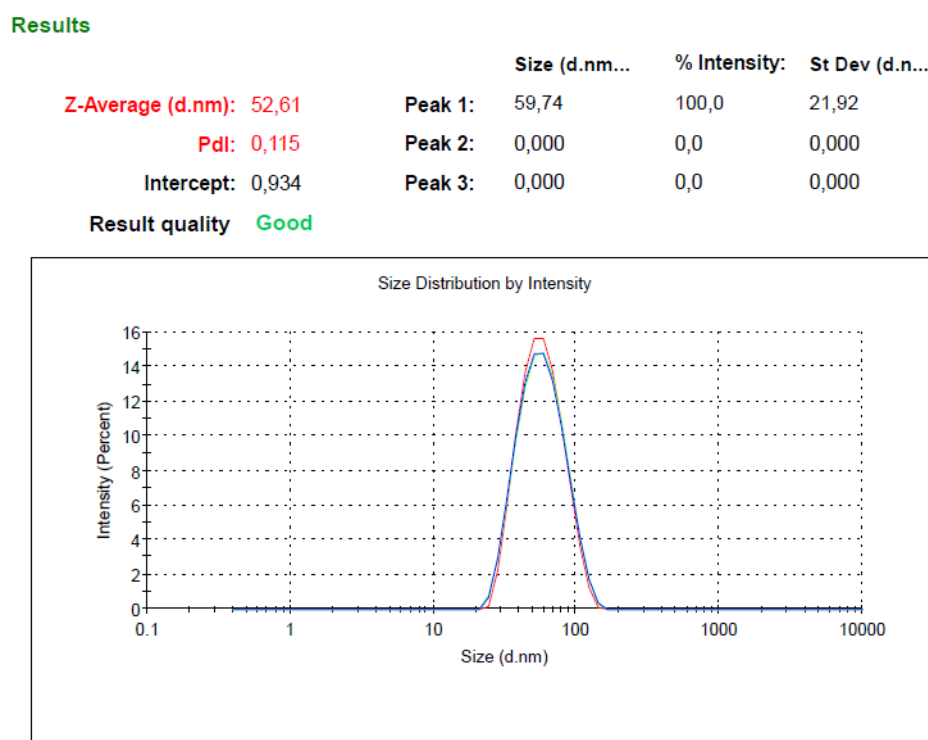


Fig. 4.10 DLS of ZnO-1 colloidal dispersion (graphical output as obtained from the dedicated original data processing software).

Results

	Size (d.nm...)	% Intensity:	St Dev (d.n...
Z-Average (d.nm): 46,90	Peak 1: 55,06	100,0	22,95
Pdl: 0,140	Peak 2: 0,000	0,0	0,000
Intercept: 0,938	Peak 3: 0,000	0,0	0,000

Result quality Good

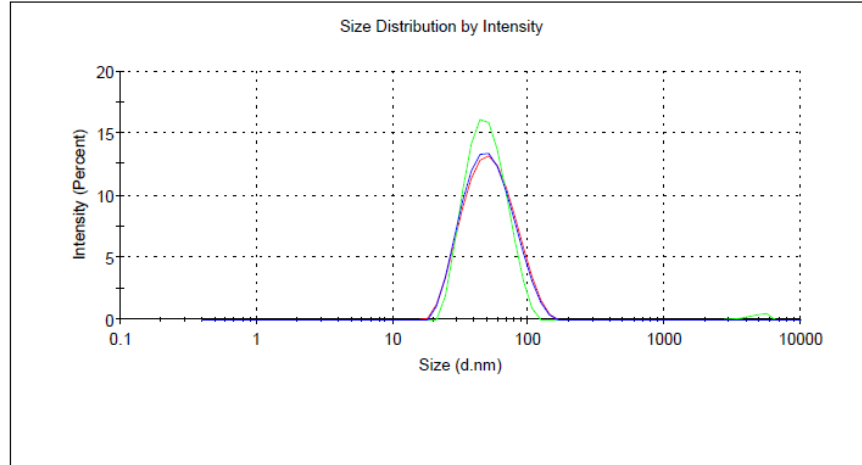


Fig. 4.11 DLS of ZnO-2 colloid (graphical output as obtained from the dedicated original data processing software).

Results

	Size (d.nm...)	% Intensity:	St Dev (d.n...
Z-Average (d.nm): 40,62	Peak 1: 45,22	97,5	18,68
Pdl: 0,196	Peak 2: 4636	2,5	814,5
Intercept: 0,906	Peak 3: 0,000	0,0	0,000

Result quality Good

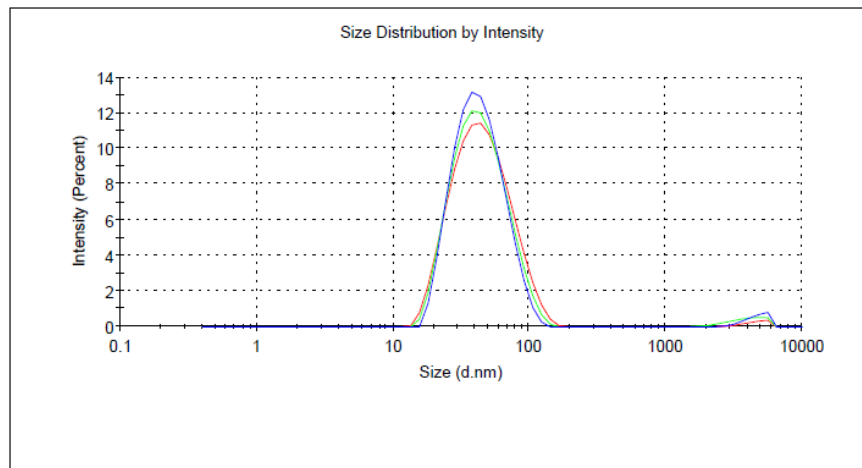


Fig. 4.12 DLS of ZnO-3 dispersion (graphical output as obtained from the dedicated original data processing software).

Results

	Size (d.nm...)	% Intensity:	St Dev (d.n...
Z-Average (d.nm): 46,80	Peak 1: 54,59	97,9	24,99
Pdl: 0,194	Peak 2: 4210	2,1	999,8
Intercept: 0,898	Peak 3: 0,000	0,0	0,000
Result quality Good			

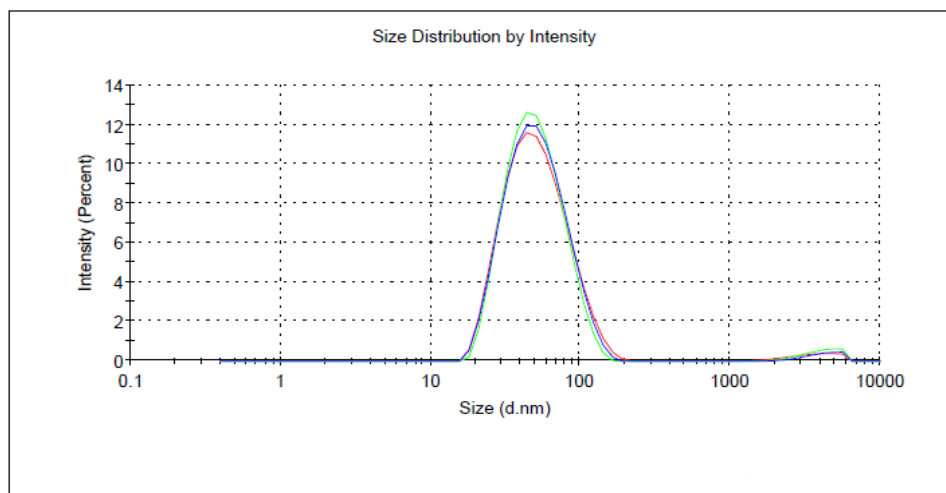


Fig. 4.13 DLS of colloidal dispersion of ZnO-4 (graphical output as obtained from the dedicated original data processing software).

Table 4.2 DLS analysis, average particle size and crystallite size of ZnO samples.

Sample	Z- Average diameter (nm)	Peak maxima	PdI	XRD average crystallite size (nm)	TEM average particle size (nm)
ZnO-1	52.61	59.74	0.11	7	4±3
ZnO-2	46.9	55.06	0.14	9	8±2
ZnO-3	40.62	45.22	0.19	12	11±1
ZnO-4	46.80	54.59	0.09	17	14±3

4.2.4 TGA study of ZnO powdered sample

An exemplary sample was characterised by simultaneous TGA/DSC, see Fig. 4.14. The mass loss observed at around 380 °C to 400 °C in air atmosphere heated up to 1000 °C is due to the decomposition of OA molecules bound to the surface

of ZnO nanoparticles. The DSC curve complements the TGA mass loss percentage showing exothermic effects above 380 °C.

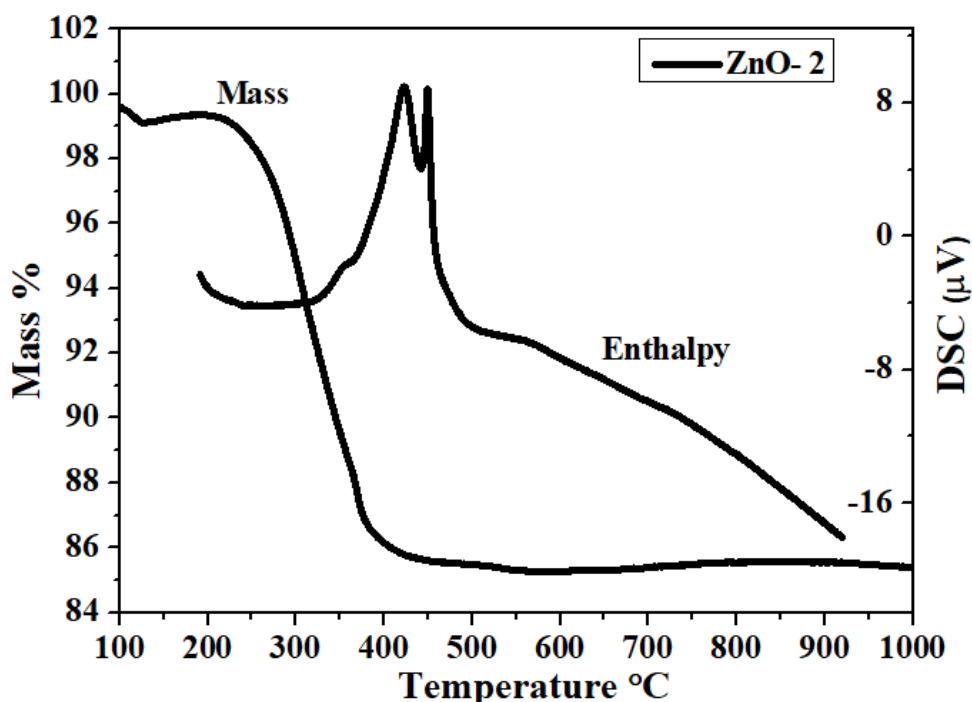


Fig. 4.14 TGA of ZnO- 2.

4.2.1 UV-Vis absorption spectra and Tauc plot

UV-Vis and Tauc plot spectra in Fig. 4.15 and Fig. 4.16 depict the optical properties of the samples. The ZnO nanoparticles were dispersed in toluene, diluted during the sample preparation, and then the solutions were used to perform the UV-Vis measurement. The spectra of the samples show a typical ZnO absorption maxima peaks at wavelength c.a.355 nm. This is attributed to the intrinsic band gap absorption of the nanoparticles due to the transition of the excited electrons from the valence band to the conduction band. It can be explained from the intensity of the absorption maxima peaks that the different particle sizes of ZnO samples allowed the absorption maxima peaks to shift to higher wavelengths. Moreover, the absorption edge symmetrically shifts to higher wavelengths with increasing size of the nanoparticles [142]. This pronounced shift in the absorption edge is due to the quantum size effect. The samples ZnO-1, ZnO-2, ZnO-3 and ZnO-4 have average particle size about 4 nm, 8 nm, 11 nm and 14 nm respectively, as analysed from TEM micrograph. The change in molar precursor concentration led to the variance in the average particle size. Further, the decrease in band gap (as evident from the Taucs plot Fig. 4.16), associated with particle growth and agglomeration, was also confirmed by TEM images.

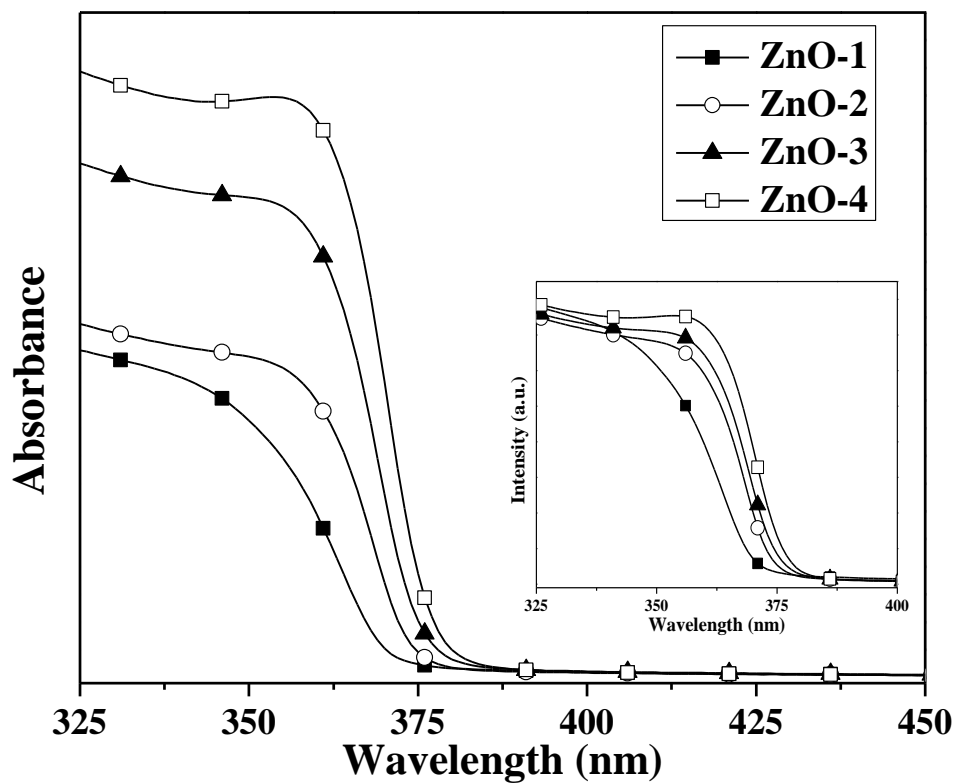


Fig. 4.15 UV-Vis absorption spectra of colloidal ZnO samples (inset: normalised curve) [141].

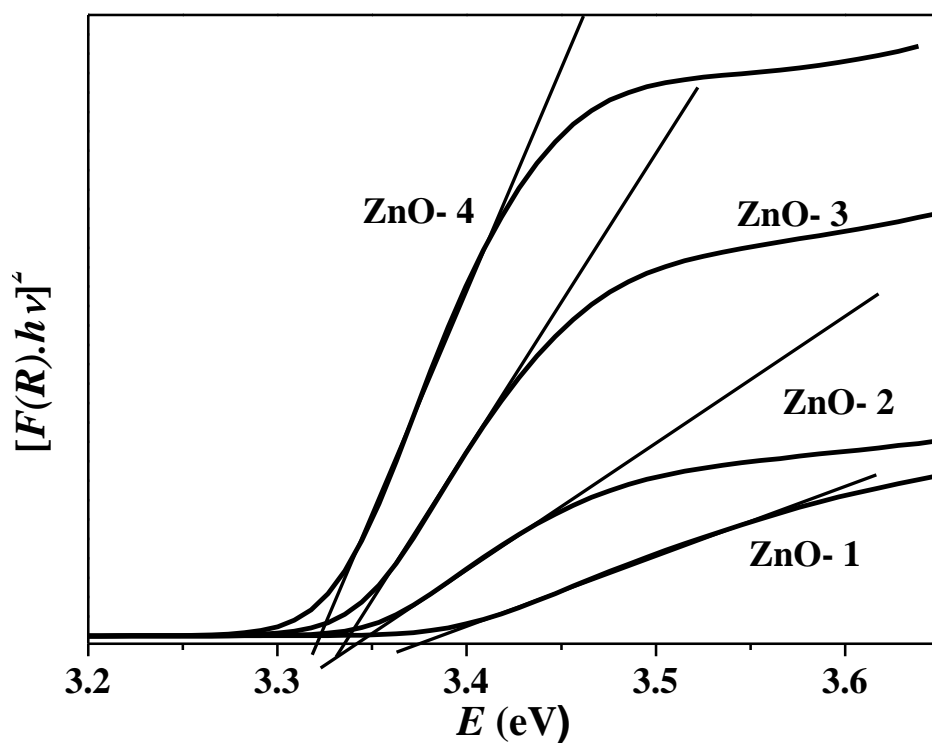


Fig. 4.16 Tauc plot of ZnO powdered samples [141].

Table 4.3 Correlation of band gap (from Tauc plot), average particle size (TEM) of ZnO samples.

Sample name	Avg. particle size (TEM) (nm)	Band gap (eV)
ZnO-1	4±3	3.38
ZnO-2	8±2	3.34
ZnO-3	11±1	3.33
ZnO-4	14±3	3.32

4.2.2 Fluorescence spectroscopy of ZnO colloidal samples

The room temperature PL spectra and normalised peaks, inset, of ZnO samples are shown in Fig. 4.17 (excited by a laser at 332 nm). The spectra observed at 370-380 nm is attributed to UV near-band-edge emission due to excitonic recombination. Moreover, the peaks also shift to higher wavelength (red-shift) as the particle size is increased. The maxima values of the peaks are recorded in Table 4.3.

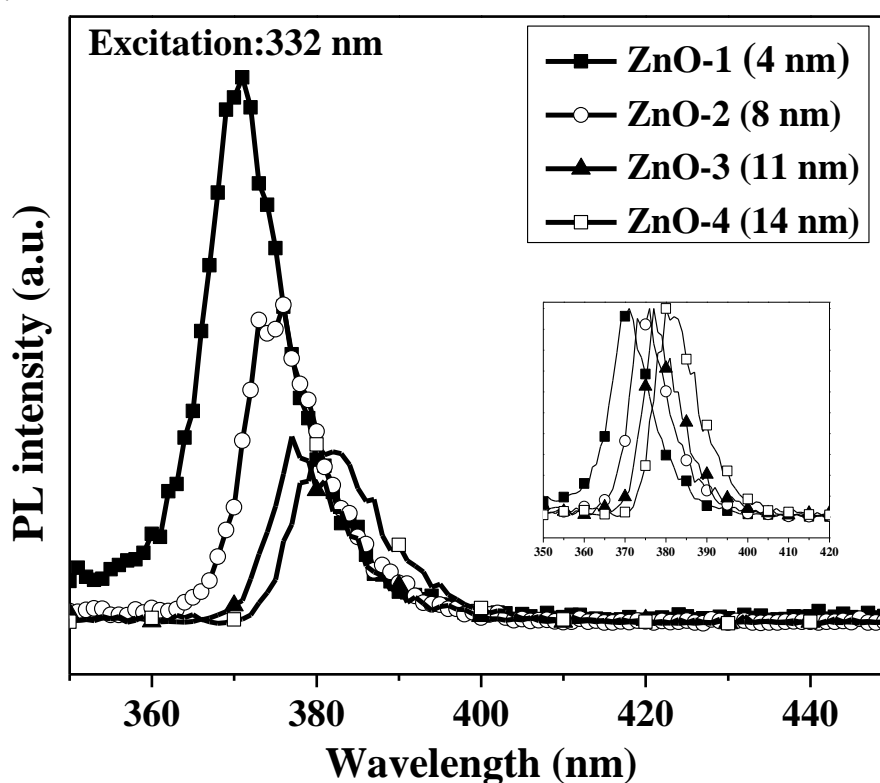


Fig. 4.17 Room-temperature fluorescence spectra of ZnO colloidal samples (inset: normalised peaks) [141].

4.2.3 Analysis of size dependent spectral features

Here, the Brus equation is employed to calculate the relation between the size of the semiconductor nanoparticles and its electronic structure [143]. The calculation is based on effective mass approximation (EMA). In order to understand the behaviour of electron and hole system, Brus' model approximated that the nanocrystal is spherical with radius r and the potential energy barrier outside the nanocrystal is infinite. The mass of electron and hole is replaced with effective masses (m_e^* and m_h^*) to define the wave function. The nanoparticles display quantum confinement effect depending on their size in the range of nanometres. The band gap of nanoparticles showing this quantum effect depends on the band gap of corresponding bulk materials as in Equation 4.1. If we consider the Coulombic attraction of the electron-hole pair, the transition energy is less than the band gap of the nanoparticles. The third term in Equation 4.2 accounts on that exciton bounding energy. Thus, the UV-Vis absorption and PL emission peak are blue-shifted on decreasing the size of the nanoparticles.

$$E_{g(tr)} = E_{g(nano)} - \frac{1.786 e^2}{4\pi r \epsilon_0 \epsilon} \quad 4.1$$

$$E_{g(tr)} = E_{g(bulk)} + \frac{h^2}{8r^2} \left(\frac{1}{m_e^*} + \frac{1}{m_h^*} \right) - \frac{1.786 e^2}{4\pi r \epsilon_0 \epsilon} \quad 4.2$$

where,

- $E_{g(tr)}$ = energy needed to create the lowest energy exciton,
- $E_{g(nano)}$ = band gap of a semiconductor nanoparticle,
- $E_{g(bulk)}$ = band gap energy of the bulk semiconductor,
- h^2 = Planck's constant,
- r = radius of the semiconductor,
- m_e^* = effective mass of excited electron,
- m_h^* = effective mass of excited hole.

The effective mass coefficient of an electron in ZnO is 0.24, and the effective mass coefficient of a hole is 0.59 [143, 144]. The energy band gap, $E_{g(bulk)}$, is characteristics of a material and, for bulk ZnO it is estimated to be around 3.4 eV [145]. In the ZnO samples, the corresponding values of band gap from Brus equation and experimental values are shown in Table 4.4 and Table 4.5, respectively. The band gap calculated from Brus equation of the ZnO samples vary slightly from the experimental values. Nevertheless, it shows the same trends as observed. The best agreement between theory and experiment was found for PL emission. The wavelength at the PL emission maximum blue-shifts slightly with decreasing size of the particles. The band gap width is predicted with lesser success but the trend is correct as well. The equation seems to exaggerate the blue-

shifts for smallest particles. Four principal sources of the observed discrepancy must be stressed out. First, The Brus' model yields wavelengths fairly close to experimental ones for larger nanoparticles in general [146]. Second, the examined size range covers a transition between weak and moderate confinement regimes. ZnO has a small Bohr radius (ca 1.8 nm). Thus the strong quantum confinement applies for particles smaller than ca 4 nm, and moderate quantum confinement regime spans approximately from 4 to 15 nm [147]. The third reason of the apparent failure is the extreme sensitivity of the model to the values of input constants. In the literature, one may find values of the bulk band gap varying from 3.30 to 3.45 eV. Similarly, the effective hole mass coefficient varies from 0.20 to 2.45 eV, depending on the method of experimental estimation or theoretical calculation, the value differs for different crystallographic orientation as well due to anisotropy of wurtzite. The same situation is for the effective electron mass coefficient varying from 0.13 up to 0.30 [148]. Changing these constants shift the predicted dependency of E_g on the particle size up and down. The fourth and major source of error is the uncertainty of particle size estimation. The Brus model curve becomes slopy for small particle radii. Thus, the impact of error in particle size increases drastically with decreasing particle size. Besides the error of particle size estimation, one must take into account the particle size distribution since the model assumes monodisperse particles only.

The polydispersity influences not only the model but complicate the evaluation of experimental data as well. Specifically, broadening of the absorption peak reduces the sharpness and readability of the spectra. The peak may even vanish if the distribution of the band gap energies is too wide. On the other hand, PL emission may be size-selective due to quantum yield (lifetime) dependency on the particle size discriminating thus the bigger fractions which yields red-shift of the PL maximum.

Table 4.4 Band gap values, absorption maxima peaks and emission maxima peaks as calculated from Brus equation.

Sample	Avg. particle size (nm)	Brus equation			
		$E_{g(nano)}$ (eV)	UV-Vis λ_{max}^* (nm)	$E_{g(exciton)}$ (eV)	PL emission λ_{max}^* (nm)
ZnO-1	4±3	3.85	322	3.50	354
ZnO-2	8±2	3.44	361	3.26	381
ZnO-3	11±1	3.37	368	3.25	382
ZnO-4	14±3	3.35	371	3.24	382

*The wavelength corresponding to the band gap energies were obtained just by energy unit conversion to enhance the comparison with experimental spectra.

Table 4.5 Table showing the experimental values for comparison with Brus equation prediction.

Sample	Avg. particle size (nm)	Experimental values				
		UV-Vis λ_{max} * (nm)		E_g (Tauc plot) (eV)	UV-Vis λ_{edge} ** (nm)	PL emission λ_{max} * (nm)
		M	1'			
ZnO-1	4±3	332	330	3.38	367	370
ZnO-2	8±2	350	345	3.34	371	375
ZnO-3	11±1	353	346	3.33	372	378
ZnO-4	14±3	354	350	3.32	373	380

* M - manual reading and 1' - first derivative method of λ_{max} reading.

** The wavelength was calculated from E_g , as estimated from the Tauc plot.

4.2.4 Fluorescence spectroscopy of ZnO/ME nanocomposite samples

Fig. 4.18 depicts the PL emission of ZnO/ME observed at room temperature. They were collected using excitation wavelength 515 nm, which is suitable for the used MEH-PPV matrix. No luminescence attributable to ZnO was experienced when tested by excitations in UV.

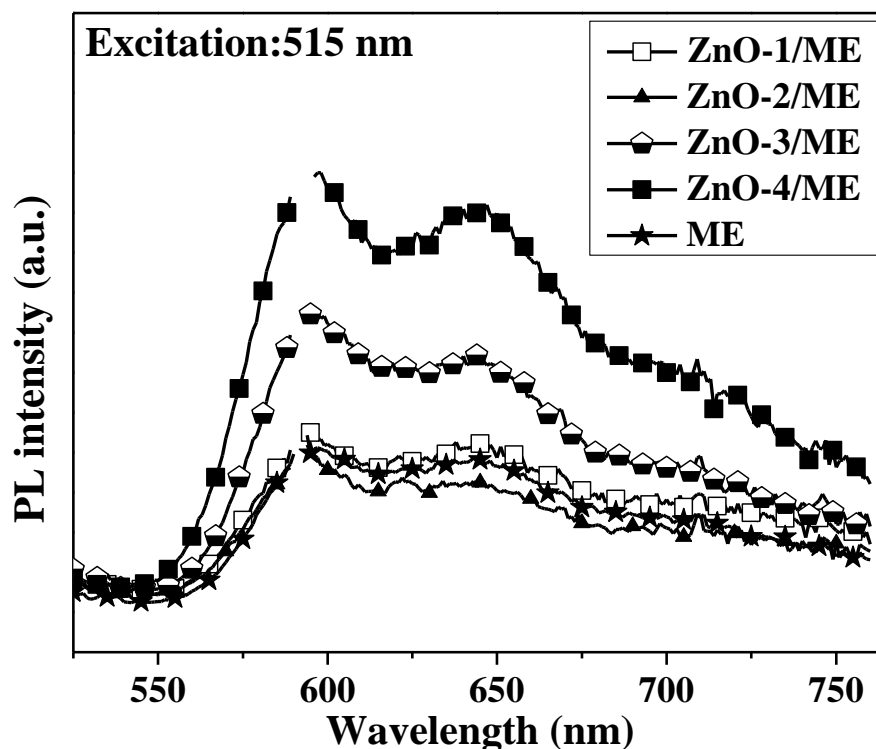


Fig. 4.18 Room temperature PL of ZnO/MEH-PPV nanocomposites and MEH-PPV [141].

Unlike the emission spectra of ZnO nanoparticles, the absolute PL intensity of ZnO/ME is quite challenging to compare, since solid samples were examined. It is observed that the addition of the nanoparticles does not deteriorate the polymer luminescence. The two emission bands 0-0 and 0-1 at emission wavelengths ca 597 nm and ca 645 nm, respectively, are of specific interest. The addition of the nanoparticles resulted in a slight increase in the emission intensity ratio (I_{0-0}/I_{0-1}). It indicates changes in the ordering of the polymer chains and enhancement of intermolecular interactions with respect to the intramolecular interaction. The incorporation of the nanofillers either supports the formation of H-aggregates or disturbs the formation of J-aggregates [149–152].

4.3 Fe-doped ZnO nanoparticles

To modify optical properties, band gap width, and electrical properties of ZnO, the semiconductor nanoparticle was doped with iron. Sample names for Fe-doped ZnO are Fe-1 Z, Fe-5 Z and Fe-10 Z for 1%, 5% and 10% Fe doping respectively. Z is the reference undoped ZnO sample prepared under the same conditions. In this section, the one-pot synthesis of Fe-doped ZnO in a microwave reactor was used as discussed in section 3.3.1. The structural and optical properties of the products and devices were studied by a variety of methods such as UV-Vis absorption spectrometry, powder XRD, SEM and TEM microscopy, thermogravimetric analysis (TGA), PL spectroscopy, and DLS size distribution measurements.

4.3.1 XRD diffractogram of ZnO and Fe-doped ZnO powdered samples

The XRD diffractogram of ZnO and Fe-doped ZnO powdered samples is depicted in Fig. 4.19. The XRD peaks revealed that the synthesised powders are hexagonal wurtzite structure which is in agreement with standard JCPDS file for ZnO (JCPDS 36-1451). No other crystallite phase contaminations by various iron oxides or hydroxides were found. The powdered Fe-ZnO samples were calcined at 400 °C and then reinvestigated by the XRD, the diffractogram is not shown as no other phases were manifested. Thus, the presence of Fe in a separate amorphous phase is excluded as well. The full-width half maxima (FWHM) of the most intense peak, (101), was chosen to calculate the average crystallite size of the samples. The average crystallite size calculated from Scherrer's formula (Equation 3.2) was about 9 to 12 nm, Table 3.1. It is also clear from the diffractograms that the intensity of the peaks is not changing much with increasing doping level. Moreover, the overall appearance and sharpness of the peaks indicate similar crystallinity of all the as-synthesised doped ZnO nanoparticle samples. The crystallite size analysed from XRD spectra may differ from particle size from TEM micrograph [140]. On the other hand, such difference is not expected on the base of experience with the previous sample series (sections 4.1 and 4.2).

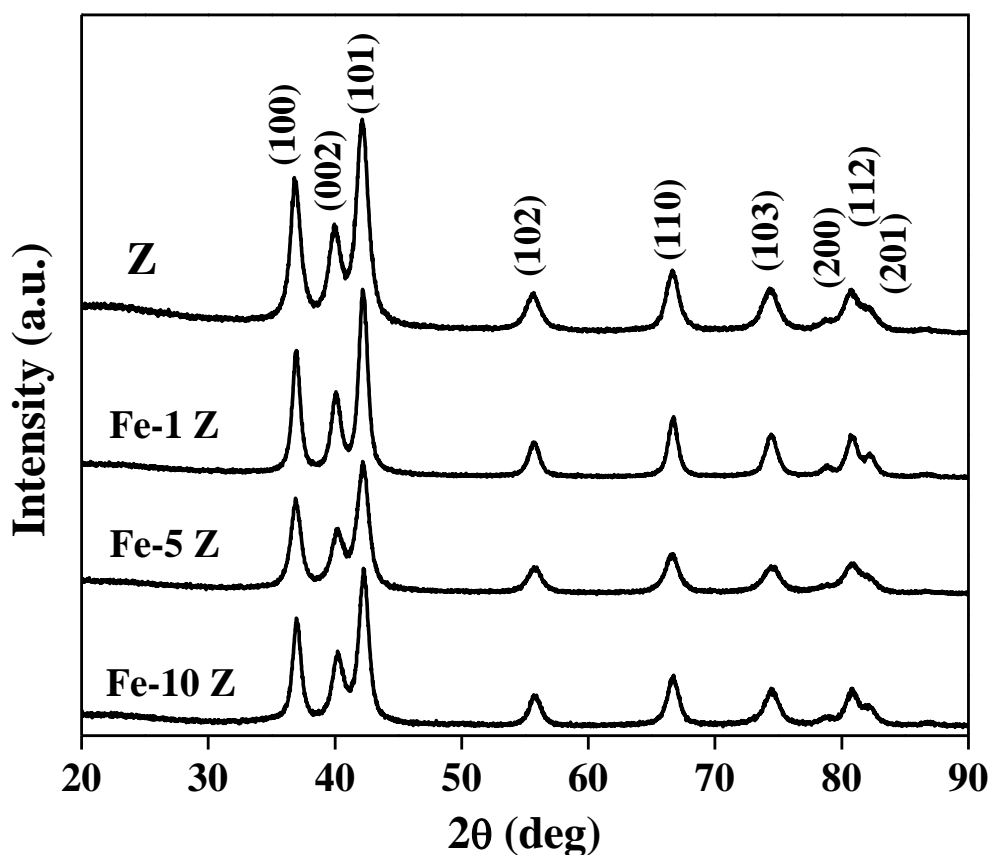


Fig. 4.19 XRD diffractogram of ZnO and Fe-ZnO nanoparticles [131].

4.3.2 TEM micrograph of ZnO and Fe-doped ZnO nanoparticles

The average particle size, morphology and distribution of the synthesised ZnO and $\text{Fe}_x\text{Zn}_{1-x}\text{O}$ colloidal samples is illustrated in Fig. 4.20. From the TEM micrograph, it was evaluated that the average particle size is about 14 nm, 11 nm and 13 nm from Fe-1 Z, Fe-5 Z and Fe-10 Z respectively. The oleic acid surface stabilising layer is not directly observed. The estimations of the average particle size of the prepared samples made by TEM and XRD do not differ significantly taking expected errors into account. A full comparison of average particles size estimation by TEM, XRD and DLS methods is presented in Table 4.7. Likewise, fine dispersions of Fe-ZnO nanoparticles in toluene is an indication of stable colloids which is required for nanocomposite thin film preparation.

It should also be noted that, in the case of sample $\text{Fe}_{0.1}\text{Zn}_{0.9}\text{O}$, fractions of small nanoparticles were observed. These nanoparticles could be presented as a result of the incomplete process of the particle growth stage.

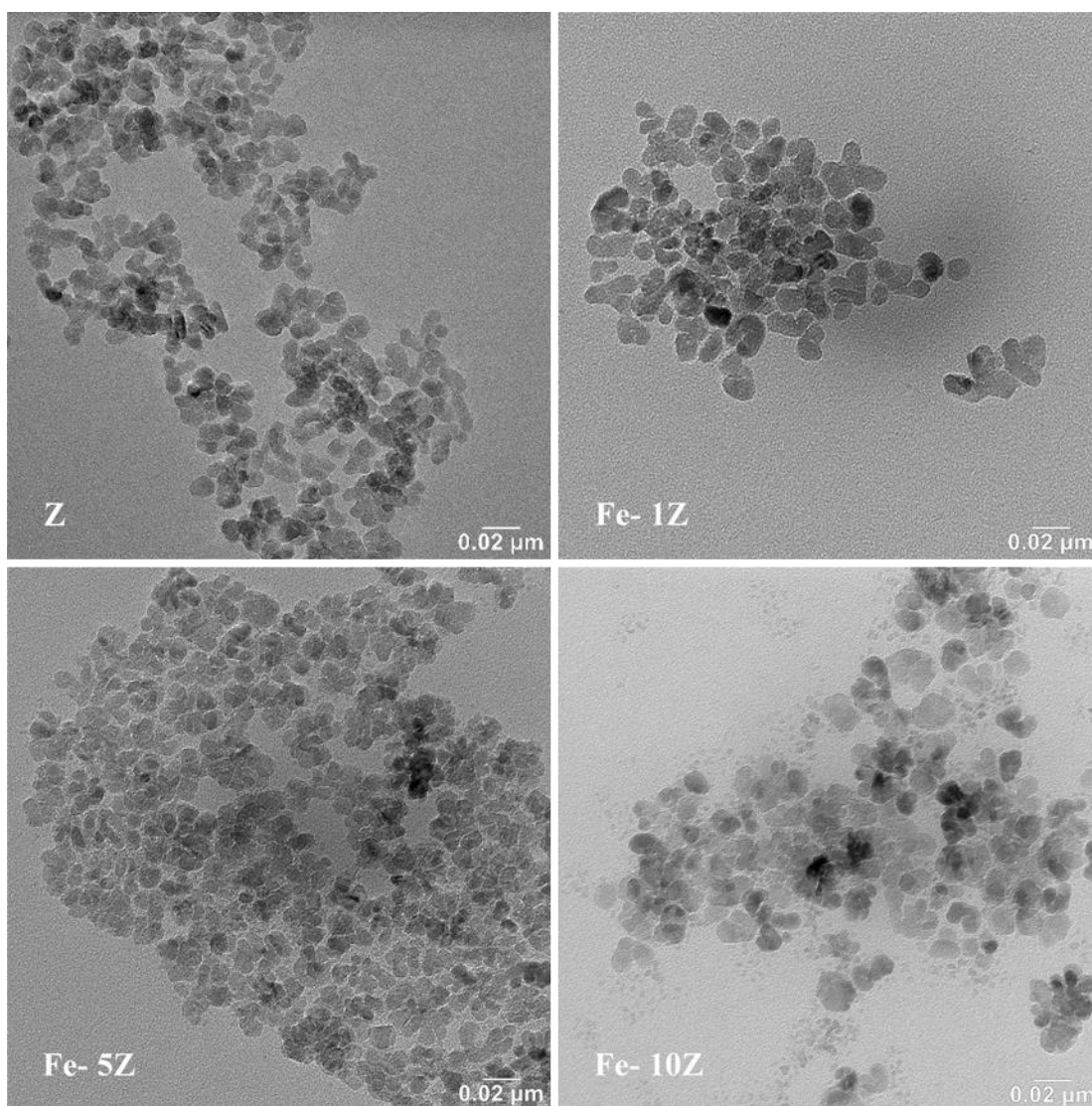


Fig. 4.20 TEM micrograph of Fe-ZnO samples [131].

4.3.3 TGA and DSC analysis of Fe_{0.10}Zn_{1-0.10}O nanoparticle

The thermal decomposition of Fe-10 Z is determined by simultaneous TGA/DSC, see Fig. 4.21. The TGA analysis imparts information related to the stability of Fe-ZnO nanoparticles and oleic acid. Heating of the powdered samples was carried out in an air atmosphere (60 ml min⁻¹) up to 1000 °C at a heating rate of 10 °C min⁻¹. A single step thermoanalytical curve was recorded for TGA while two peaks were distinguished in the DSC graph. A high rate of mass loss was observed between 200 °C to 400 °C (loss of ca 20%). The mass loss step is accompanied by a pronounced exothermic effect observed in the DSC curve. This is due to the desorption, oxidation and decomposition of the oleic acid surfactant or eventual organic byproducts or solvent residuals present on the particle surface. The presence of the second smaller exothermic peak in the DSC indicates the presence of another minor component besides the oleic acid.

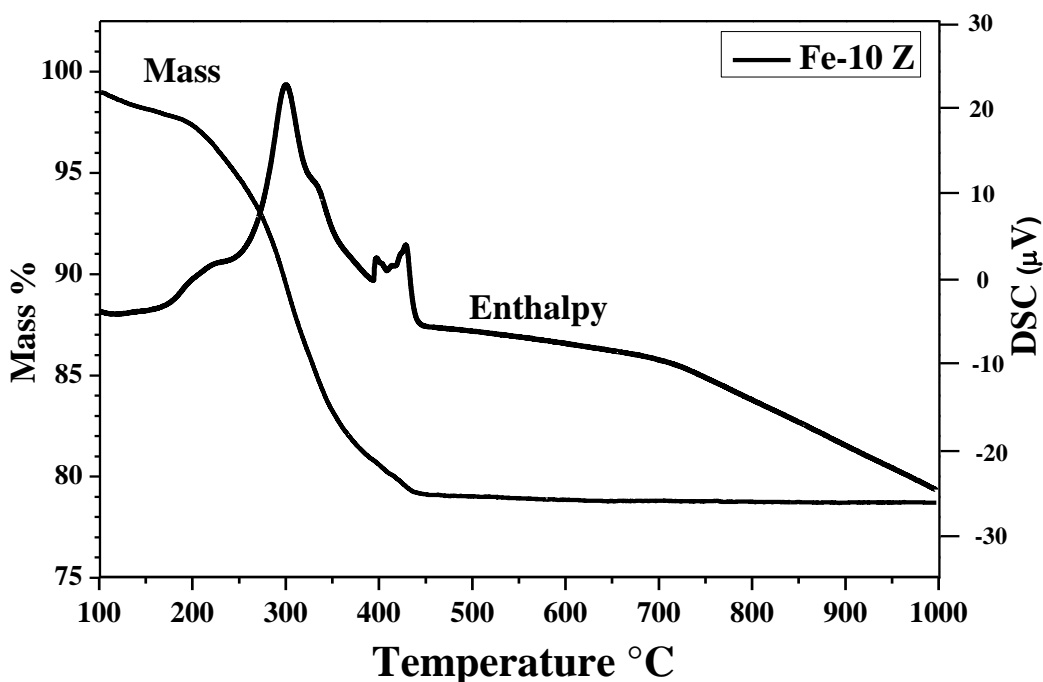


Fig. 4.21 TGA/DSC graph of Fe-10 Z [131].

4.3.4 FT-IR spectra of ZnO and $\text{Fe}_x\text{Zn}_{1-x}\text{O}$ nanoparticles

The FT-IR spectra of Fe-ZnO powdered nanoparticles is shown in Fig. 4.22. A strong vibrational stretching around 600 cm^{-1} is attributed to undoped and Fe-ZnO nanoparticles [138]. The stretching vibration of the hydroxyl group (-OH) due to the dihydrate of ZnO precursor or residual solvent traces is observed as a weak intensity at 3375 cm^{-1} [139]. Likewise, the vibrations due to the methylene group (-CH₂-) from the hydrocarbon moiety is seen at 2920 cm^{-1} and 2853 cm^{-1} . In addition, the intense peaks at 1557 cm^{-1} and 1420 cm^{-1} are associated with vibrational stretching of the carboxylate group [139]. The characteristic peaks implied that the OA bound to the surface of doped ZnO nanoparticles.

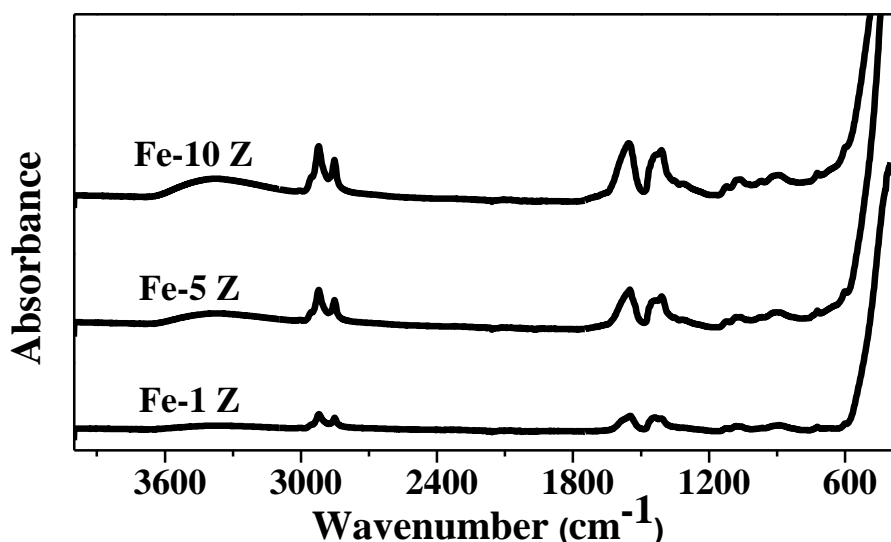


Fig. 4.22 FT-IR of Fe-ZnO powdered samples [131].

4.3.5 Elemental analysis of Fe_xZn_{1-x}O powdered samples

The elemental analysis of the composition of as prepared Fe-doped ZnO was investigated by electron dispersive spectroscopy technique (EDS) integrated to the SEM microscope. In the interpretation of the spectral technique, the compositional existence of Zn and O atoms, and the presence of Fe dopant at varying degrees of dopant concentration is actualised. Most importantly, no other elemental peaks were observed, confirming the absence of other elements and the purity of the samples. The atomic percentage of the elements Fe and Zn were quantitatively analysed by the spectroscopic analytical instrument integrated in SEM. The powdered Fe-doped ZnO samples were calcined at 400 °C prior to the analysis. The obtained concentrations of these atoms were compared with the elemental composition calculated from initial precursor concentrations and studied, as presented in Table 4.2. It can be deduced that the composition of the prepared doped nanoparticles complies with the initial precursor load. A conclusion can be drawn that the EDS and XRD data confirm the presence of Fe (yet without specification of its oxidation state) ions in the ZnO host crystal lattice.

Table 4.6 Contents of Zn and Fe according to the synthesis protocol and concentration of Fe in the product as calculated from precursor content and as measured by EDS [131].

Sample	n_{Zn} (mmol)	n_{Fe} (mmol)	n_{Fe}/(n_{Fe}+n_{Zn}) (atomic %)	Fe conc. (EDS) (atomic %)
Fe-1 Z	3.56	0.04	1.10	1.90
Fe-5 Z	3.42	0.18	5.19	4.51
Fe-10 Z	3.24	0.36	10.19	9.40
Z	3.60	--	--	--

4.3.6 DLS of colloidal Fe-doped ZnO dispersion

The colloidal stability of the Fe-ZnO dispersed in toluene is analysed by dynamic light scattering technique (DLS), Fig. 4.23, Fig. 4.24, and Fig. 4.25. The statistical representation of the hydrodynamic diameter is retrieved from DLS measurement. In the colloidal samples, the Fe-ZnO nanoparticles are dispersed in non-polar solvent toluene due to a layer of oleic acid on the surface of the nanoparticles. Moreover, the small nanoparticles tend to agglomerate, resulting in larger hydrodynamic diameter of the samples as compared to TEM average particle size Table 4.7. The solvation of the ZnO nanoparticle core along with the capping agent layers resulted in increased diameter (hydrodynamic diameter) of the capped-ZnO nanoparticles. Likewise, it can be concluded from the PdI values that the prepared nanodispersions are monodispersed systems despite the slightly

visible agglomeration (Fig. 4.20). Nonetheless, contrary to the TEM micrograph of Fe-10 Z, the smaller fractions of particles were not detected from the DLS technique. These technical glitches could be due to the detection limit of the instrument.

Table 4.7 Zeta average and polydispersity index, average crystallite and particle size of ZnO and Fe_xZn_{1-x}O nanoparticle dispersions [131].

Sample	Z- Average diameter (nm)	Peak maxima (nm)	PdI	XRD average crystallite size (nm)	TEM average particle size (nm)
Fe-1 Z	39	45±17	0.13	12	14±3
Fe-5 Z	39	46±15	0.11	9	11±2
Fe-10 Z	42	44±16	0.09	11	13±3

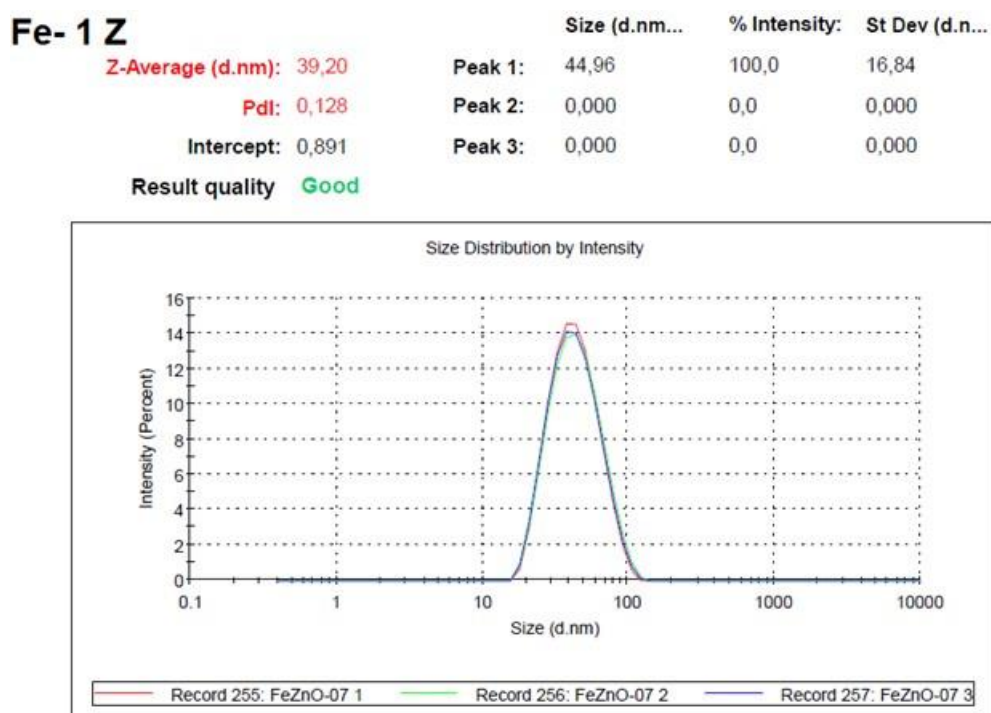


Fig. 4.23 DLS size distribution by the intensity of Fe-1 Z nanoparticles dispersed in toluene. (graphical output as obtained from the dedicated original data processing software) [131].

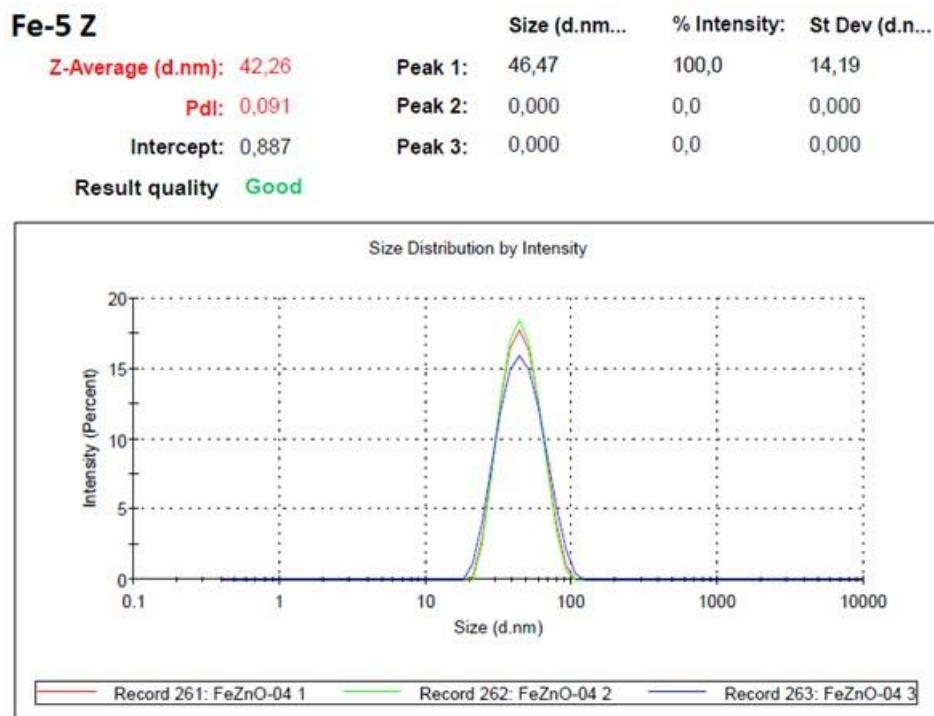


Fig. 4.24 DLS size distribution by the intensity of Fe-5 Z nanoparticles dispersed in toluene. (graphical output as obtained from the dedicated original data processing software) [131].

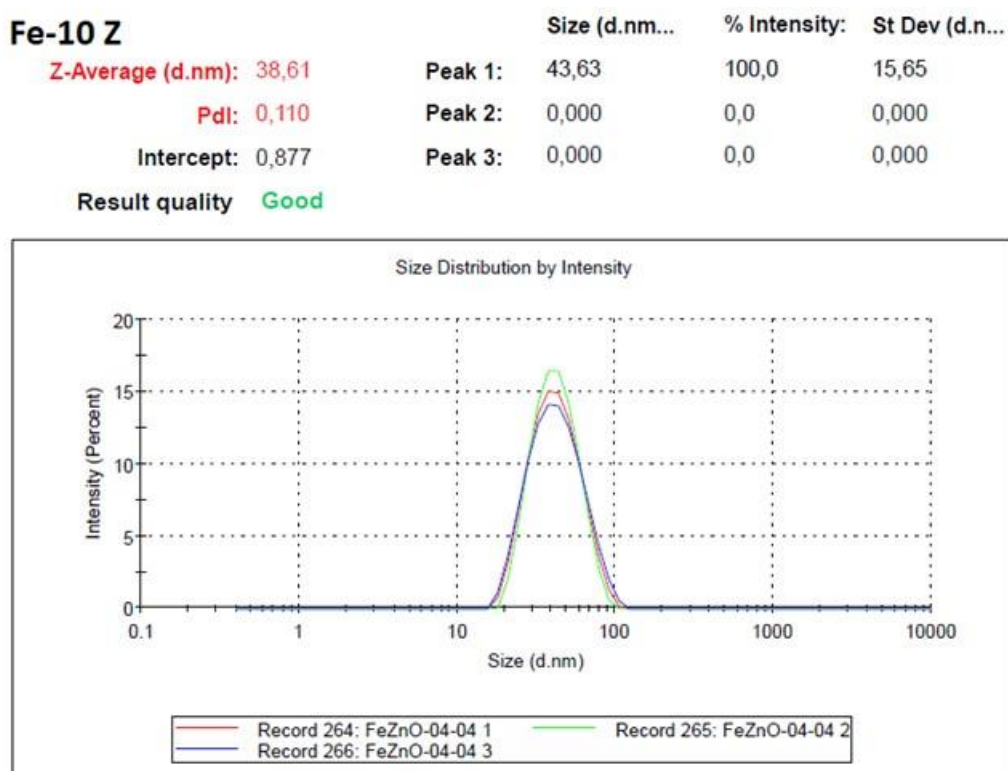


Fig. 4.25 DLS size distribution by the intensity of Fe-10 Z nanoparticles dispersed in toluene. (graphical output as obtained from the dedicated original data processing software) [131].

4.3.7 UV-Vis and Tauc plot of ZnO and Fe-ZnO colloidal dispersions

The absorption spectra of ZnO and $\text{Fe}_x\text{Zn}_{1-x}\text{O}$ colloidal dispersions is illustrated in Fig. 4.26. It can be seen that the absorption edge for undoped ZnO is relatively sharp, and the peak has a readable maximum at 350 nm, while there was a red-shift of the edge for doped ZnO nanoparticles. Moreover, the edge losses its steepness. It becomes to be less defined and tailing to the visible range with increasing doping. The tail region (up to 500 nm) corresponds to the creation of states in the bandgap. Since the average particle size of the nanoparticle did not change significantly, the shift to longer wavelength is primarily due to the addition of Fe [66, 153].

Further analysis of the absorption band edge of ZnO and Fe-ZnO powdered samples was conducted using diffuse-reflectance ultraviolet-visible spectroscopy (DRUV-Vis), Fig. 4.27. Tauc plot calculation from the absorption region of the diffuse reflectance led to the determination of bandgap of the samples. The above-described change in absorption spectra with increasing dopant concentration is visible from the Tauc plot more clearly.

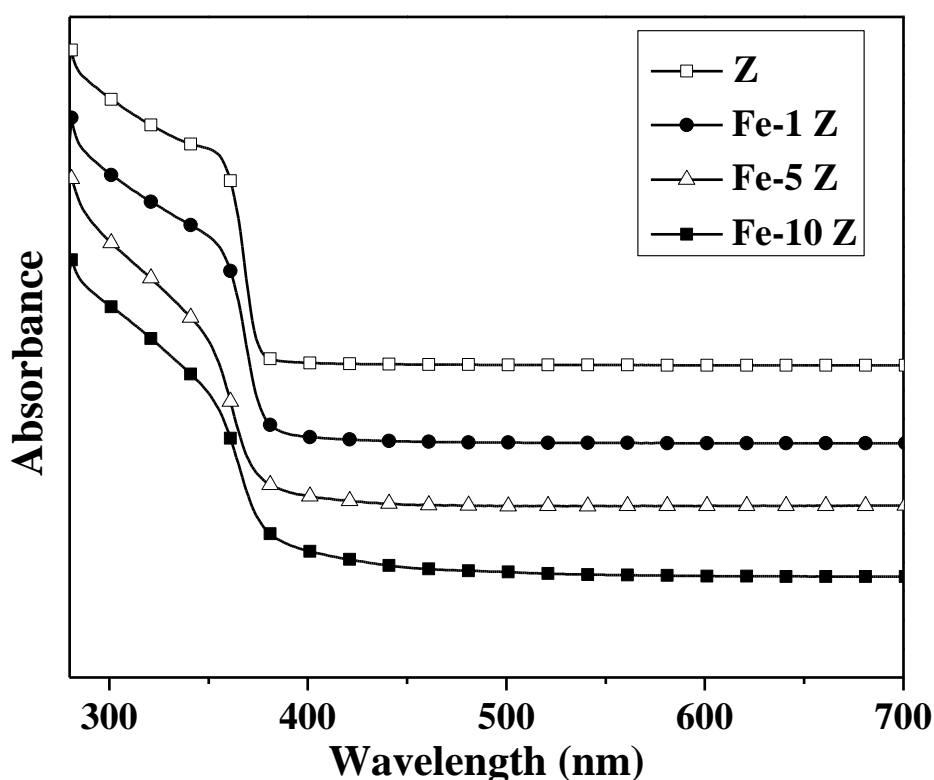


Fig. 4.26 UV-Vis spectra of pure and F-ZnO colloids [131].

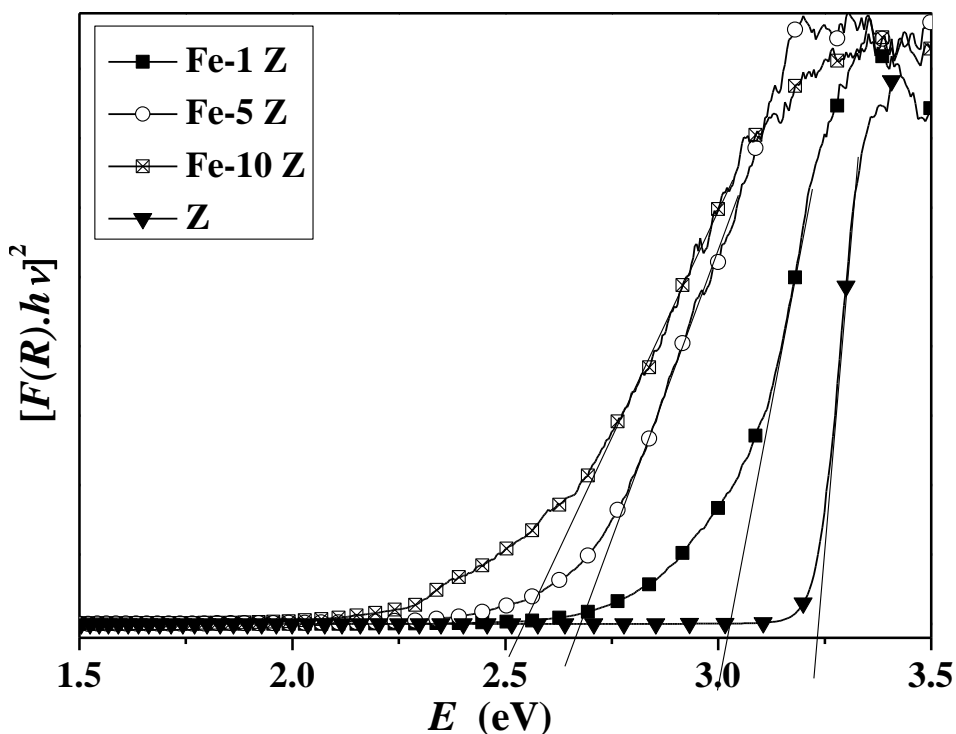


Fig. 4.27 Tauc plot and DRUV-Vis of ZnO and Fe-ZnO powders [131].

It can be seen from the calculated values of the band gaps that undoped ZnO nanoparticle's band gap is 3.2 eV. With further increase in Fe dopant concentration, the band gaps of the doped samples narrowed as seen in Table 4.8, which is in agreement with Fe-doping effect observed for nanopowders synthesised by sol-gel and calcining method [154].

Table 4.8 Correlation between average particle size and band gap of ZnO and Fe-ZnO [131].

Sample name	Avg. Particle size (nm)	Band gap (eV)
Z	9±2	3.2
Fe-1Z	14±3	3.0
Fe-5Z	11±2	2.7
Fe-10Z	13±3	2.5

4.3.8 Emission spectra of ZnO and Fe_xZn_{1-x}O colloids

The photoluminescence (PL) spectra for diluted Fe_xZn_{1-x}O nanoparticle dispersions at an excitation wavelength of 322 nm at room temperature are shown in Fig. 4.28. From the absorption spectra of the samples, the excitation wavelength of the samples was estimated. It can be observed from the graph that

the emission peak is manifested in 370 nm to 400 nm. According to [155], it is possible that the PL emission intensity decreases in UV region and increases relatively in the violet region. Surprisingly, in this work, the emission maximum wavelength decreases for 5 and 10 % of doping. Comparing to [155], a much higher level of doping was achieved in this study, as evidenced by the significant band gap narrowing. The peaks in the UV region are due to near band-edge (NBE) transitions. The direct band gap transition of the excited electrons from the conduction band to the valence band may compete with transitions involving various defects (intrinsic like zinc interstitials and extrinsic caused by the introduction of the dopant) resulting into the observed complicated pattern of red and blue shifts. For sample $\text{Fe}_{0.01}\text{Zn}_{0.99}\text{O}$, a slight shift to higher wavelength indicates the relaxation process related to NBE states as no red-shift was seen in the UV-Vis spectrum. Further, the blue-shift for higher dopant concentration correlates with the same feature in the absorption spectra. Moreover, with increasing doping concentration, the PL intensity correspondingly reduced. The lowering of the intensity is due to the presence of Fe ions that provides an alternative pathway for the relaxation of excited electrons.

Since no peaks were observed in the visible region for undoped and Fe-doped ZnO, all transitions related to the corresponding states in the band gap are non-radiative. Besides, the surface functionalisation of the nanoparticle surface by oleic acid led to the absence of luminescence corresponding to surface defects [138].

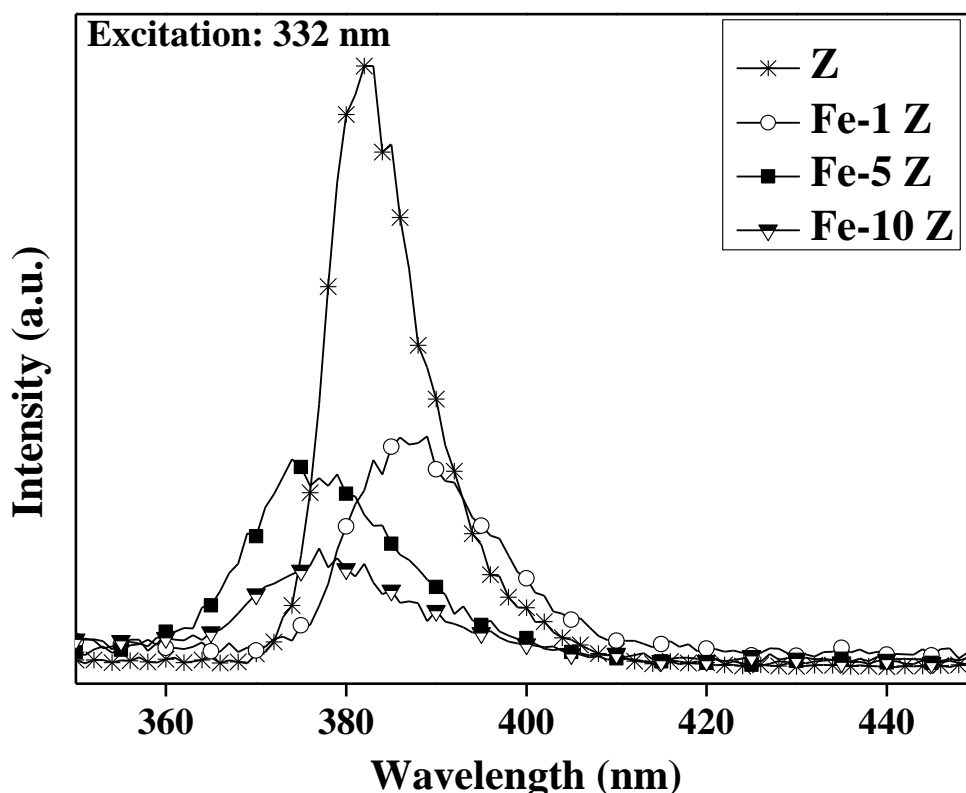


Fig. 4.28 Fluorescence spectra of ZnO and Fe-doped ZnO colloids [131].

4.3.9 Investigation of oxidation states of Fe in $\text{Fe}_x\text{Zn}_{1-x}\text{O}$ samples

The surface analysis method renders information related to the composition and oxidation state of Fe in Fe-doped ZnO nanoparticles characterised by XPS, Fig. 4.29, and Fig. 4.30. In this investigation, the peak positions of the main peaks and the satellite of Fe gives the information of its ionic state. The satellite peaks position for Fe $2p_{1/2}$ and Fe $2p_{3/2}$ is sensitive to the oxidation states and this information is used for qualitative determination of the ionic state of iron. The core peak positions of Fe $2p_{1/2}$ and Fe $2p_{3/2}$ are 709.8 and 723.5 eV, 710.1 and 723.9 eV for 1 and 5 % respectively. The satellite peak was recorded at 716.3 and 729.8 for 1 % and 717.6 and 731.9 eV for 5 %. Besides, the binding energy difference of Fe $2p_{1/2}$ and Fe $2p_{3/2}$ is around 13 eV. These peaks were deconvoluted into two peaks to distinguish the oxidation state of Fe^{2+} and Fe^{3+} , Table 4.9. The values were in coherence with the work published by Karamat *et al.* [156]. Concerning quantification, Fe^{2+} was identified as the prevailing form in the sample. Besides that, the presence of Fe^{3+} is manifested in the spectrum. However, precise quantification is not possible with respect to the relatively poor resolution.

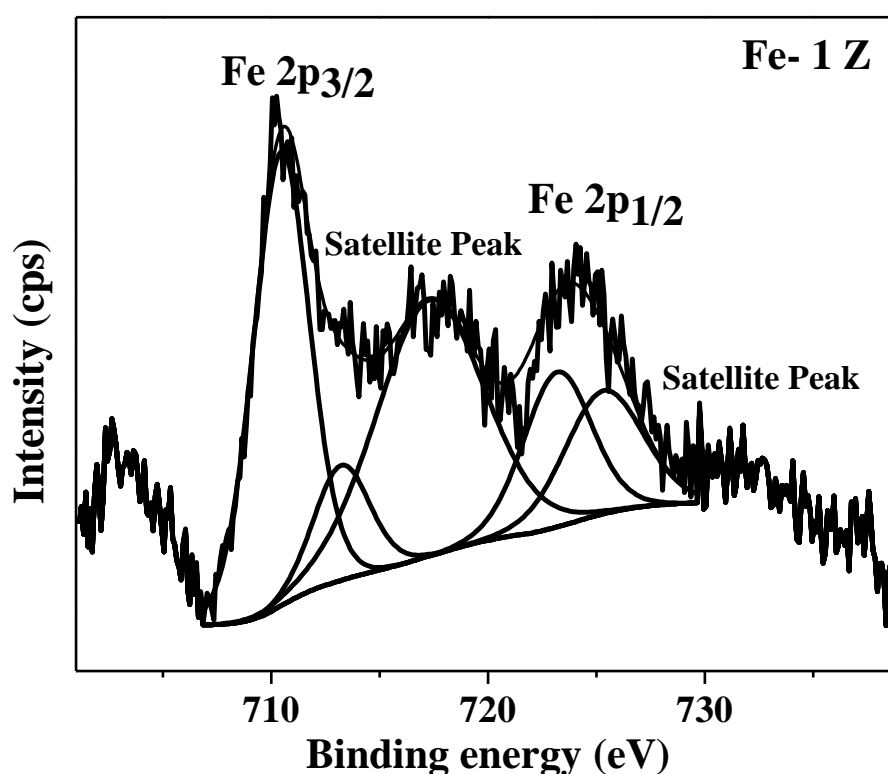


Fig. 4.29 Narrow scan XPS core spectra of Fe 2p of the $\text{Fe}_x\text{Zn}_{1-x}\text{O}$, sample $x=0.0$ [131].

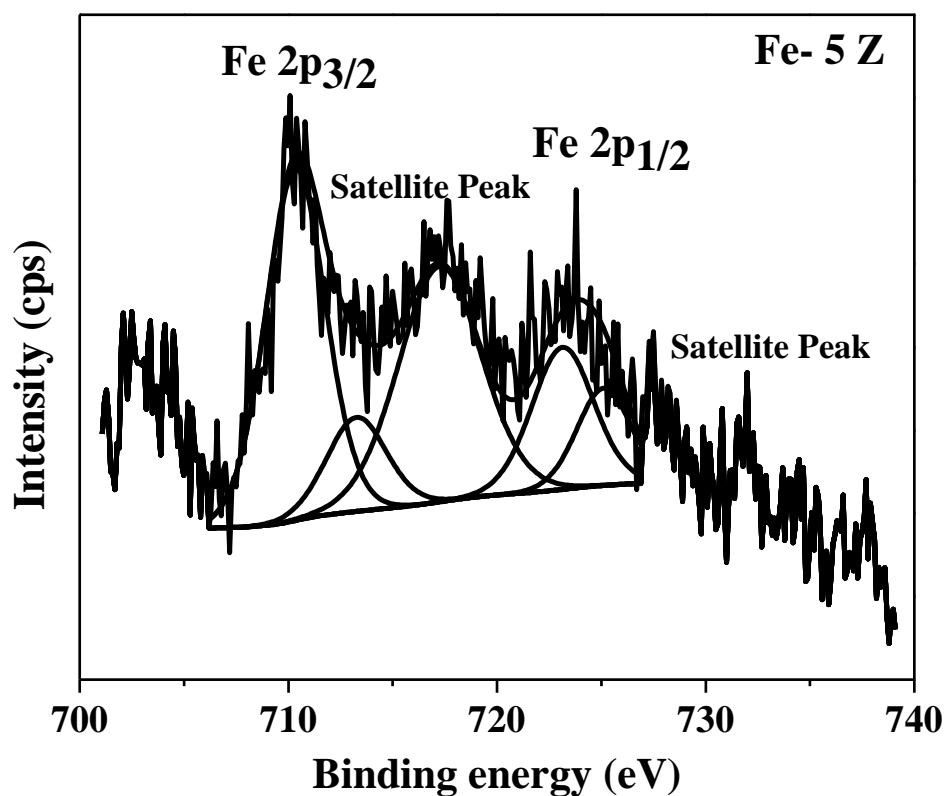


Fig. 4.30 Narrow scan XPS core spectra of Fe 2p of the $Fe_xZn_{1-x}O$, sample, $x= 0.05$ [131].

Table 4.9 De-convoluted Fe^{2+}/Fe^{3+} peak positions at the binding energy (BE) scale [131].

Sample	Fe doping (mol %)	Main peaks BE (eV)				Satellite peaks BE (eV)	
		Fe^{2+}		Fe^{3+}		Fe^{3+}	
		Fe 2p _{3/2}	Fe 2p _{1/2}	Fe 2p _{3/2}	Fe 2p _{1/2}	Fe 2p _{3/2}	Fe 2p _{1/2}
Fe-1 Z	1	710.6	723.2	713.2	725.4	717.5	729.8
Fe-5 Z	5	710.4	723.1	713.4	725.4	717.6	731.3

In the same study, the presence of Zn in the doped ZnO was also validated, Fig. 4.31. The location of the binding energies of Zn 2p_{3/2} affirms the existence of Zn atom. Therefore, the binding energies for 1 %, 5 % and 10 % Fe doped ZnO the binding energies of Zn 2p_{3/2} are found to be at 1021.2 eV, 1021.1 eV and 1021.2 eV, respectively. In addition to that, the differences in binding energies is within the experimental error range.

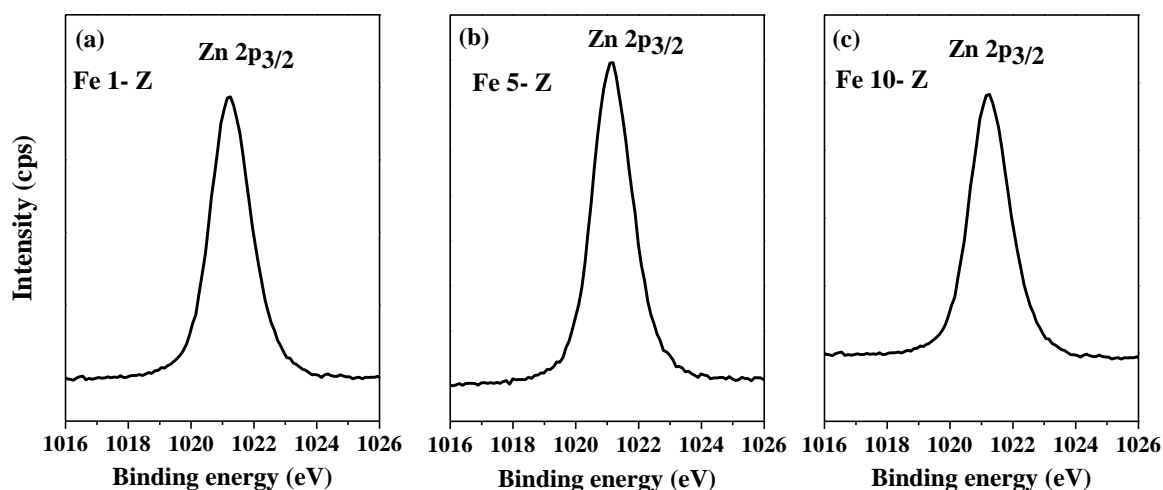


Fig. 4.31 Narrow scan XPS core spectra of Zn $2p_{3/2}$ of the $Fe_xZn_{1-x}O$ samples (a) $x = 0.01$, (b) $x = 0.05$ and (c) $x = 0.1$ [131].

4.3.10 Fluorescence spectroscopy of Fe- ZME nanocomposite samples

The emission spectra of the casted Fe- ZME nanocomposite on a glass substrate was characterised at room temperature, Fig. 4.32. The spin-coated thin films were excited at 515 nm. The nanocomposite thin films showed emission ranging from 560 nm to 800 nm. This emission is primarily from the MEH-PPV polymer. Two distinct peaks are noticeable from the spectral graph, one at around 595 nm and the shoulder peak around 645 nm. This is well documented in the literature that 595 nm peaks are due to 0-0, and shoulder peak is 0-1 vibronic transitions resulting from excitonic recombination [149–151]. The ratio of intensities of the two peaks changed between pure polymer thin film and nanocomposite films in favour of the 0-1 vibronic transition. On top of that, the ratio is not dependent on the doping level, as no shift of peak maxima was observed. Moreover, the fillers influenced the ordering of polymer chains in the nanocomposite during casting by spin-coating. This also affected the J-H aggregate formation [152].

Not only that, the long-chain organic ligand on the surface of the nanoparticles also does not prevent charge separation and transfer processes at the interface [157]. It can also be argued that the lowering of the PL intensity in the conductive layer is a result of electron transfer from LUMO of MEH-PPV to the conduction band of ZnO nanoparticles [158]. The outcome is most apparent for undoped ZnO and less for Fe-doped ZnO. For MEH-PPV, the LUMO is -3.0 eV, and HOMO is -5.3 eV whereas, for ZnO, the conduction band is -4.2 eV and valence band -7.6 eV. The readjustment in the energy level of MEH-PPV and ZnO nanoparticles during charge transfer could also lead to the different relaxation pathway of excited electrons. The photo-excited electrons withdraw themselves off during the charge transfer process at the MEH-PPV and $Fe_xZn_{1-x}O$ energy level interface [149].

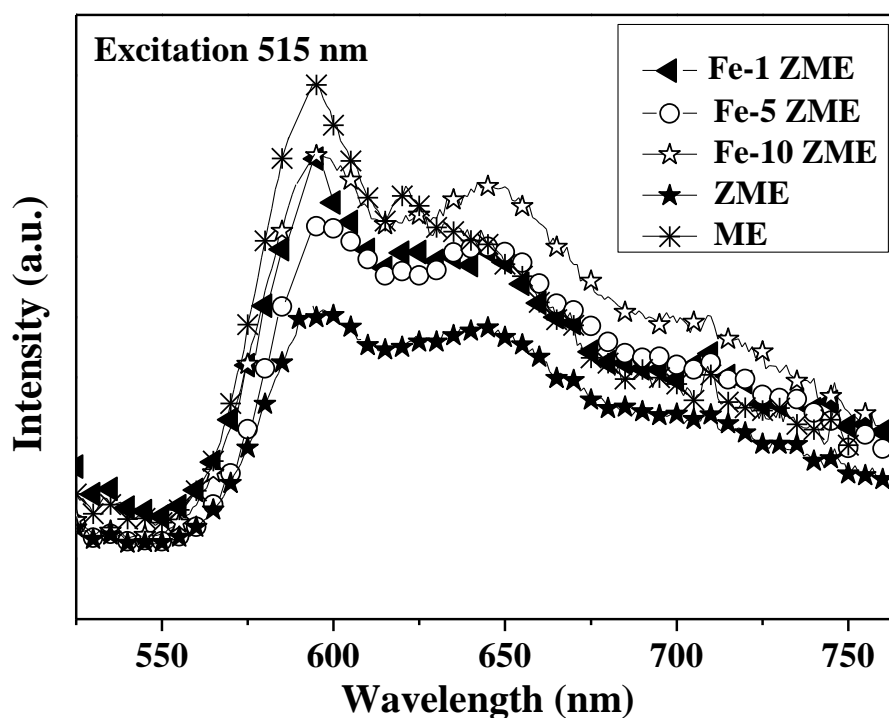


Fig. 4.32 Room temperature PL spectra of pure MEH-PPV, ZnO/MEHPPV and $Fe_xZn_{1-x}O/MEH-PPV$ nanocomposites [131].

4.4 Al-doped ZnO nanoparticles

To modify optical properties, band gap width, and electrical properties of ZnO, n-doping by aluminium was investigated as the second choice of dopant. The synthesis of Al-ZnO was explored by varying the Al doping concentration. As in Fe-doped ZnO nanoparticles, the same atomic doping concentration was utilised. Sample names for Al-doped ZnO are Al-1 Z, Al-5 Z and Al-10 Z are for 1%, 5% and 10% Al doping, respectively. Z is the reference undoped ZnO sample prepared under the same conditions but without any doping (as in section 4.3). The structural and optical properties of the products and thin films were studied by the same methods (but XPS) as in case of Fe-doped materials in section 4.3.

4.4.1 XRD diffractogram patterns of ZnO and Al-ZnO powder

The XRD diffractogram of undoped and Al-doped ZnO is depicted in Fig. 4.33. The phase purity, crystallinity and average particle size of the samples were analysed by this technique. The peaks indexed at (100), (002), (101), (102), (110), (103), (200), (112) and (201) corresponds to the hexagonal wurtzite structure of ZnO, and it goes well with standard JCPDS database, JCPDS 36-1451. Absence of secondary phases of oxides of Al corresponds to the presence of Al^{3+} ions in the host dispersed at the atomic level. The negligible variation of diffraction peak angles in comparison with that of pure ZnO suggests that Al^{3+} ions substitute Zn^{2+} in the crystal lattice of the structure of ZnO. However, the peak intensity varies

in accordance with the dopant concentration, confirming the presence of dopant in the semiconductor nanoparticles, i.e. decreases with increased doping level [159]. The ionic radius of Al^{3+} is 0.053 nm and for Zn^{2+} ion 0.073 nm. Thus, Al^{3+} ions could produce some strain in the crystal lattice of ZnO atom and decrease the lattice parameters size [160, 161]. On the other hand, the repulsive Coulomb force due to Al^{3+} surplus of charge can compensate for this effect by the expansion of the lattice parameters [162, 163].

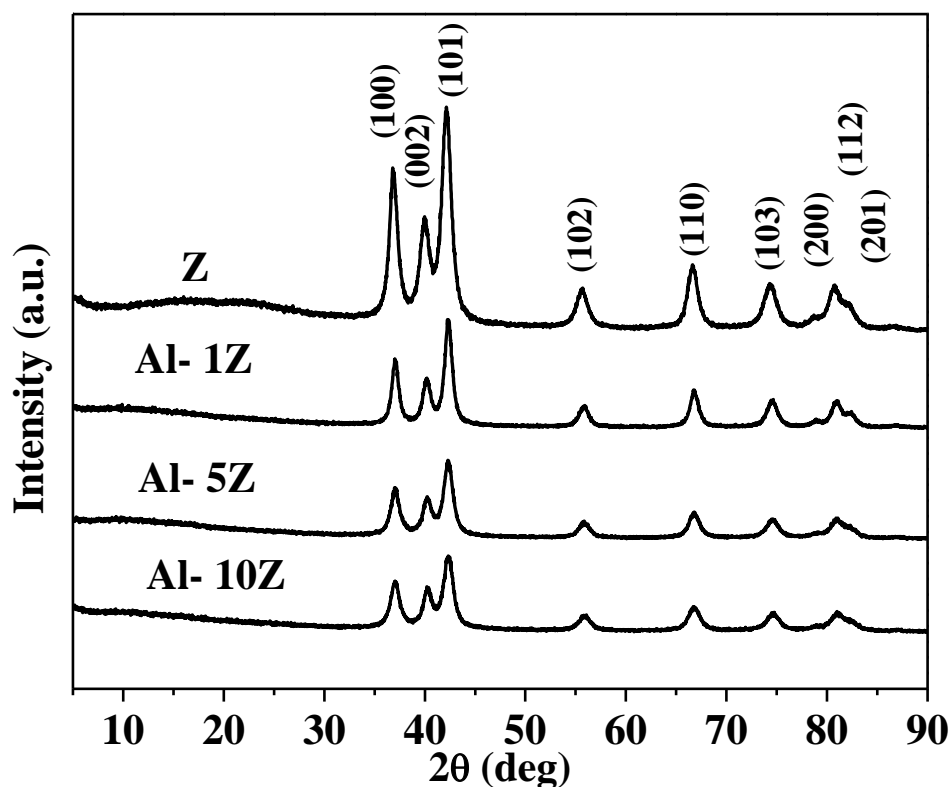


Fig. 4.33 XRD peaks of ZnO and Al-ZnO powders [164].

The average crystallite size of ZnO and Al-ZnO is calculated by Scherrer's equation (Equation 3.2). No preferential direction of particle growth is manifested in the diffractograms. As the peak at (101) lattice plane has high intensity, the average crystallite size of ZnO was calculated from the (101) plane of the lattice. The values were found to be 11.5 nm, 9.5 nm and 8.6 nm for Al- 1Z, Al- 5Z and Al- 10Z, respectively. Thus, the microwave synthesis of the nanoparticles led to single-phase Al-doped ZnO powder with smaller crystallite size.

4.4.2 TEM images of ZnO and $\text{Al}_x\text{Zn}_{1-x}\text{O}$ nanoparticles

The electron micrograph analysis of the pure and Al-ZnO was carried out by transmission electron microscope (TEM), Fig. 4.34. Monodisperse nanoparticles is verified by this high energy electron microscopic technique. In addition, a critical role played by the surfactant, oleic acid, is visible in the images. Apart

from checking the agglomeration of the reactive surface of the nanoparticles, the long alkyl chains enable the stable dispersion in non-polar solvent toluene. The average particle size of the particles is about 10 nm, 9 nm and 8 nm for Al-1Z, Al-5Z and Al-10Z respectively. The average crystallite size calculated from Scherrer's equation correlates with the average particle size from TEM imaging. The TEM investigation also revealed similar morphology for all the samples.

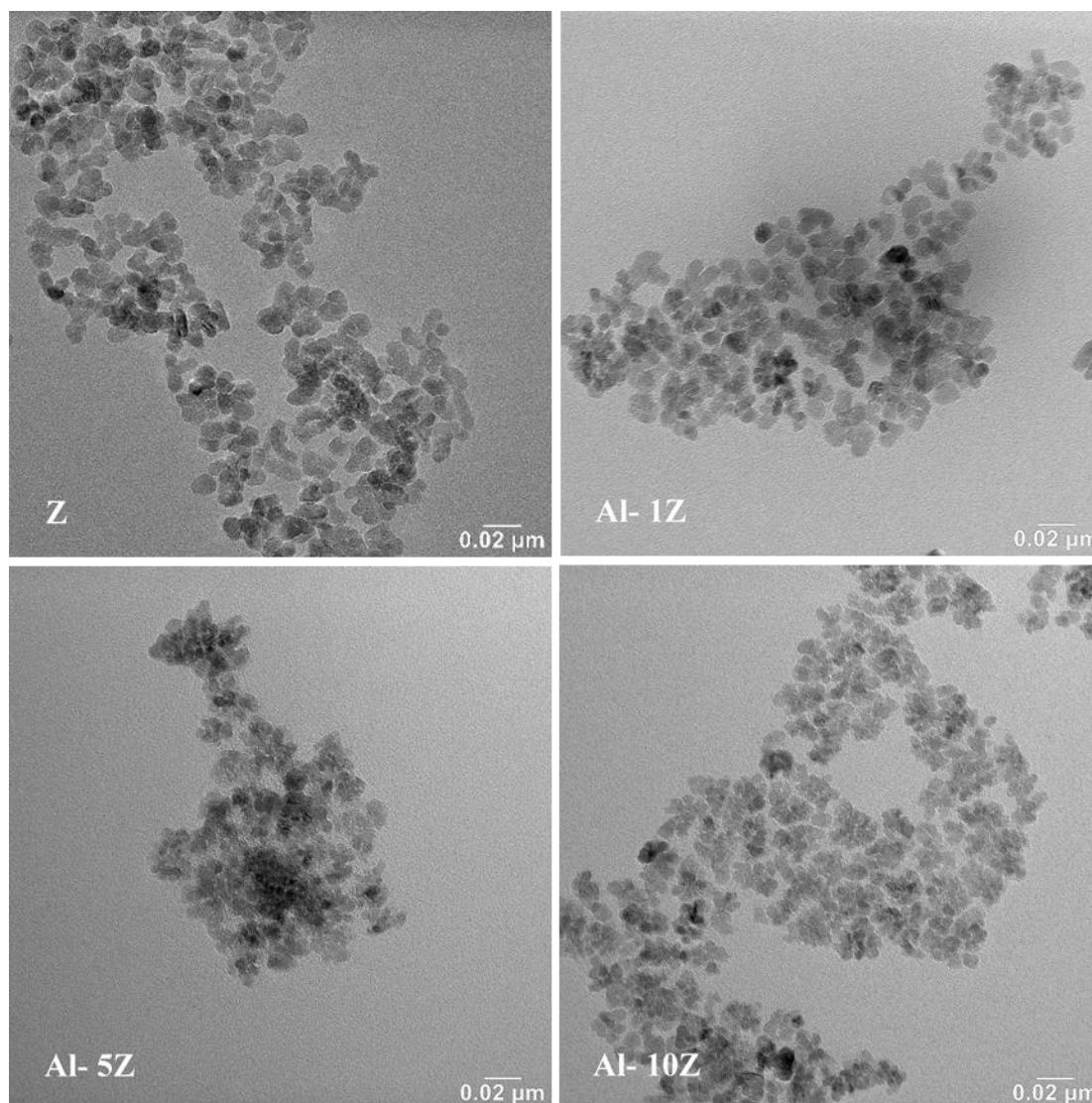


Fig. 4.34 TEM micrograph of undoped ZnO and Al-doped ZnO nanoparticles dispersed in toluene.

4.4.3 Analysis of Al doping concentration by EDS technique

The dopant concentration and composition of aluminium-doped zinc oxide was assessed by energy-dispersive X-ray spectroscopy (EDS). The powdered samples were calcined at 300 °C for two hours. These calcined samples were analysed for the elemental composition as in Fe-doped ZnO. From the EDX spectra, Zn, O and Al peaks are observed for the doped samples. Moreover, the calculated concentrations and the observed values are comparable (Table 4.10).

Table 4.10 Al concentration calculated from amounts of reaction precursors in comparison with Al-dopant concentration as obtained from EDS analysis.

Sample	n_{Zn} (mmol)	n_{Al} (mmol)	n_{Al}/(n_{Al}+n_{Zn}) (atomic %)	Al conc. (EDS) (atomic %)
Al- 1Z	3.58	0.05	1.28	1.60
Al- 5Z	3.43	0.18	4.98	5.23
Al- 10Z	3.28	0.37	10.13	9.39
Z	3.60	--	--	--

4.4.4 Study of colloidal stability and hydrodynamic diameter of Al-ZnO colloids

The hydrodynamic diameter analysed by DLS technique of Al- 1Z, Al- 5Z and Al- 10Z nanoparticles dispersed in toluene is shown in Fig. 4.35, Fig. 4.36, and Fig. 4.37. As with the previous samples, ZnO series and Fe-ZnO series, measured hydrodynamic diameter is greater than the average particle size analysed by TEM imaging technique. This characterisation technique gave information of Al-ZnO nanoparticle, the organic ligand adhered to the surface of the nanoparticle, and the solvation sphere. The hydrodynamic diameter and PDI were not influenced by the doping procedure and is similar to that one obtained for Fe-doped samples and pure ZnO nanoparticles. The dispersion stability and behaviour of the nanoparticles in toluene is fully controlled by the use of OA.

Table 4.11 Hydrodynamic diameter, PDI and average particle size of Al-doped ZnO samples as estimated by XRD and TEM.

Sample	Z-Average diameter (nm)	PdI	Peak Maxima (nm)	XRD average crystallite size (nm)	TEM average particle size (nm)
Al- 1Z	49	0.13	56±22	11	10±2
Al- 5Z	36	0.11	40±15	10	10±2
Al- 10Z	42	0.13	49±19	9	9±1

Results

	Size (d.nm...)	% Intensity:	St Dev (d.n...
Z-Average (d.nm): 48,93	Peak 1: 56,02	100,0	22,00
Pdl: 0,138	Peak 2: 0,000	0,0	0,000
Intercept: 0,890	Peak 3: 0,000	0,0	0,000

Result quality **Good**

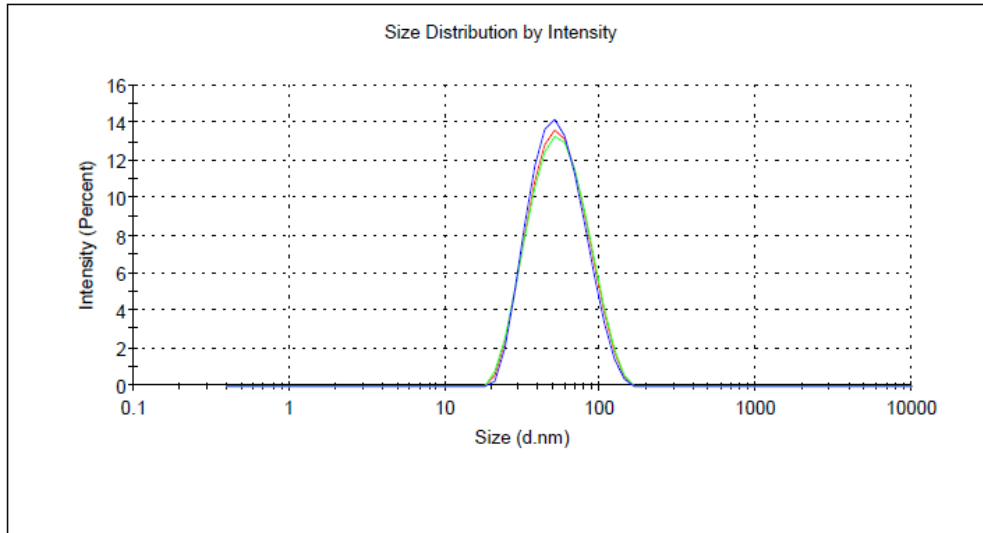


Fig. 4.35 DLS of Al- 1Z colloidal sample (graphical output as obtained from the dedicated original data processing software)

Results

	Size (d.nm...)	% Intensity:	St Dev (d.n...
Z-Average (d.nm): 35,75	Peak 1: 40,33	100,0	14,54
Pdl: 0,108	Peak 2: 0,000	0,0	0,000
Intercept: 0,907	Peak 3: 0,000	0,0	0,000

Result quality **Good**

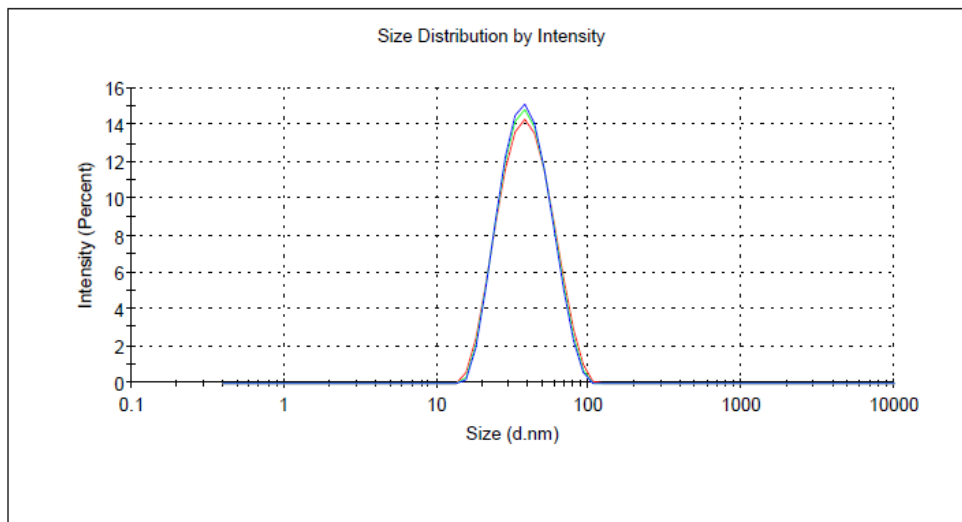


Fig. 4.36 DLS of Al- 5Z colloidal dispersion (graphical output as obtained from the dedicated original data processing software)

Results

	Size (d.nm...)	% Intensity:	St Dev (d.n...
Z-Average (d.nm): 42,16	Peak 1: 48,46	100,0	18,59
Pdl: 0,128	Peak 2: 0,000	0,0	0,000
Intercept: 0,889	Peak 3: 0,000	0,0	0,000

Result quality **Good**

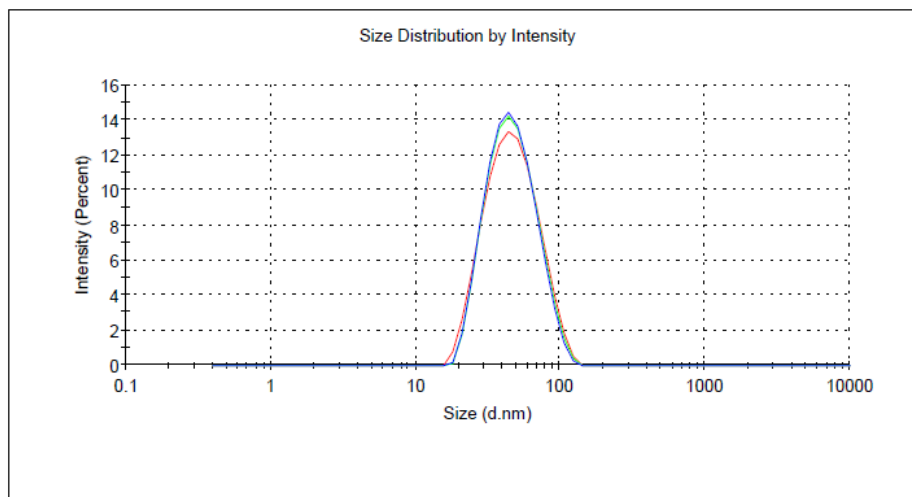


Fig. 4.37 DLS of Al- 10Z colloid (graphical output as obtained from the dedicated original data processing software)

4.4.5 Simultaneous TGA/DSC analysis of $\text{Al}_{0.01}\text{Zn}_{1-0.01}\text{O}$

Like the previously discussed samples, undoped ZnO (Fig. 4.14) and Fe-ZnO (Fig. 4.21), the TGA and DSC curves of Al-doped ZnO show similar characteristics, Fig. 4.38. This, confirms the surface modification of Al-doped ZnO but the second component of the surface adsorbates prevails in this case.

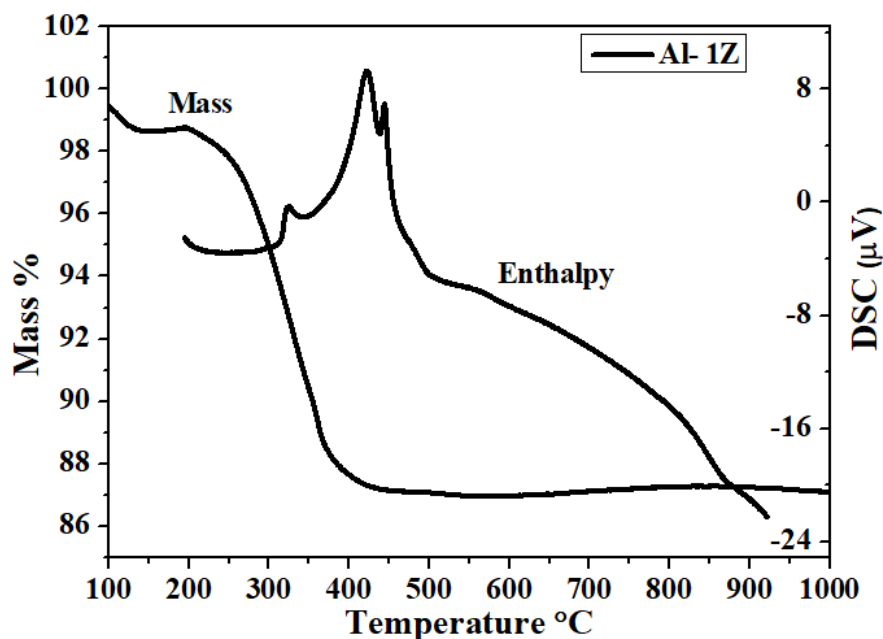


Fig. 4.38 TGA of Al-1Z powdered sample.

4.4.6 FTIR spectra of Al_{0.1}Zn_{1-0.1}O powdered samples

The infrared spectroscopy of OA-capped Al- 10Z in the region 4000 cm⁻¹ to 400 cm⁻¹ is depicted in Fig. 4.39. This spectroscopic technique complements the information obtained from XRD and TEM analysis, Fig. 4.33, and Fig. 4.34. Since this sample has the highest doping percentage among the three, so Al- Z10 alone was indicated in the FT-IR analysis. The weak peaks at about 3400 cm⁻¹ are due to the stretching vibrations of –OH group from oleic acid or dihydrate of ZnO precursor [139]. In addition, the peaks at 2922 cm⁻¹ and 2841 cm⁻¹ is referred to the asymmetric and symmetric vibrations of –CH₂, respectively [139]. Furthermore, the stretching vibration peaks due to the carboxylate group is recorded at 1556 cm⁻¹ and 1402 cm⁻¹ [165]. Similar to Fig. 4.22, this spectral peak supports the surface functionalisation of Al-doped ZnO by oleic acid. Moreover, the vibrational band c.a. 668 cm⁻¹ is attributed to ZnO.

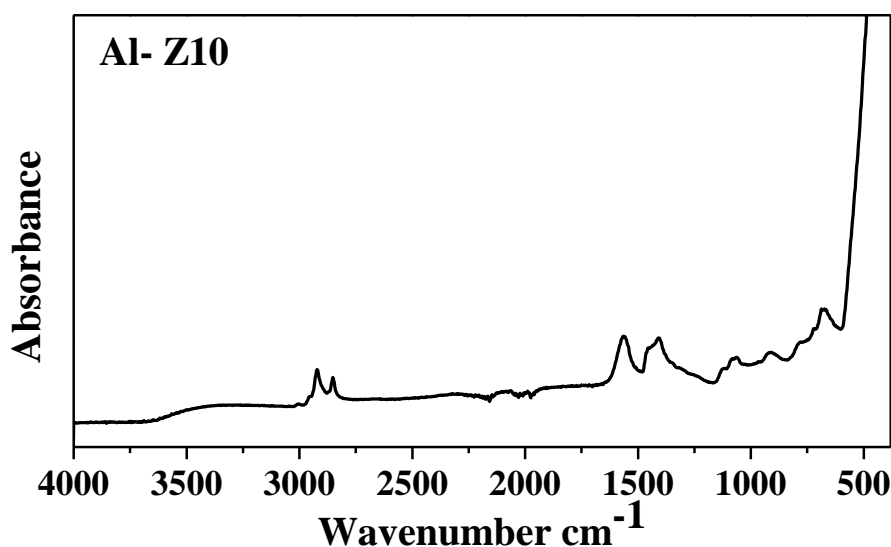


Fig. 4.39 FT-IR of Al-doped ZnO powder.

4.4.7 Absorption spectra and Tauc plot of ZnO and Al-ZnO nanoparticles

The optical properties of the samples were investigated by ultraviolet-visible (UV-Vis) spectroscopic technique. The maximum absorption (λ_{max}) peak of undoped ZnO dispersed in toluene is c.a. 355 nm. The λ_{max} value is 341 nm for 1% Al-doped ZnO and 335 nm both for 5% and 10% Al-doped ZnO. It is evident from Fig. 4.40 that there is a shift in the lower wavelength for ZnO with Al dopant, especially for 5% and 10% molar Al dopant. This hypsochromic shift in λ_{max} is attributed to the presence of the dopant. The shoulder peaks in the three Al-doped ZnO samples are associated with the semiconductor nanoparticles. The peaks are situated in the ultraviolet region and are due to the exciton band of ZnO. The

gradual shift to lower wavelength is one of the implications of Al^{3+} in the host crystal lattice [166, 167].

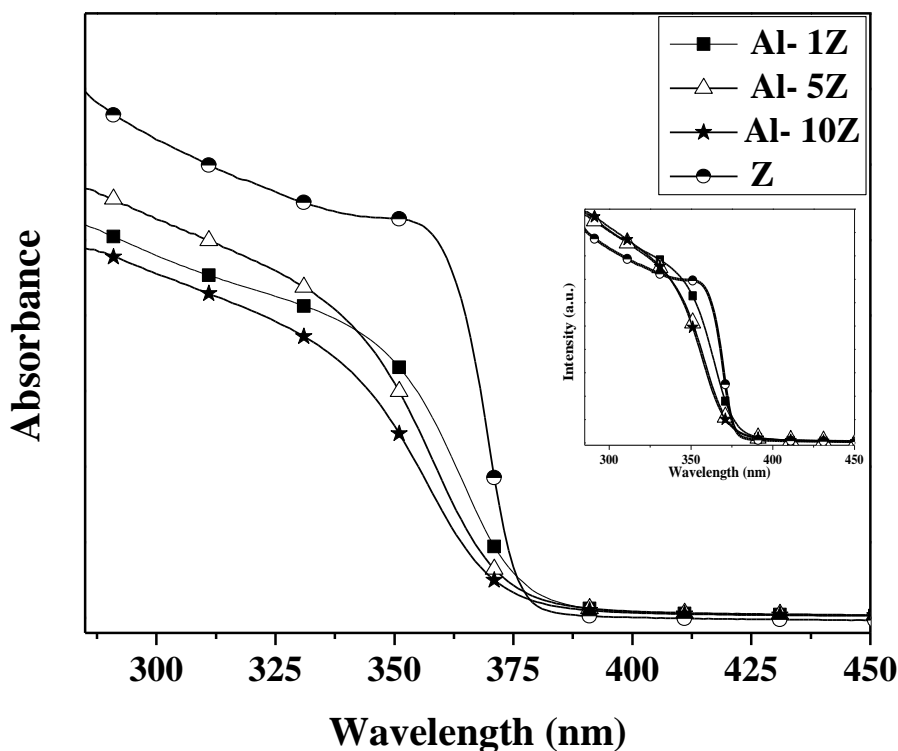


Fig. 4.40 UV-Vis spectra of ZnO and Al-ZnO colloids, inset: normalised data [164].

The effect of doping in the band gap was actualised by measuring the powdered samples with diffuse reflectance ultraviolet-visible spectroscopy (DRUV-Vis). The spectra is depicted in Fig. 4.41 Like the previous samples, the band gap of Al-ZnO samples was calculated by Kubelka-Munk function. Moreover, the relation between the absorption coefficient and the incident photon energy was discussed previously too. The band gaps of the samples are shown in Table 4.12.

Table 4.12 Comparison of average particle size and bandgaps of undoped ZnO and Al-doped ZnO at different dopant concentrations.

Sl no.	Sample name	Al conc. (EDS) (atomic %)	TEM avg. particle size (nm)	Band gap Tauc Plot (eV)
1.	Z	---	9 ± 2	3.23
4	Al-1 Z	1.60	10 ± 2	3.13
5	Al-5 Z	5.23	9 ± 2	3.16
6	Al-10 Z	9.39	8 ± 1	3.13

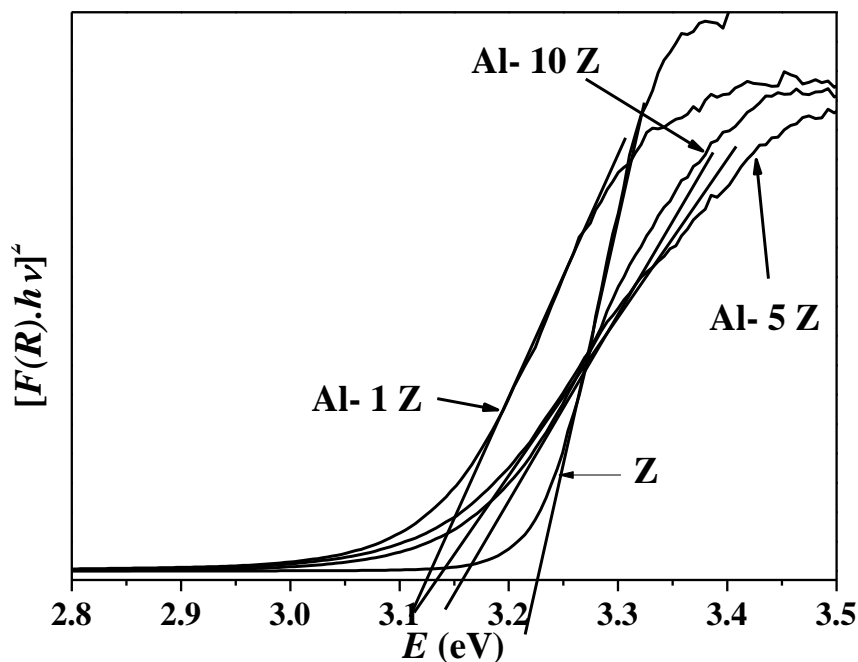


Fig. 4.41 Band gap calculation of ZnO and Al-ZnO powder using Tauc plot; inset, DRUV-Vis of ZnO and Al-doped samples [164].

4.4.8 Room temperature photoluminescence spectra of ZnO and Al-ZnO nanoparticles

The fluorescence measurement of ZnO and Al-ZnO colloidal samples was investigated at room temperature, Fig. 4.42. At the inset are the normalised emission spectra for better analysis of the luminescent peaks. The PL measurement was studied as a function of Al dopant concentration in the Al-ZnO nanoparticles in the form of colloidal dispersion. In accordance to the general principle of the fluorescence spectra of the ZnO nanoparticles, two emissions are observed: photoluminescence emission due to near band edge (NBE) emission which falls in the ultraviolet (UV) region (c.a. 380 nm) and another one arises due to defects in the crystal structure deep level (DLE) emission in the visible region (510-650 nm) [168]. The peak in the visible region is attributed to oxygen vacancies (V_O), zinc vacancies (V_{Zn}), oxygen interstitial (O_i), zinc interstitial (Zn_i), zinc substitute in oxygen site (Zn_O) and oxygen substitute in Zn site (O_{Zn}) [169]. After exciting the samples by a laser source at 332 nm, the emission of the excited electrons from the conduction band to the valence band was recorded. Two things are clearly observable. There is a blue shift and the increase in the intensity due to the presence of the dopant. The emission peaks of the samples for pure ZnO, Al-1Z, Al-5Z and Al-10Z are 377 nm (3.29 eV), 376 nm (3.29 eV), 369 nm (3.36 eV) and 366 nm (3.39 eV) respectively. The hypsochromic shift implies broadening of transition band gap with more Al concentration. This shift to lower wavelength is complementary to the shift of UV-Vis absorption spectra maximum (λ_{max}) Fig. 4.40. The filling of the lowest states in the conduction band of ZnO by electrons from the dopant may result to higher energy

of radiative recombination transition (Burstein-Moss shift) while the shallow states can be more manifested in the Tauc plot [93].

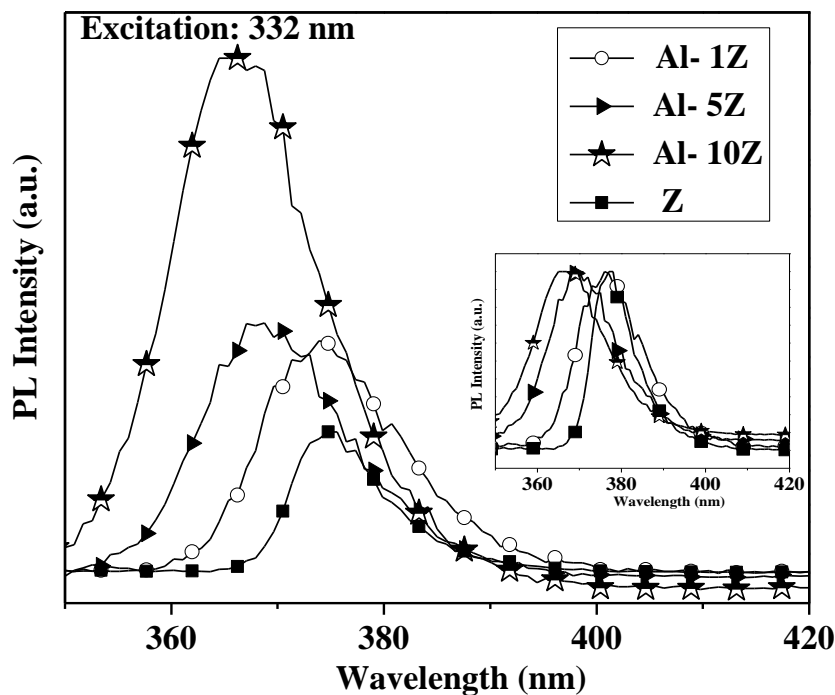


Fig. 4.42 Room temperature PL spectra of pure and Al-doped ZnO colloids [164].

4.4.9 Fluorescence spectroscopy of Al- ZME nanocomposite samples

Fig. 4.43 represents the room temperature PL measurement of neat MEH-PPV and the nanocomposite solutions. And, the excitation wavelength was 515 nm. The emission in the visible region 560 to 750 nm is from the conjugate polymer.

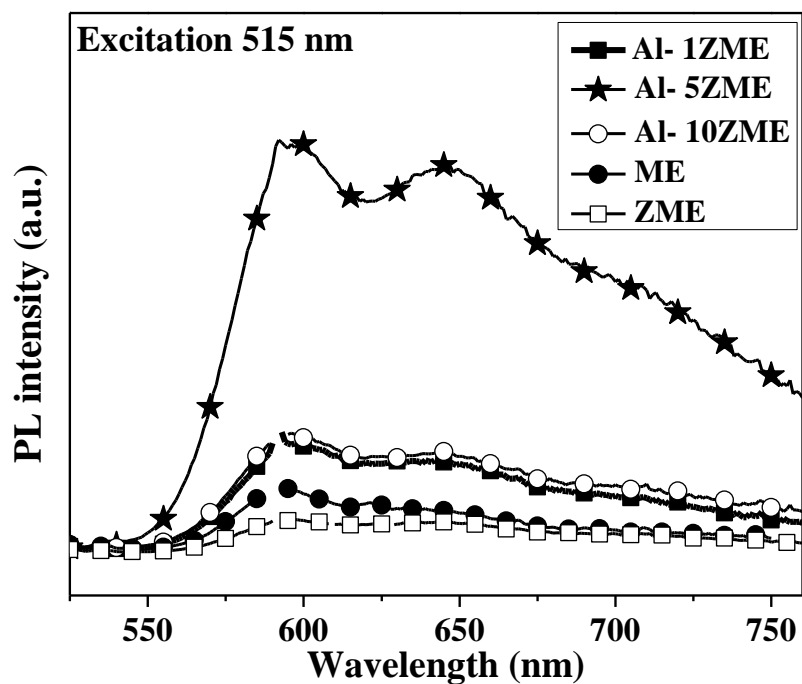


Fig. 4.43 PL spectra of neat MEH-PPV and Al- ZME nanocomposites [164].

Linking to the Fe-doped ZnO nanocomposite films, the two distinct peaks are in the emission spectrum at the same positions. Also, in this case, the ratio of intensities of the two peaks changed between pure polymer thin film and nanocomposite films in favour of the 0-1 vibronic transition due to introduction of the nanoparticle filler to the polymer matrix. No significant dependence of the peak ratio was observed with variation of Al doping concentration. According to the literature, partial filling of the conductive band of ZnO nanoparticles by electrons is expected, an impeding factor for eventual electron transfer from LUMO of MEH-PPV to the conduction band of ZnO nanoparticles [158].

4.5 PLEDs as proof-of-concept

Electroluminescence is an optoelectrical phenomenon when a material emits light due to applied potential difference or when subjected to a strong electric field. In principle, the recombination of electrons and holes due to applied electric field results in the emission of a material. With this discovery, it was possible to convert electric energy into light energy. Since its discovery in the nineteenth century, it has widely been researched and is extensively used in electronic display applications.

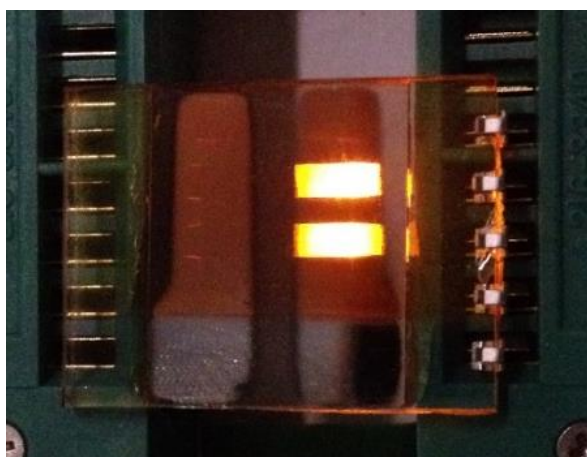


Fig. 4.44 Luminance of two pixels of ZnO-3/MEH-PPV PLED device at 10 V.

It was previously discussed that the surface functionalisation of nanoparticles makes for stable dispersion in toluene. The blending of a conjugate polymer MEH-PPV solution with the colloidal nanoparticle dispersion yields an opaque nanocomposite precursor dispersion. Then, it is deposited on a substrate for PLED device fabrication by spin-coating technique within one simple casting step. The obtained nanocomposite thin film serves as an active/emissive layer. It consists of ZnO or doped ZnO nanoparticles embedded in the MEH-PPV matrix. The concentration of nanoparticles is 50 wt%. ZnO is an n-type semiconductor and MEH-PPV is a p-type semiconductor. The hybrid heterojunction electroluminescent device was fabricated in the state-of-the-art laboratory in the

research group. The structure of the device stacked on top of each other looks like this glass substrate/ITO/PEDOT:PSS/nanocomposite/Mg. The schematic diagram of the PLED device is shown in Fig. 3.2. The optimum thickness of the active layer was about 30 nm for all devices. To illustrate the performance of prepared devices, a photograph of the ZnO-3/MEH-PPV PLED with two pixels powered at 10 V is shown in Fig. 4.44.

The role of the nanoparticles, their size and doping elements (Fe and Al) and their concentrations in PLEDs was studied in another dissertation in the research group [170]. In comparison to the neat MEH-PPV device, the organic/inorganic heterostructure hybrid device electroluminescence is enhanced, especially when doped with Al. In addition, the Fe-doped ZnO diode was found to have lower opening bias voltage due to the presence of Fe dopant in the ZnO host crystal structure. Further, when undoped ZnO nanoparticles were synthesised with varied particle size, there was an increase in the electroluminescence spectra too with an optimum for particle diameter 11 nm. Further, like the Fe-doped samples, a decrease in forwarding bias voltage was observed with the increase in particle size of the ZnO nanoparticles [170]. In order to demonstrate the effects of nanoparticle addition in the active layer, as well as to show and analyse the functional characteristics of the prepared PLEDs, and eventual benefit for application, the devices shall be characterised as sources of light rather than to study microphysics behind the diode operations.

4.5.1 Performance of the reference MEH-PPV PLED

The CIE 1931 chromaticity diagram of the PLED device prepared with MEH-PPV polymer is depicted in Fig. 4.45 (a), and with an enlarged area of interest in Fig. 4.45 (b). The colour coordinate was obtained using EL spectra of the MEH-PPV PLED powered by 10 V. An example of such EL spectra is shown in Fig. 4.45 (c). The diode emits light of yellowish-orange colour appearance with chromaticity coordinates (x 0.518, y 0.457). It can be seen that the operation point is not directly on the spectral locus, although the point is quite close to the wavelength of 583 nm, which is the maximum EL intensity emitted from the reference PLED. The chromaticity is shifted towards the white centre of the visible gamut due to contributions in the blue-green region of the emitted spectra as highlighted in Fig. 4.45 (c).

According to the previous study [170], the opening voltage of this reference diode is 5.5 V, and the maximum EL intensity is 11 800 a.u. @ 10 V. Increasing the maximum EL intensity, decreasing the opening voltage, and approaching monochromaticity are the performance indicators which represent an eventual improvement of the desired function of the prepared demonstration of the PLEDs in comparison to the reference diodes.

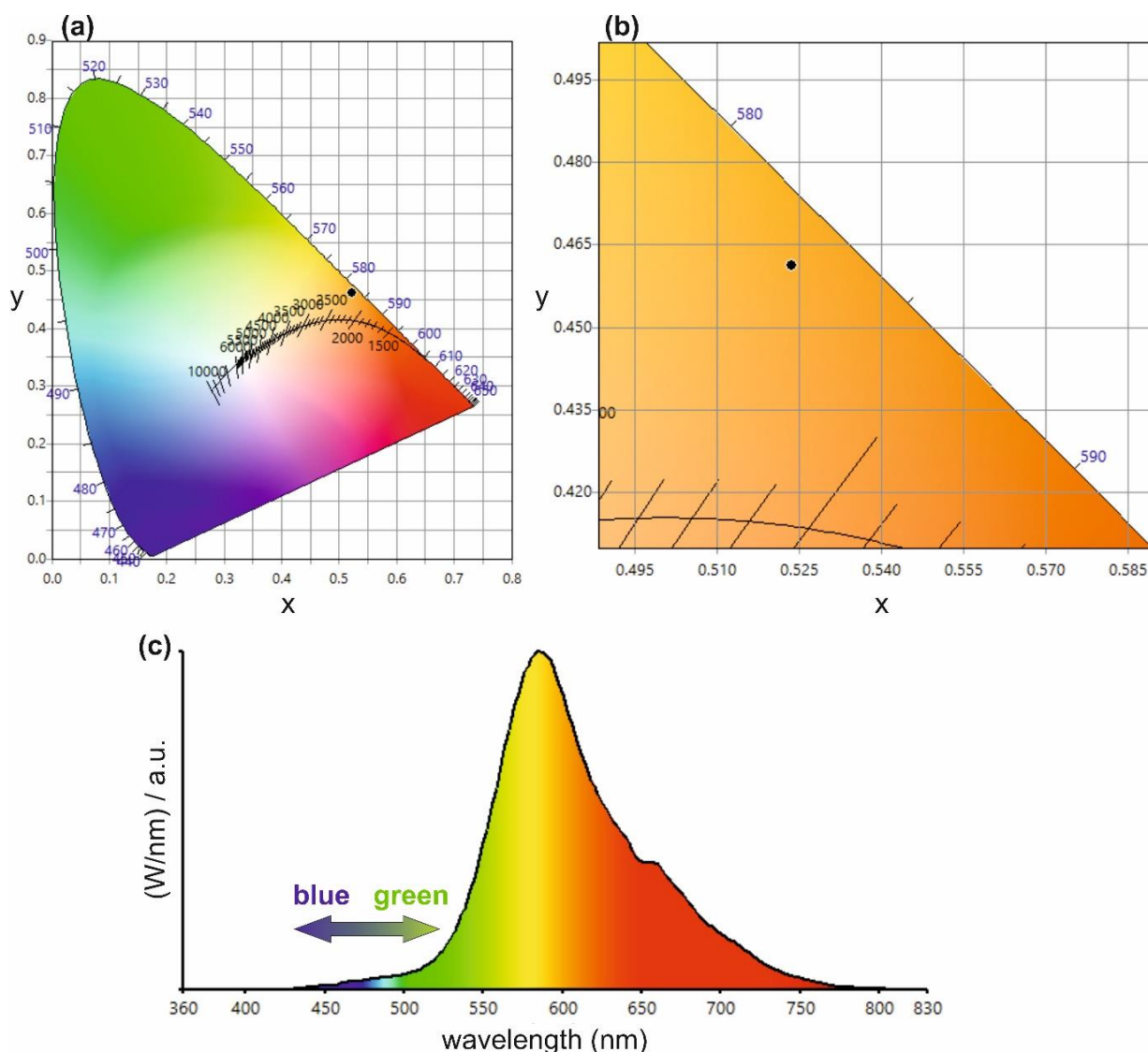


Fig. 4.45 (a) Chromaticity diagram (CIE 1931) of PLED devices fabricated with neat MEH-PPV, (b) magnified region the chromatic diagram, and (c) colour spectrum of MEH-PPV diode.

4.5.2 Performance of the undoped ZnO/MEH-PPV devices

Addition of ZnO nanoparticles to the active layer resulted in enhanced luminance of prepared diodes in comparison with the reference as documented in Fig. 4.46. The average size of the particles was always at least several times smaller than the active layer thickness (see chapter 4.2). The best performance was observed in ZnO-3/MEH-PPV sample with average particle size of about 11 nm [141, 170]. The structure of the hybrid PLED device comprises of two electrodes, a hole transporting layer (HTL), and an emissive/active nanocomposite layer. When a potential is applied to the device, electrons are generated from the low work function cathode (Mg, 3.66 eV), and holes are released from the transparent anode (ITO, 4.70 eV). PEDOT:PSS is used as an HTL stacked on the ITO layer. The holes originating from the anode pass across

the valence band (5.2 eV) of the HTL layer into the conjugate polymer MEH-PPV. The large difference between these energy levels and the valence band of ZnO (7.4 eV) creates a barrier for the holes. And, the injection and transport of electrons from the cathode can be enhanced through the conduction band of the dispersed nanoparticles ZnO (4.2 eV) to the lowest unoccupied-molecular orbital (LUMO) of MEH-PPV (3 eV) [171]. Thus, recombination of electrons and holes in the emissive layer results in the emission of light from the conjugate polymer. Moreover, ZnO nanoparticles improved the charge carrier concentration balance in the active layer due to its n-type character [172].

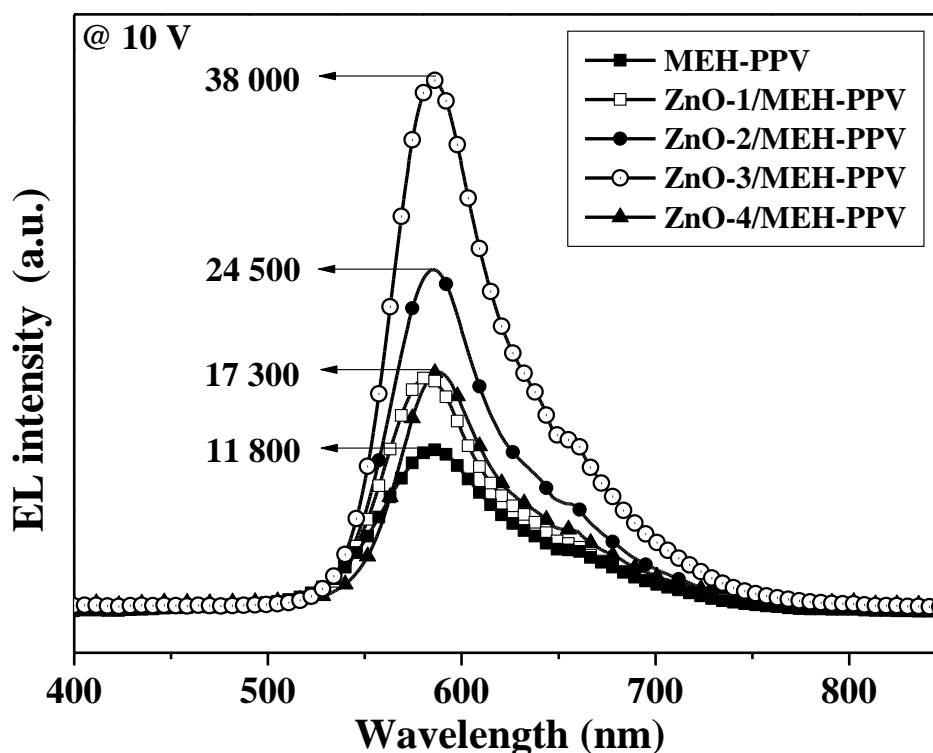


Fig. 4.46 Electroluminescence of ZnO/MEH-PPV and neat MEH-PPV diode [170].

Unlike in [172], using well-arranged nanowire forest, a simple random nanocomposite fulfils the same role in the prepared diodes [170]. This is one of the reasons behind the higher luminescent intensity of the composite active layer compared to the diode prepared by the neat polymer. The EL maximum intensity of the ZnO-3/MEH-PPV was ca 3.2 times higher than that of the reference, and the opening bias was slightly decreased from 5.5 V to 5.0 V [170]. When comparing the EL spectra shown in Fig. 4.46 with the luminescence spectra of the corresponding nanocomposites Fig. 4.18, it is evident that 0-0 transition overrides the 0-1 transition significantly. The consequence of this recombination mechanism preference is a shift of the chromaticity of the PLEDs towards the spectral locus as seen in Fig. 4.47 (a) and (b). The best performing sample has the chromaticity coordinates (x 0.532, y 0.465) closest to the wavelength of 583 nm on the monochromatic line, which is the maximum emitted from the reference

PLED device. Moreover, the prominence of the main 0-0 transition peak eradicated the emission in the blue-green region as seen in the spectrum in Fig. 4.47 (c).

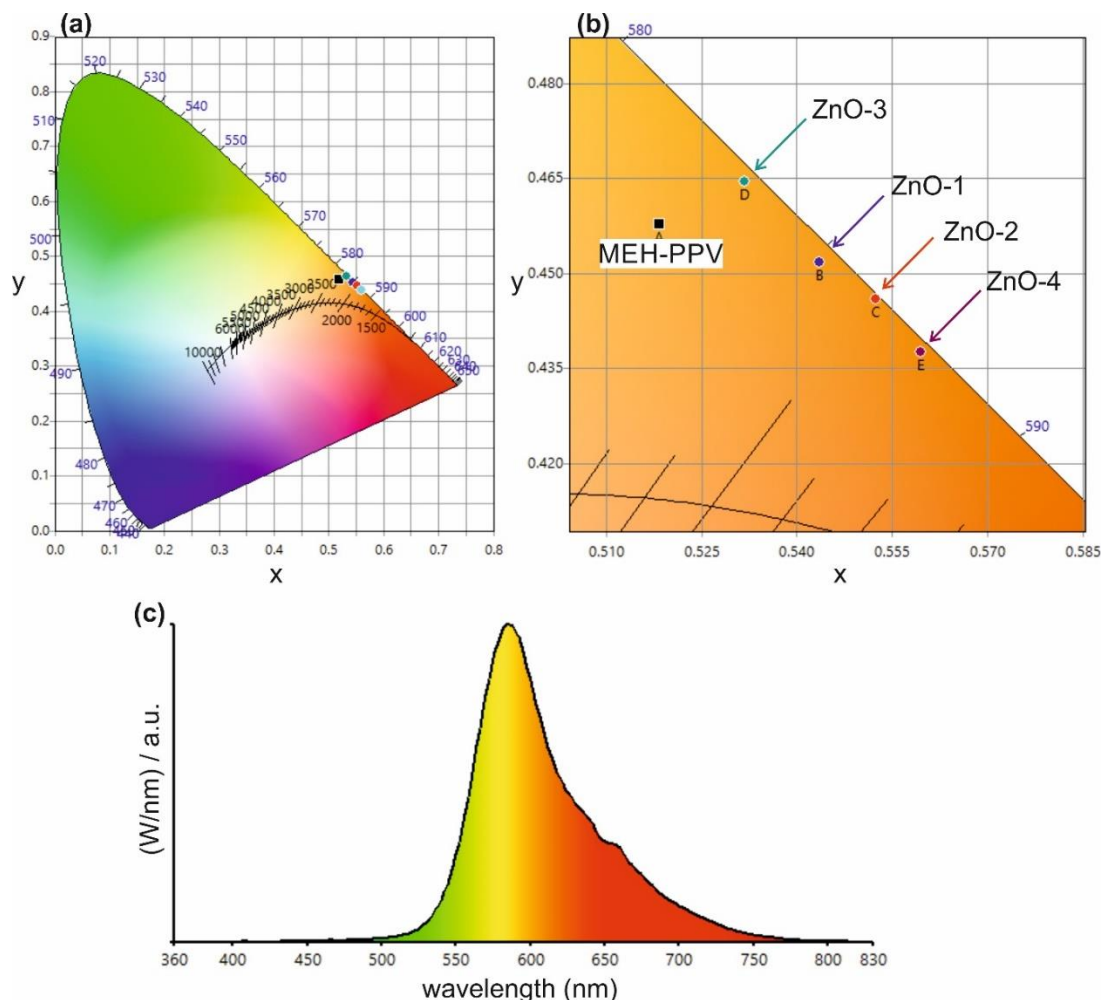


Fig. 4.47 (a) Colour space representation of neat MEH-PPV and ZnO/MEH-PPV samples, (b) image enlarged from the chromatic plot, and (c) EL spectrum of ZnO/MEH-PPV 1 diode @ 10 V.

4.5.3 Performance of the Fe-ZnO/MEH-PPV devices

To demonstrate the effect of Fe doping, particles of a size similar to ZnO-3 were prepared with three different doping levels (see chapter 4.3) and added to the active layer of nanocomposite PLEDs. The devices were prepared in the same way as the sample series of undoped ZnO nanoparticles. Thus, the PLED structure can be described as ITO/PEDOT:PSS/ $\text{Fe}_x\text{Zn}_{1-x}\text{O}$ /MEH-PPV/Mg.

The electroluminescence (EL) spectra of the fabricated PLED devices of $\text{Fe}_x\text{Zn}_{1-x}\text{O}$ /MEH-PPV, ZnO-3/MEH-PPV and neat MEH-PPV is depicted in Fig. 4.48 [141, 170]. It is evident that the EL maximum intensity decreases with increasing doping level (from 38000 a.u. for the undoped sample down to 7700 a.u. for 10 % Fe-doping level). This is expected because Fe works as a p-type dopant diminishing relatively the concentration of negative charge carriers in the

system. Moreover, it creates alternative non-radiative electron-hole recombination pathways. Nevertheless, the emission spectra of all the prepared nanocomposite devices look similar, and it is clear that the 0–0 relaxation path is preferred [170].

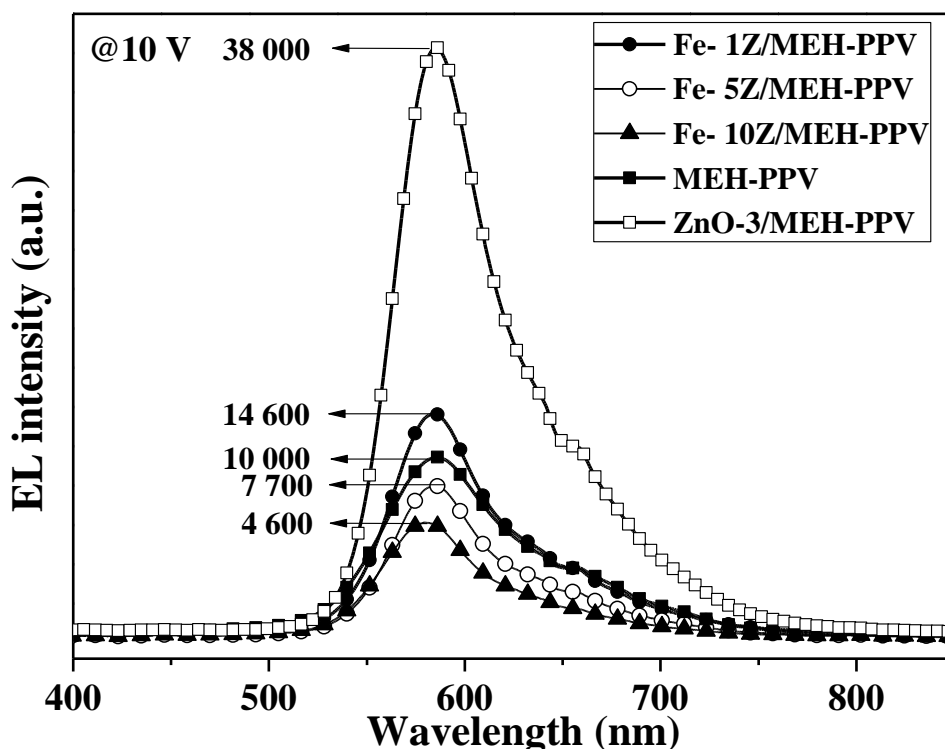


Fig. 4.48 Electroluminescence of Fe-Z/MEH-PPV, Z/MEH-PPV and MEH-PPV samples [170].

On the other hand, the opening bias decreased from 5.5 V for the reference device down to 3.5 V for sample Fe-1 Z/MEH-PPV, which is a favourable change. The opening bias decreases even more with increasing doping level down to 2.8 V for sample Fe-10 Z/MEH-PPV but, this is at the expense of the decreased EL maximum intensity which is 1.5 times lower as compared to the EL maximum intensity of the reference. The decrease in opening bias may compensate for the loss of EL intensity from the point of power efficiency if the device is operated at a lower voltage [170].

The chromaticity analysis allows for another point of view. The CIE 1931 chromaticity diagram in Fig. 4.49 (a) and especially the detail in (b) testifies for less monochromaticity than it was achieved in case of undoped samples. The spectrum in (c) recorded for sample Fe-1 Z/MEH-PPV still provided EL maximum intensity higher than was observed for the neat MEH-PPV reference diode. The blue part of the EL emission was suppressed while the green region of the spectra still carries some emission intensity. The chromaticity coordinates of the sample Fe-1 Z/MEH-PPV are (x 0.535, y 0.456). No trend was observed for the chromaticity of the samples with either doping level or EL maximum intensity.

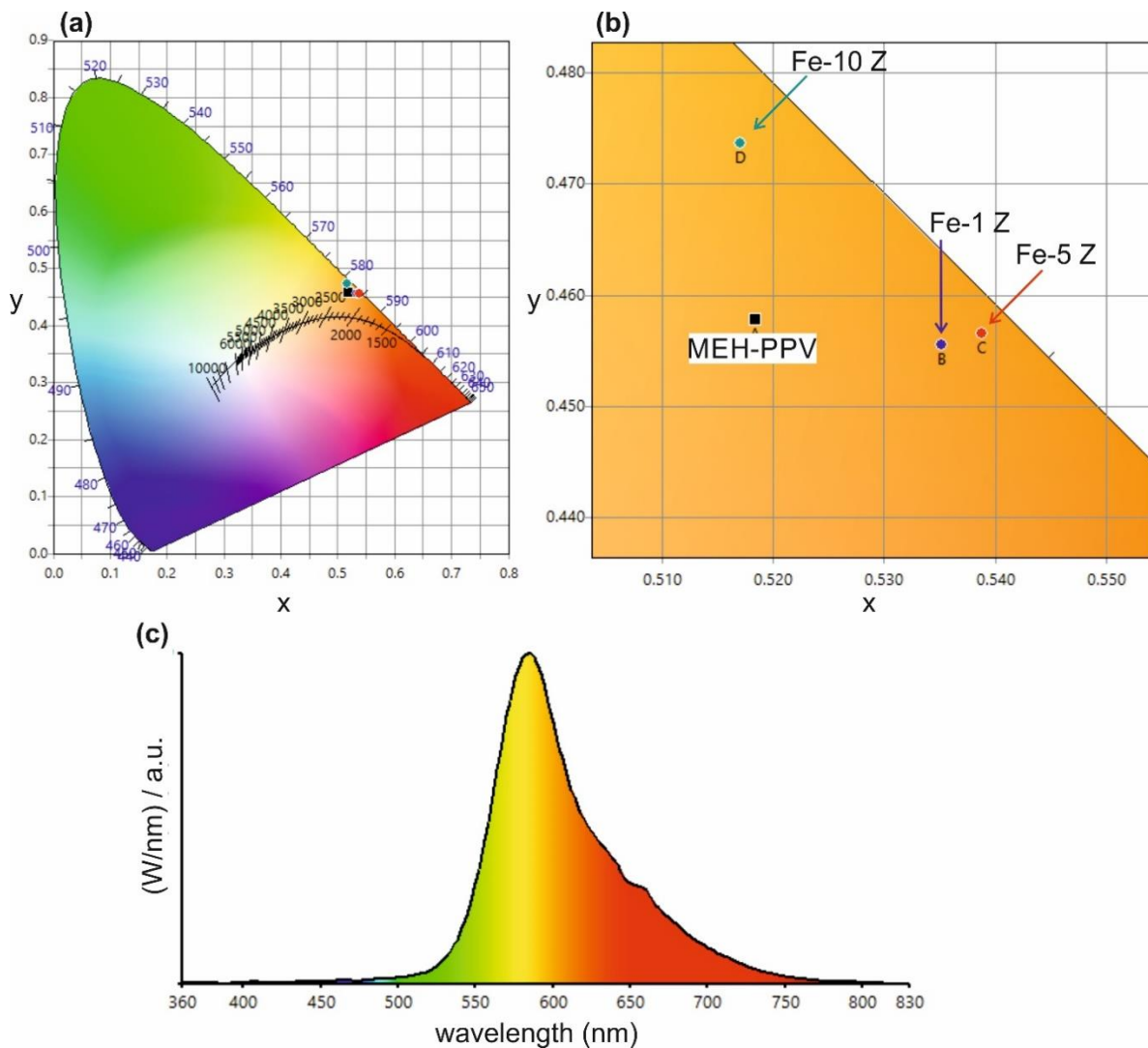


Fig. 4.49 (a) CIE 1931 diagram for PLED devices with Fe- Z/MEH-PPV samples as active layer, (b) enlarged image of the chromaticity plot, and (c) EL colour spectrum of the Fe-doped MEH-PPV diodes.

4.5.4 Performance of the Al-ZnO/MEH-PPV devices

When ZnO is doped with a trivalent dopant from the p-block elements, an excess charge carrier is available in the conduction band. Thus, Al is considered an n-type dopant. An increase of density of states (DOS) below the conduction band of the prepared Al-doped ZnO was experimentally verified by the energy-resolved electrochemical impedance spectroscopy (ER-EIS) [170]. The effect of the addition of Al-doped particles on the electroluminescence spectra of Al-Z/MEH-PPV based PLED devices were studied, Fig. 4.50 [170].

In all the electroluminescent spectra, the peaks observed in the visible region was from MEH-PPV polymer with preferential 0-0 transition as in all other prepared nanocomposite PLEDs. As with the previous samples, in order to check the efficiencies of the fabricated PLED devices, the luminescent nature of the

devices were analysed. Again, the EL maxima intensities of tested devices were compared with neat MEH-PPV reference diode. The EL intensity increases with increasing doping level. It was found that the PLED with Al-10 Z/MEH-PPV as active layers has approximately about 14 times more intense emission than the reference and 4.2 times higher than the best performing ZnO-3/MEH-PPV sample. An increased concentration of negative charge carriers in the system contributes positively to the charge carrier balance, which results in higher efficiency of radiative recombination events per unit of transferred charge through the device. The doping of the semiconductor nanocrystallite also increases the conductivity of the active layer in general. Hence the serial resistance of the device diminishes. Indeed, the opening bias was 2.8 V for all Al-doped samples, which represents a significant improvement in comparison to the reference (5.5 V) as well as with the undoped ZnO-3/MEH-PPV samples (5.0 V).

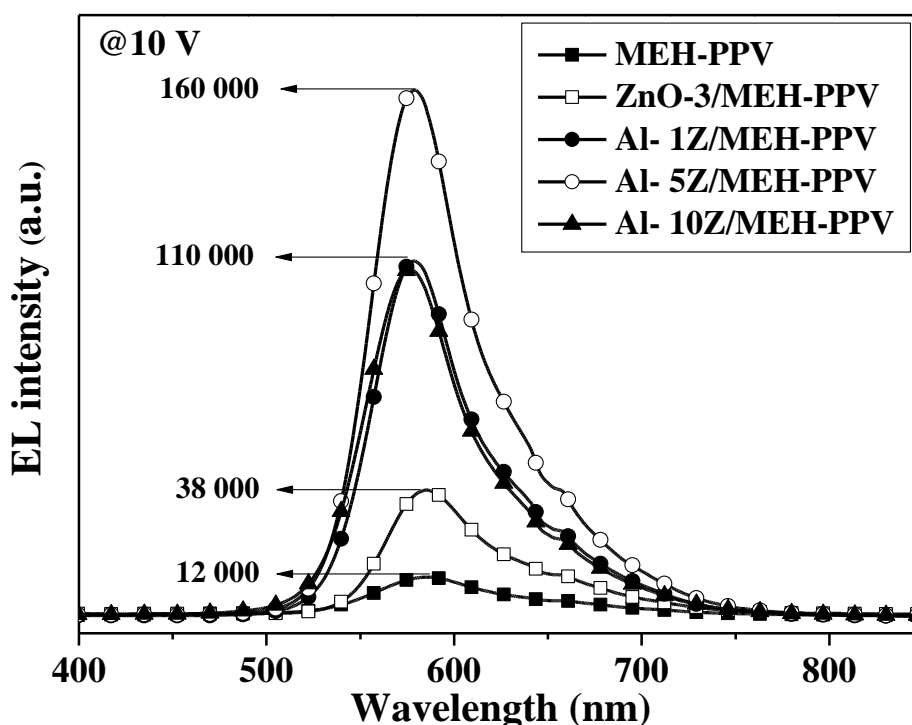


Fig. 4.50 Electroluminescence of Al-Z/MEH-PPV, Z/MEH-PPV and MEH-PPV samples [170].

The CIE 1931 chromaticity diagram with operating points of neat MEH-PPV and Al- Z/MEH-PPV diodes is displayed in Fig. 4.51. Comparing the EL spectra and the chromaticity of the diodes, it is observed that with increasing doping level and EL intensity, the chromaticity of the diodes shifted to the yellow region and approached the monochromatic locus. Al-10 Z/MEH-PPV has the highest luminescence, and in the chromaticity space, it is placed at (x 0.521, y 0.477) in the proximity of monochromatic wavelength 578 nm, unlike the diodes Al-1 Z/MEH-PPV and Al-5 Z/MEH-PPV with the coordinates (x 0.506, y 0.490) and (x 0.521, y 0.477), respectively.

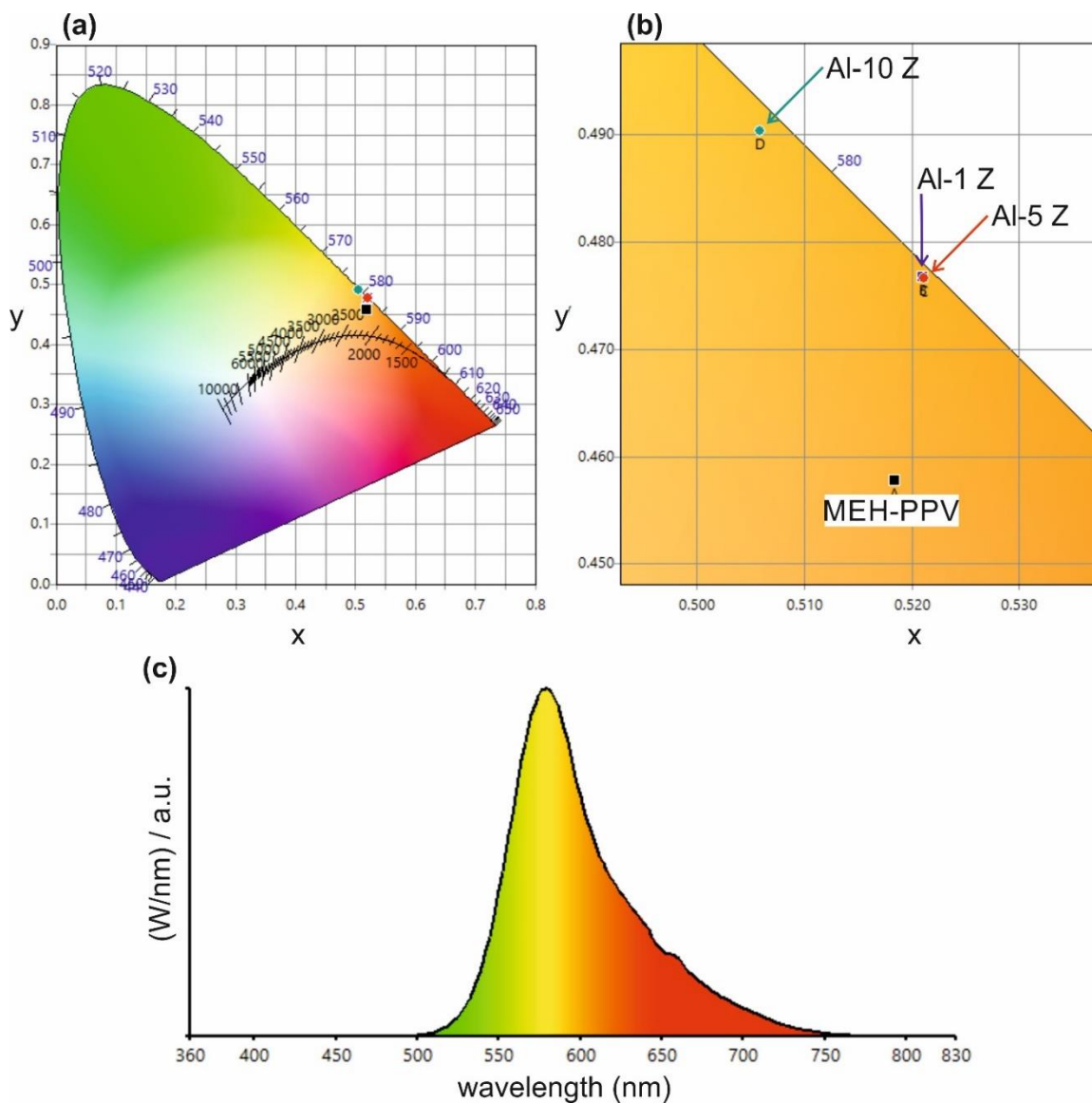


Fig. 4.51 (a) The chromatic diagram of MEH-PPV and Al-Z/MEH-PPV samples, (b) expanded image of the chromatic plot, and (c) EL spectrum of Al-Z/MEH-PPV diode.

4.5.5 Overall assessment of the performance of prepared devices

The EL emission spectra of selected best performing PLEDs from each sample series are depicted in Fig. 4.52 in order to compare the effects of the various nanofillers with the reference neat MEH-PPV diode. Addition of the ZnO nanoparticles increases the EL emission intensity in general. It can be explained by the n-type character of ZnO, which improves the charge carrier balance in the p-type MEH-PPV conductive polymer emissive layer. When the ZnO nanofiller was positively doped by Fe, a decrease of PLEDs luminance was observed for higher doping levels. In contrast to that, n-type Al doping of ZnO increased the PLEDs EL intensity largely even compared to the devices with undoped ZnO nanoparticles.

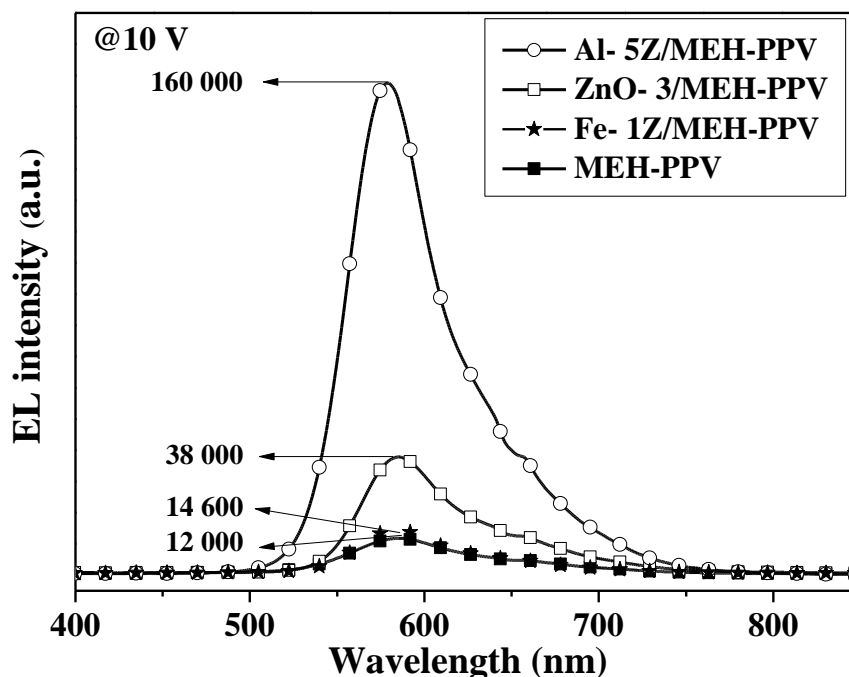


Fig. 4.52 Comparison of the best performing PLEDs from each sample series with the reference diode.

With further development in band gap engineering of ZnO nanoparticles, it can be expected that suitable doping allows for even much higher PLED efficiency. Moreover, the performance of the prepared devices demonstrated not only the application potential of the synthesised nanofillers but also the reliability of the single-step spin coating procedure in the fabrication of PLEDs. Unlike competitive layer-by-layer physical deposition methods, here the bulk heterojunction emissive layer is fabricated by spin-coating from a liquid dispersion in one step.

5. CONCLUSION

In this work, the research is focused on the microwave-assisted polyol synthesis of undoped and doped ZnO nanoparticles. The role of water molecules, oleic acid as the capping agent and dopants (Fe and Al) were investigated. Moreover, the prepared ZnO nanoparticles with varied average particle size showed different optical properties. The microwave reactor enabled the rapid and uniform heating of the reaction mixtures. As demonstrated in this work, polyol synthesis is fast and efficient preparation technique for obtaining nanocrystalline particles. Since a high boiling point solvent was employed, the reaction was conducted at high temperature, the result being the production of high crystalline nanoparticles within 15 min. And, a stable dispersion of the as-synthesised nanoparticles was possible due to surface modification by the capping agent. The nanoparticles obtained using the microwave reactor were reproducible and highly crystalline. All the particles exhibited a sharp peak in the UV region of the photoluminescence emission spectra. No emission was observed in the visible part of the spectra confirming good crystallinity of the particles and passivation of eventual surface defects. Both the solvent (diethylene glycol, DEG) and the capping agent (oleic acid, OA) have the passivation capability. In order to actualise the potential of the prepared ZnO and doped ZnO nanoparticles, the colloids were blended with a conjugate polymer MEH-PPV, deposited on a substrate by spin-coating technique and their optical properties were studied. Finally, polymer light-emitting diode (PLED) devices were prepared, and their optoelectronic characteristics were analysed.

Application-oriented synthesis of nanoparticles is a task for consideration, with all the uncertainties pertaining to it. Therefore, four synthesis studies were performed.

In the first study, the role of water molecules in ZnO nanoparticle synthesis was analysed. Here, water molecules play a significant role as they assist the hydrolysis of the zinc precursor (zinc acetate) in the initial stage of the process. The particle nanocrystallite size (as obtained by XRD) increases with the equivalent amount of water. The ZnO nanoparticles prepared from an anhydrous precursor exhibited the smallest size (9 nm). The size was increased in the case of ZnO nanoparticles prepared from dihydrate precursor (13 nm). The biggest nanoparticles were obtained from the anhydrous precursor with the addition of 4 molar equivalents of H₂O (16 nm). Thus, the water molecule controls the ZnO nanoparticle size during the synthesis. The water molecule is either supplied *in situ* from the hydrated metal precursor or from the organic medium. The intentional addition of water to DEG solvent was demonstrated as a viable method for synthesised nanoparticle size adjustment. The spectral properties can be controlled as well because they depend on the particle size. With respect to the employment of the capping agent, OA enabled stable colloidal dispersion of ZnO in toluene. There is an interaction between the surface of ZnO and the hydrophilic

head of the ligand while the hydrophobic tail, i.e. the long alkyl chains, enables good interactions with the surrounding environment of ZnO. The thickness of an OA monolayer shell on the surface of the particles can be estimated in the range 2-3 nm. Nevertheless, this organic layer does not interfere XRD based estimation of the particle size. The diameter of ZnO nanocrystallites stabilised by OA varied from 9 nm for particles prepared from anhydrous precursor to 18 nm for particles prepared from an anhydrous precursor with the addition of 4 molar equivalent of H₂O. TEM analysis confirmed the presence of isolated ZnO nanoparticles in the dispersion. When synthesis was carried out in the absence of the capping agent, an unstable suspension in toluene was observed, and TEM analysis revealed the presence of large aggregates of the nanoparticles. Moreover, OA is a barrier for transport of the source ions from the solution to the growing particle surface, which is another size controlling mechanism in the synthesis. It seems that there is a cooperative effect of the presence of water and capping agent in the reaction mixture. As a result, OA was used in synthesis throughout the rest of the work.

The second series of reactions studied size variation of ZnO nanoparticles by changing the molar concentration of the precursor to find the most proper size for further application in PLED. With increasing molar precursor concentration, the average particle size of ZnO increased in the range from 4 nm to 14 nm (as estimated from TEM images) for the molar precursor concentrations from 0.02 mol/dm³ to 0.16 mol/dm³. The sample with the smallest particle size exhibited the lowest crystallinity and broadest size distribution judging according to all of its characteristics. The observed dependence of spectral features on the nanoparticle size correlated well with the prediction by the theoretical Brus equation model. The stable dispersions of the prepared ZnO nanoparticles in toluene (due to OA) allowed mixing of the particles with MEH-PPV dissolved in toluene. Thus, homogenous thin nanocomposite films were fabricated easily by one-step spin-coating technique. It was confirmed that the addition of 50 wt% of ZnO nanoparticles does not deteriorate the polymer luminescence and, no luminescence attributable to the ZnO nanoparticles is visible when the sample is excited by UV light (332 nm). The incorporation of the nanofillers influences the ordering of the polymer chain favouring the intermolecular interaction slightly over the intramolecular one.

As a third study, band gap engineering of the semiconductor nanoparticles by doping it with metal impurities was investigated. Iron was the metal dopant employed in this part. The Fe dopant did not influence the average particle size of the nanoparticle much. Incorporation of the dopant was also confirmed by EDX spectroscopy analysis. Further, it is clear from the XPS spectra that the Fe dopant was present mainly in Fe²⁺ oxidation state. Thus, the reduction of the source ions from Fe³⁺ to Fe²⁺ proceeded during the synthesis which can be explained by the mild reducing effect of DEG. Next, the Fe-doping caused variations of the absorbance and fluorescence spectra of ZnO nanoparticles. Red-shift of the absorption edge was observed with an increase in doping concentration. The band

gap varied from 3.2 eV (for undoped sample) down to 2.5 eV (for ZnO doped with 10 % Fe). On the other hand, the increase in doping level was accompanied by the vanishing of the first absorption maxima around 350 nm. Moreover, the Fe-doping has a negative effect on the intensity of the UV peak in the fluorescence emission spectra excited at 332 nm. Thin nanocomposite films with MEH-PPV matrix were prepared from toluene dispersion. The addition of doped nanoparticles did not cause any pronounced change of the polymer photoluminescence emission intensity. On the other hand, the incorporation of the nanofillers had a similar effect on the intra- and inter-molecular interactions of polymer chains as in the case of undoped ZnO.

In the fourth study, the ZnO nanoparticles were doped with a trivalent dopant Al (p-block element) using similar concentrations as in Fe-doped ZnO samples. The variation of the particle size with Al doping concentration was not significant. The band gap estimated from Tauc plot was decreased by 0.1 eV in contrast to undoped ZnO nanoparticles but did not vary with doping concentration. On the other hand, there was a blue shift and an increase in the intensity of the PL emission peak due to the presence of the dopant. The hypsochromic shift (from 377 nm for undoped ZnO to 366 nm for 10 % Al-doped ZnO) indicates broadening of the transition band gap with increasing Al concentration, which is virtually in contradiction with the band gap estimations from UV-Vis absorption spectra. It could be that, not only new states are created below the conduction band of ZnO, but also the lowest states in the conduction band are partially filled by the electrons from the dopant. Thin nanocomposite films with MEH-PPV matrix were prepared from toluene dispersion, and the addition of doped nanoparticles yielded similar results as in the previous two studies. It can be concluded that, the observed features are due to the incorporation of the nanofillers. It is a general effect of the nanocomposite formation, and no specific manifestations of particle doping were observed in the PL spectra.

The last part of the dissertation was focused on the demonstration of the potential of synthesised particles as fillers for nanocomposites applicable in electronics. PLEDs using synthesised nanoparticles embedded in MEH-PPV polymer matrix were prepared and studied within the framework of another dissertation run in the research group [170]. This previous study was focused on detailed analysis of mechanisms and the role of the nanoparticles in the prepared devices. Here, the fabrication of the PLEDs allowed selecting the optimum size of the nanoparticles first. The best performance of nanocomposite PLEDs was achieved for ZnO nanoparticles of ca 11 nm in diameter. It was also confirmed that the presence of OA surface shell has no detrimental effect on the nanoparticulate filler function in the device. Next, the emphasis was put on further development of the prepared diode characterisation and interpretation of the effects of ZnO nanoparticle addition and their doping. The prepared PLEDs were dealt as sources of coloured light, and the results were viewed from the point of practical application. A PLED with the active layer prepared from neat MEH-

PPV was used as a reference. It emitted a yellowish-orange light of low intensity. The addition of ZnO nanoparticles enhanced the luminance of the PLEDs significantly while the opening voltage was lowered slightly. The chromaticity of ZnO/MEH-PPV diodes approached the spectral locus indicating monochromaticity of emitted light. Incorporation of Fe doped ZnO nanoparticles to the active layer affected the opening voltage much more positively; however, it is at the expense of the electroluminescence intensity. Fe is a positive dopant to ZnO. Hence, it contributes to the charge carrier imbalance compared to undoped ZnO counterparts and lowers the efficiency of the diode. The monochromaticity of the emitted light is also not that good as in the case of undoped ZnO/MEH-PPV PLEDs. On the other hand, it was found that Al-doping had an extremely positive effect on both the EL intensity and lowering of the opening bias voltage. Al is a negative dopant and contributes positively to the charge carrier balance in the diode. The application of Al-doped nanoparticles resulted in the shift of the emitted light to the yellow gamut very close to the spectral locus. The best performing Al-doped ZnO MEH-PPV PLED was about 13 times brighter than the neat MEH-PPV reference device.

CLOSING REMARKS

Contribution to science and practice

ZnO semiconductor nanoparticles is a widely researched material. The versatility of the material is eminent in various research fields and its applicability in many scientific areas. In addition to that, the characteristics of ZnO nanoparticles can be altered and tailored according to the requirement for various application purposes. In this work, for the preparation of PLED devices, the optical properties of ZnO nanoparticles were tailored for better performance of the devices. Bandgap engineering is one of the ways of achieving it. The intentional addition of foreign metal ions into the host atom alters the optical characteristics of the host crystal lattice. In this work, undoped ZnO and doped ZnO nanoparticles possessed characteristics different from each other due to average particle size, types and concentration of dopants. When ZnO nanoparticles were prepared with different molar precursor concentration, the average particle size of the nanocrystals varied. With the increase in molar precursor concentration, there was an increase in the particle size too. However, when Fe and Al dopants were used to dope ZnO nanoparticles, the particle size differences were not very significant. It, however, altered its optical properties due to the different concentration of the dopants. The absorbance and fluorescence results confirmed the effects of doping on ZnO nanoparticles. The polyol synthesis of undoped and doped ZnO nanoparticles in a microwave reactor provides an efficient and rapid technique to prepare semiconductor nanoparticles. The high boiling point multivalent alcohol is characterised by reduction potential of some metal precursors into metal ions of lower valency state. With the first use of the polyol technique by Fievet, Lagier and Figlarz in 1989 [44], it has since become a reliable method for nanoparticle synthesis. One of the main advantages of the polyol solvent is its ability to solubilise metal precursors during the reaction. The solubility is often considered equivalent to water. This is advantageous as it allows the use of easily-available and economical metal salts as precursors for metal nanoparticles. Even during the synthesis of nanoparticles, the multidentate nature of the solvent leads to a good chelating effect on to the metal salts. This effect usually controls particle nucleation, growth and agglomeration of the final product formed. However, large nanoparticle aggregates were produced in our synthesis. To further elaborate the effectiveness of the polyol solvent, the colloidal stability was improved by utilisation of oleic acid as a capping agent. It delivers stabilising effect by binding carboxyl group to the surface of the nanoparticles. Not only this, surface-modified ZnO, when mixed with conjugate polymer MEH-PPV, brings in a different flavour in terms of application in the fabrication of optoelectronic devices. The nanocomposite of the ZnO-based filler with the conjugate polymer functions as an active/emissive layer in the fabricated PLED device. From the electroluminescence spectra, it was observed that the addition of fillers enhances the luminescent intensity. The

highest luminance was observed in case of Al-doped ZnO. Moreover, Al-ZnO samples related diodes had lower opening voltages (2.8 V) compared to the one with undoped ZnO nanoparticles related PLED diodes (5.0 V). For Fe-doped ZnO based device, the forward bias voltage (2.8 V) was reduced reasonably, when compared with its undoped ZnO nanoparticle analogue (5.0 V) but, it was at the expense of the EL intensity.

The work contributes by delivery of the original knowledge about the role of ZnO precursor concentrations, water and the use of oleic acid as a capping agent in the synthesis of ZnO nanoparticles. Based on the obtained results, it is possible to intentionally alter the size, band gaps and optical properties (3.18 eV to 3.34 eV). Moreover, the electronic properties of ZnO can be tuned by doping. Fe and Al dopants showed different optical characteristics at different dopant concentrations (1, 5 and 10 atomic %). This will help us to rationalise the particle synthesis.

The prepared surface-functionalised ZnO nanoparticles were used for nanocomposite preparation with standard conductive polymer MEH-PPV and thin films made from these materials were used as active layers in the fabrication of PLEDs. It was observed that pure ZnO nanoparticles (fillers) significantly enhanced the luminescence of the devices. The use of Fe-doped ZnO nanoparticles causes depreciation in the EL intensity; however, it lowered the forward bias voltage needed to power the device. Contrary to Fe dopant, doping of ZnO with Al resulted in much higher EL intensity of the devices as well as in lowering of the opening voltage.

Ongoing research and future prospect

Microwave-assisted synthesis of ZnO nanoparticles with varied reaction conditions and dopants were investigated. The polyol reaction method was employed for all the syntheses and optimised in the condition of our research laboratories. The main achievement is represented by the introduction of the microwave-assisted heating of the reaction mixture. Preparation of heavily n-doped ZnO nanoparticles will be the next logical step in the continuation of the present research. Besides Al, In- and Ga-doped ZnO shall be considered.

The work was not confined to synthesis alone, a series of thin-films were cast by spin-coating technique and its optical and electronic properties studied. As an actualisation of the applicability of the synthesised semiconductor nanoparticles, the nanocomposite was cast as an active/emissive layer in the fabrication of PLED devices. Extensive experience of electronic devices fabrication and testing was gained in the research group.

REFERENCES

- [1] NJOKI, P.N., LIM, I.I.S., MOTT, D., PARK, H.Y., KHAN, B., MISHRA, S., SUJAKUMAR, R., LUO, J. and ZHONG, C.J. Size correlation of optical and spectroscopic properties for gold nanoparticles. *Journal of Physical Chemistry C* [online]. 2007, **111**(40), 14664–14669. ISSN 19327447.
- [2] BOISSEAU, P. and LOUBATON, B. Nanomedicine, nanotechnology in medicine. *Comptes Rendus Physique* [online]. 2011, **12**(7), 620–636. ISSN 16310705. Available at: <http://dx.doi.org/10.1016/j.crhy.2011.06.001>
- [3] LEE, J.H., MIRZAEI, A., KIM, J.Y., KIM, J.H., KIM, H.W. and KIM, S.S. Optimization of the surface coverage of metal nanoparticles on nanowires gas sensors to achieve the optimal sensing performance. *Sensors and Actuators, B: Chemical* [online]. 2020, **302**(December 2018), 127196. ISSN 09254005. Available at: <https://doi.org/10.1016/j.snb.2019.127196>
- [4] PRASAD, R., BHATTACHARYYA, A. and NGUYEN, Q.D. Nanotechnology in sustainable agriculture: Recent developments, challenges, and perspectives. *Frontiers in Microbiology* [online]. 2017, **8**(JUN), 1–13. ISSN 1664302X.
- [5] EBRAHIMI, Y., PEIGHAMBARDUST, S.J., PEIGHAMBARDUST, S.H. and KARKAJ, S.Z. Development of Antibacterial Carboxymethyl Cellulose-Based Nanobiocomposite Films Containing Various Metallic Nanoparticles for Food Packaging Applications. *Journal of Food Science* [online]. 2019, **84**(9), 2537–2548. ISSN 17503841.
- [6] ALVES, T.E.P., KOLODZIEJ, C., BURDA, C. and FRANCO, A. Effect of particle shape and size on the morphology and optical properties of zinc oxide synthesized by the polyol method. *Materials and Design* [online]. 2018, **146**, 125–133. ISSN 18734197. Available at: <https://doi.org/10.1016/j.matdes.2018.03.013>
- [7] LU, L.T., TUNG, L.D., ROBINSON, I., UNG, D., TAN, B., LONG, J., COOPER, A.I., FERNIG, D.G. and THANH, N.T.K. Size and shape control for water-soluble magnetic cobalt nanoparticles using polymer ligands. *Journal of Materials Chemistry* [online]. 2008, **18**(21), 2453–2458. ISSN 09599428.
- [8] AN, K. and SOMORJAI, G.A. Size and Shape Control of Metal Nanoparticles for Reaction Selectivity in Catalysis. *ChemCatChem* [online]. 2012, **4**(10), 1512–1524. ISSN 18673880.
- [9] KIM, H.J., ROH, D.K., JUNG, H.S. and KIM, D.S. Size and shape control of monoclinic vanadium dioxide thermochromic particles for smart window applications. *Ceramics International* [online]. 2019, **45**(3), 4123–4127. ISSN 02728842. Available at: <https://doi.org/10.1016/j.ceramint.2018.11.036>
- [10] WU, Z., YANG, S. and WU, W. Shape control of inorganic nanoparticles

- from solution. *Nanoscale* [online]. 2016, **8**(3), 1237–1259. ISSN 20403372.
- [11] FIEVET, F., AMMAR-MERAH, S., BRAYNER, R., CHAU, F., GIRAUD, M., MAMMERI, F., PERON, J., PIQUEMAL, J.Y., SICARD, L. and VIAU, G. The polyol process: a unique method for easy access to metal nanoparticles with tailored sizes, shapes and compositions. *Chemical Society Reviews* [online]. 2018, **47**(14), 5187–5233. ISSN 14604744.
- [12] NIKAM, A. V., PRASAD, B.L.V. and KULKARNI, A.A. Wet chemical synthesis of metal oxide nanoparticles: A review. *CrystEngComm* [online]. 2018, **20**(35), 5091–5107. ISSN 14668033.
- [13] CHEN, J., MA, Q., WU, X.J., LI, L., LIU, J. and ZHANG, H. Wet-Chemical Synthesis and Applications of Semiconductor Nanomaterial-Based Epitaxial Heterostructures. *Nano-Micro Letters* [online]. 2019, **11**(1), 1–28. ISSN 21505551. Available at: <https://doi.org/10.1007/s40820-019-0317-6>
- [14] MOURDIKOU DIS, S., MONTES-GARCÍA, V., RODAL-CEDEIRA, S., WINCKELMANS, N., PÉREZ-JUSTE, I., WU, H., BALS, S., PÉREZ-JUSTE, J. and PASTORIZA-SANTOS, I. Highly porous palladium nanodendrites: Wet-chemical synthesis, electron tomography and catalytic activity. *Dalton Transactions* [online]. 2019, **48**(11), 3758–3767. ISSN 14779234.
- [15] WANG, Y. and YANG, H. Oleic acid as the capping agent in the synthesis of noble metal nanoparticles in imidazolium-based ionic liquids. *Chemical Communications* [online]. 2006, (24), 2545–2547. ISSN 13597345.
- [16] SHARMA, K.S., NINGTHOUJAM, R.S., DUBEY, A.K., CHATTOPADHYAY, A., PHAPALE, S., JULURI, R.R., MUKHERJEE, S., TEWARI, R., SHETAKE, N.G., PANDEY, B.N. and VATSA, R.K. Synthesis and characterization of monodispersed water dispersible Fe₃O₄ nanoparticles and in vitro studies on human breast carcinoma cell line under hyperthermia condition. *Scientific Reports* [online]. 2018, **8**(1), 1–11. ISSN 20452322. Available at: <http://dx.doi.org/10.1038/s41598-018-32934-w>
- [17] AJITHA, B., KUMAR REDDY, Y.A., REDDY, P.S., JEON, H.J. and AHN, C.W. Role of capping agents in controlling silver nanoparticles size, antibacterial activity and potential application as optical hydrogen peroxide sensor. *RSC Advances* [online]. 2016, **6**(42), 36171–36179. ISSN 20462069.
- [18] AKHTAR, M.S., KHAN, M.A., JEON, M.S. and YANG, O.B. Controlled synthesis of various ZnO nanostructured materials by capping agents-assisted hydrothermal method for dye-sensitized solar cells. *Electrochimica Acta* [online]. 2008, **53**(27), 7869–7874. ISSN 00134686.
- [19] CAMPISI, S., SCHIAVONI, M., CHAN-THAW, C.E. and VILLA, A. Untangling the role of the capping agent in nanocatalysis: Recent advances and perspectives. *Catalysts* [online]. 2016, **6**(12), 1–21. ISSN 20734344.
- [20] BANDULASENA, M. V., VLADISAVLJEVIĆ, G.T., ODUNMBAKU,

- O.G. and BENYAHIA, B. Continuous synthesis of PVP stabilized biocompatible gold nanoparticles with a controlled size using a 3D glass capillary microfluidic device. *Chemical Engineering Science* [online]. 2017, **171**, 233–243. ISSN 00092509.
- [21] ISHIZAKI, T., YATSUGI, K. and AKEDO, K. Effect of particle size on the magnetic properties of Ni nanoparticles synthesized with trioctylphosphine as the capping agent. *Nanomaterials* [online]. 2016, **6**(9). ISSN 20794991.
- [22] BELHAJ, M., DRIDI, C. and ELHOUCHE, H. PFE: ZnO hybrid nanocomposites for OLED applications: Fabrication and photophysical properties. *Journal of Luminescence* [online]. 2015, **157**, 53–57. ISSN 00222313.
- [23] MÜLLER, K., BUGNICOURT, E., LATORRE, M., JORDA, M., SANZ, Y.E., LAGARON, J.M., MIESBAUER, O., BIANCHIN, A., HANKIN, S., BÖLZ, U., PÉREZ, G., JESDINSZKI, M., LINDNER, M., SCHEUERER, Z., CASTELLÓ, S. and SCHMID, M. Review on the processing and properties of polymer nanocomposites and nanocoatings and their applications in the packaging, automotive and solar energy fields. *Nanomaterials* [online]. 2017, **7**(4). ISSN 20794991.
- [24] LI, L., LIANG, J., CHOU, S.Y., ZHU, X., NIU, X., YU, Z. and PEI, Q. A solution processed flexible nanocomposite electrode with efficient light extraction for organic light emitting diodes. *Scientific Reports* [online]. 2014, **4**, 1–8. ISSN 20452322.
- [25] ZHAN, C., YU, G., LU, Y., WANG, L., WUJCIK, E. and WEI, S. Conductive polymer nanocomposites: a critical review of modern advanced devices. *Journal of Materials Chemistry C* [online]. 2017, **5**(7), 1569–1585. ISSN 20507526.
- [26] THANH, N.T.K., MACLEAN, N. and MAHIDDINE, S. Mechanisms of nucleation and growth of nanoparticles in solution. *Chemical Reviews* [online]. 2014, **114**(15), 7610–7630. ISSN 15206890.
- [27] CHU, D.B.K., OWEN, J.S. and PETERS, B. Nucleation and Growth Kinetics from LaMer Burst Data. *Journal of Physical Chemistry A* [online]. 2017, **121**(40), 7511–7517. ISSN 15205215.
- [28] WHITEHEAD, C.B., ÖZKAR, S. and FINKE, R.G. LaMer’s 1950 Model for Particle Formation of Instantaneous Nucleation and Diffusion-Controlled Growth: A Historical Look at the Model’s Origins, Assumptions, Equations, and Underlying Sulfur Sol Formation Kinetics Data. *Chemistry of Materials* [online]. 2019, **31**(18), 7116–7132. ISSN 15205002.
- [29] POLTE, J. Fundamental growth principles of colloidal metal nanoparticles - a new perspective. *CrystEngComm* [online]. 2015, **17**(36), 6809–6830. ISSN 14668033.
- [30] HORIKOSHI, S. and SERPONE, N. Introduction to Nanoparticles and Nanotoxicology. In: *Microwaves in Nanoparticle Synthesis: Fundamentals*

- and Applications* [online]. B.m.: Wiley-VCH Verlag GmbH & Co. KGaA, 2013, p. 1–24. ISBN 9780128014066. Available at: <http://linkinghub.elsevier.com/retrieve/pii/B9780128014066000017>
- [31] DE MELLO, L.B., VARANDA, L.C., SIGOLI, F.A. and MAZALI, I.O. Co-precipitation synthesis of (Zn-Mn)-co-doped magnetite nanoparticles and their application in magnetic hyperthermia. *Journal of Alloys and Compounds* [online]. 2019, **779**, 698–705. ISSN 09258388. Available at: <https://doi.org/10.1016/j.jallcom.2018.11.280>
- [32] VIJAYAPRASATH, G., MURUGAN, R., ASAITHAMBI, S., SAKTHIVEL, P., MAHALINGAM, T., HAYAKAWA, Y. and RAVI, G. Structural and magnetic behavior of Ni/Mn co-doped ZnO nanoparticles prepared by co-precipitation method. *Ceramics International* [online]. 2016, **42**(2), 2836–2845. ISSN 02728842. Available at: <http://dx.doi.org/10.1016/j.ceramint.2015.11.019>
- [33] ZENG, X. and QIN, W. Synthesis of MoS₂ nanoparticles using MoO₃ nanobelts as precursor via a PVP-assisted hydrothermal method. *Materials Letters* [online]. 2016, **182**, 347–350. ISSN 18734979.
- [34] KUBRA, K.T., SHARIF, R., PATIL, B., JAVAID, A., SHAHZADI, S., SALMAN, A., SIDDIQUE, S. and ALI, G. Hydrothermal synthesis of neodymium oxide nanoparticles and its nanocomposites with manganese oxide as electrode materials for supercapacitor application. *Journal of Alloys and Compounds* [online]. 2020, **815**. ISSN 09258388.
- [35] FOTUKIAN, S.M., BARATI, A., SOLEYMANI, M. and ALIZADEH, A.M. Solvothermal synthesis of CuFe₂O₄ and Fe₃O₄ nanoparticles with high heating efficiency for magnetic hyperthermia application. *Journal of Alloys and Compounds* [online]. 2020, **816**, 152548. ISSN 09258388. Available at: <https://doi.org/10.1016/j.jallcom.2019.152548>
- [36] ALOMAR, M., LIU, Y., CHEN, W. and FIDA, H. Controlling the growth of ultrathin MoS₂ nanosheets/CdS nanoparticles by two-step solvothermal synthesis for enhancing photocatalytic activities under visible light. *Applied Surface Science* [online]. 2019, **480**(November 2018), 1078–1088. ISSN 01694332. Available at: <https://doi.org/10.1016/j.apsusc.2019.03.014>
- [37] LEMARCHAND, A., RÉMONDIÈRE, F., JOUIN, J., THOMAS, P. and MASSON, O. Crystallization Pathway of Size-Controlled SnO₂ Nanoparticles Synthesized via a Nonaqueous Sol-Gel Route. *Crystal Growth and Design* [online]. 2020, **20**(2), 1110–1118. ISSN 15287505.
- [38] CALVO-DE LA ROSA, J. and SEGARRA, M. Optimization of the Synthesis of Copper Ferrite Nanoparticles by a Polymer-Assisted Sol-Gel Method. *ACS Omega* [online]. 2019, **4**(19), 18289–18298. ISSN 24701343.
- [39] DONG, H., CHEN, Y.C. and FELDMANN, C. Polyol synthesis of nanoparticles: status and options regarding metals, oxides, chalcogenides, and non-metal elements. *Green Chemistry* [online]. 2015, **17**(8), 4107–

4132. ISSN 14639270.

- [40] FUJIEDA, S., GAUDISSION, T., GRENÈCHE, J.M., FRANÇOIS, M. and AMMAR, S. Synthesis of magnetic wires from polyol-derived Fe-glycolate wires. *Nanomaterials* [online]. 2020, **10**(2), 3–9. ISSN 20794991.
- [41] KUMARESAN, N., RAMAMURTHI, K., RAMESH BABU, R., SETHURAMAN, K. and MOORTHY BABU, S. Hydrothermally grown ZnO nanoparticles for effective photocatalytic activity. *Applied Surface Science* [online]. 2017, **418**, 138–146. ISSN 01694332. Available at: <http://dx.doi.org/10.1016/j.apsusc.2016.12.231>
- [42] LIU, X., LIU, J., ZHANG, S., NAN, Z. and SHI, Q. Structural, Magnetic, and Thermodynamic Evolutions of Zn-Doped Fe₃O₄ Nanoparticles Synthesized Using a One-Step Solvothermal Method. *Journal of Physical Chemistry C* [online]. 2016, **120**(2), 1328–1341. ISSN 19327455.
- [43] CAO, E., YANG, Y., CUI, T., ZHANG, Y., HAO, W., SUN, L., PENG, H. and DENG, X. Effect of synthesis route on electrical and ethanol sensing characteristics for LaFeO_{3-δ} nanoparticles by citric sol-gel method. *Applied Surface Science* [online]. 2017, **393**, 134–143. ISSN 01694332. Available at: <http://dx.doi.org/10.1016/j.apsusc.2016.10.013>
- [44] FIEVET, F., LAGIER, J.P. and FIGLARZ, M. Preparing Monodisperse Metal Powders in Micrometer and Submicrometer Sizes by the Polyol Process. *MRS Bulletin* [online]. 1989, **14**(12), 29–34. ISSN 19381425.
- [45] RAMAMOORTHY, R.K., VIOLA, A., GRINDI, B., PERON, J., GATEL, C., HYTCH, M., ARENAL, R., SICARD, L., GIRAUD, M., PIQUEMAL, J.Y. and VIAU, G. One-Pot Seed-Mediated Growth of Co Nanoparticles by the Polyol Process: Unraveling the Heterogeneous Nucleation. *Nano Letters* [online]. 2019, **19**(12), 9160–9169. ISSN 15306992.
- [46] JOSHI, R., KUMAR, P., GAUR, A. and ASOKAN, K. Structural, optical and ferroelectric properties of V doped ZnO. *Applied Nanoscience* [online]. 2014, **4**(5), 531–536. ISSN 2190-5509. Available at: <http://link.springer.com/10.1007/s13204-013-0231-z>
- [47] MENG, A., XING, J., LI, Z. and LI, Q. Cr-Doped ZnO Nanoparticles: Synthesis, Characterization, Adsorption Property, and Recyclability. *ACS Applied Materials and Interfaces* [online]. 2015, **7**(49), 27449–27457. ISSN 19448252.
- [48] BELKHAOUI, C., LEFI, R., MZABI, N. and SMAOUI, H. Synthesis, optical and electrical properties of Mn doped ZnO nanoparticles. *Journal of Materials Science: Materials in Electronics* [online]. 2018, **29**(8), 7020–7031. ISSN 1573482X. Available at: <http://dx.doi.org/10.1007/s10854-018-8689-9>
- [49] REDDY, I.N., REDDY, C.V., SREEDHAR, M., SHIM, J., CHO, M. and KIM, D. Effect of ball milling on optical properties and visible photocatalytic activity of Fe doped ZnO nanoparticles. *Materials Science and Engineering B: Solid-State Materials for Advanced Technology*

- [online]. 2019, **240**(January), 33–40. ISSN 09215107. Available at: <https://doi.org/10.1016/j.mseb.2019.01.002>
- [50] NEOGI, S.K., AHMED, M.A., BANERJEE, A. and BANDYOPADHYAY, S. Enhanced ferromagnetism by ion irradiation for substitutionally cobalt doped ZnO films. *Applied Surface Science* [online]. 2019, **481**(March), 443–453. ISSN 01694332. Available at: <https://doi.org/10.1016/j.apsusc.2019.03.151>
- [51] SAMANTA, A., GOSWAMI, M.N. and MAHAPATRA, P.K. Magnetic and electric properties of Ni-doped ZnO nanoparticles exhibit diluted magnetic semiconductor in nature. *Journal of Alloys and Compounds* [online]. 2018, **730**, 399–407. ISSN 09258388. Available at: <https://doi.org/10.1016/j.jallcom.2017.09.334>
- [52] MAHMOUD, A., ECHABAANE, M., OMRI, K., EL MIR, L. and BEN CHAABANE, R. Development of an impedimetric non enzymatic sensor based on ZnO and Cu doped ZnO nanoparticles for the detection of glucose. *Journal of Alloys and Compounds* [online]. 2019, **786**, 960–968. ISSN 09258388. Available at: <https://doi.org/10.1016/j.jallcom.2019.02.060>
- [53] QIAN, L., ZHENG, Y., CHOUDHURY, K.R., BERA, D., SO, F., XUE, J. and HOLLOWAY, P.H. Electroluminescence from light-emitting polymer/ZnO nanoparticle heterojunctions at sub-bandgap voltages. *Nano Today* [online]. 2010, **5**(5), 384–389. ISSN 17480132.
- [54] BEEK, W.J.E., WIENK, M.M. and JANSSEN, R.A.J. Efficient Hybrid Solar Cells from Zinc Oxide Nanoparticles and a Conjugated Polymer. *Advanced Materials* [online]. 2004, **16**(12), 1009–1013. ISSN 0935-9648.
- [55] BHATIA, S., VERMA, N. and BEDI, R.K. Ethanol gas sensor based upon ZnO nanoparticles prepared by different techniques. *Results in Physics* [online]. 2017, **7**, 801–806. ISSN 22113797. Available at: <https://doi.org/10.1016/j.rinp.2017.02.008>
- [56] MOHANTA, A., SIMMONS, J.G., EVERITT, H.O., SHEN, G., MARGARET KIM, S. and KUNG, P. Effect of pressure and Al doping on structural and optical properties of ZnO nanowires synthesized by chemical vapor deposition. *Journal of Luminescence* [online]. 2014, **146**, 470–474. ISSN 00222313. Available at: <http://dx.doi.org/10.1016/j.jlumin.2013.10.028>
- [57] BERNARDO, M.S., VILLANUEVA, P.G., JARDIEL, T., CALATAYUD, D.G., PEITEADO, M. and CABALLERO, A.C. Ga-doped ZnO self-assembled nanostructures obtained by microwave-assisted hydrothermal synthesis: Effect on morphology and optical properties. *Journal of Alloys and Compounds* [online]. 2017, **722**, 920–927. ISSN 09258388. Available at: <http://dx.doi.org/10.1016/j.jallcom.2017.06.160>
- [58] YANG, Q., LOU, L. and WANG, G. Optical properties of indium doped ZnO planar superlattice nanoribbons. *Physica E: Low-Dimensional Systems*

- and Nanostructures* [online]. 2017, **89**(November 2016), 124–129. ISSN 13869477. Available at: <http://dx.doi.org/10.1016/j.physe.2017.02.011>
- [59] CHEN, Z., YAN, Q., ZHAO, Y., CAO, M., WANG, J. and WANG, L. The structure and the optical-electrical properties of the ZnO films and the Al:ZnO/N: ZnO homojunction photodiode. *Journal of Sol-Gel Science and Technology* [online]. 2019, **91**(1), 101–110. ISSN 15734846. Available at: <http://dx.doi.org/10.1007/s10971-019-04993-6>
- [60] LIU, H., WANG, X., LI, M., YU, S. and ZHENG, R. Optical and electrical properties of Al doped ZnO thin film with preferred orientation in situ grown at room temperature. *Ceramics International* [online]. 2019, **45**(11), 14347–14353. ISSN 02728842. Available at: <https://doi.org/10.1016/j.ceramint.2019.04.149>
- [61] AYDIN, H., YAKUPHANOGLU, F. and AYDIN, C. Al-doped ZnO as a multifunctional nanomaterial: Structural, morphological, optical and low-temperature gas sensing properties. *Journal of Alloys and Compounds* [online]. 2019, **773**, 802–811. ISSN 09258388.
- [62] HJIRI, M., EL MIR, L., LEONARDI, S.G., PISTONE, A., MAVILIA, L. and NERI, G. Al-doped ZnO for highly sensitive CO gas sensors. *Sensors and Actuators, B: Chemical* [online]. 2014, **196**, 413–420. ISSN 09254005. Available at: <http://dx.doi.org/10.1016/j.snb.2014.01.068>
- [63] SONG, J., LIU, S., YANG, C., WANG, G., TIAN, H., ZHAO, Z. jian, MU, R. and GONG, J. The role of Al doping in Pd/ZnO catalyst for CO₂ hydrogenation to methanol. *Applied Catalysis B: Environmental* [online]. 2020, **263**(November 2019), 118367. ISSN 09263373. Available at: <https://doi.org/10.1016/j.apcatb.2019.118367>
- [64] JIANG, X., SONG, Z., LIU, G., MA, Y., WANG, A., GUO, Y. and DU, Z. AgNWs/AZO composite electrode for transparent inverted ZnCdSeS/ZnS quantum dot light-emitting diodes. *Nanotechnology* [online]. 2020, **31**(5). ISSN 13616528.
- [65] DINESHA, M.L., JAYANNA, H.S., ASHOKA, S. and CHANDRAPPA, G.T. Temperature dependent electrical conductivity of Fe doped ZnO nanoparticles prepared by solution combustion method. *Journal of Alloys and Compounds* [online]. 2009, **485**(1–2), 538–541. ISSN 09258388.
- [66] CICILIATI, M.A., SILVA, M.F., FERNANDES, D.M., DE MELO, M.A.C., HECHENLEITNER, A.A.W. and PINEDA, E.A.G. Fe-doped ZnO nanoparticles: Synthesis by a modified sol-gel method and characterization. *Materials Letters* [online]. 2015, **159**, 84–86. ISSN 18734979.
- [67] JEYACHITRA, R., SENTHILNATHAN, V. and SENTHIL, T.S. Studies on electrical behavior of Fe doped ZnO nanoparticles prepared via co-precipitation approach for photo-catalytic application. *Journal of Materials Science: Materials in Electronics* [online]. 2018, **29**(2), 1189–1197. ISSN 1573482X. Available at: <http://dx.doi.org/10.1007/s10854-017->

- [68] MESHKI, M., BEHPOUR, M. and MASOUM, S. Application of Fe doped ZnO nanorods-based modified sensor for determination of sulfamethoxazole and sulfamethizole using chemometric methods in voltammetric studies. *Journal of Electroanalytical Chemistry* [online]. 2015, **740**, 1–7. ISSN 15726657. Available at: <http://dx.doi.org/10.1016/j.jelechem.2014.12.008>
- [69] IQBAL, J., JAN, T., RONGHAI, Y., NAQVI, S.H. and AHMAD, I. Doping Induced Tailoring in the Morphology, Band-Gap and Ferromagnetic Properties of Biocompatible ZnO Nanowires, Nanorods and Nanoparticles. *Nano-Micro Letters* [online]. 2014, **6**(3), 242–251. ISSN 21505551.
- [70] HASSANIEN, A.S., AKL, A.A. and SÁAEDI, A.H. Synthesis, crystallography, microstructure, crystal defects, and morphology of BixZn1-xO nanoparticles prepared by sol-gel technique. *CrystEngComm* [online]. 2018, **20**(12), 1716–1730. ISSN 14668033. Available at: <http://dx.doi.org/10.1039/C7CE02173A>
- [71] OVHAL, M.M., SANTHOSH KUMAR, A., KHULLAR, P., KUMAR, M. and ABHYANKAR, A.C. Photoluminescence quenching and enhanced spin relaxation in Fe doped ZnO nanoparticles. *Materials Chemistry and Physics* [online]. 2017, **195**, 58–66. ISSN 02540584.
- [72] SINGHAL, A., ACHARY, S.N., TYAGI, A.K., MANNA, P.K. and YUSUF, S.M. Colloidal Fe-doped ZnO nanocrystals: Facile low temperature synthesis, characterization and properties. *Materials Science and Engineering: B* [online]. 2008, **153**(1–3), 47–52. ISSN 09215107. Available at: <http://linkinghub.elsevier.com/retrieve/pii/S0921510708003851>
- [73] WANG, J., WAN, J. and CHEN, K. Facile synthesis of superparamagnetic Fe-doped ZnO nanoparticles in liquid polyols. *Materials Letters* [online]. 2010, **64**(21), 2373–2375. ISSN 0167577X.
- [74] BILECKA, I., LUO, L., DJERDJ, I., ROSSELL, M.D., JAGODIČ, M., JAGLIČIĆ, Z., MASUBUCHI, Y., KIKKAWA, S. and NIEDERBERGER, M. Microwave-Assisted Nonaqueous Sol–Gel Chemistry for Highly Concentrated ZnO-Based Magnetic Semiconductor Nanocrystals. *The Journal of Physical Chemistry C* [online]. 2011, **115**(5), 1484–1495. ISSN 1932-7447.
- [75] SKODA, D., URBANEK, P., SEVCIK, J., MUNSTER, L., ANTOS, J. and KURITKA, I. Microwave-assisted synthesis of colloidal ZnO nanocrystals and their utilization in improving polymer light emitting diodes efficiency. *Materials Science and Engineering B: Solid-State Materials for Advanced Technology* [online]. 2018, **232–235**(December 2017), 22–32. ISSN 09215107. Available at: <https://doi.org/10.1016/j.mseb.2018.10.013>
- [76] SKODA, D., URBANEK, P., SEVCIK, J., MUNSTER, L., NADAZDY, V., CULLEN, D.A., BAZANT, P., ANTOS, J. and KURITKA, I. Colloidal

- cobalt-doped ZnO nanoparticles by microwave-assisted synthesis and their utilization in thin composite layers with MEH-PPV as an electroluminescent material for polymer light emitting diodes. *Organic Electronics* [online]. 2018, **59**(March), 337–348. ISSN 15661199. Available at: <https://doi.org/10.1016/j.orgel.2018.05.037>
- [77] MKAWI, E.M., IBRAHIM, K., ALI, M.K.M., FARRUKH, M.A. and MOHAMED, A.S. The effect of dopant concentration on properties of transparent conducting Al-doped ZnO thin films for efficient Cu₂ZnSnS₄ thin-film solar cells prepared by electrodeposition method. *Applied Nanoscience (Switzerland)* [online]. 2015, **5**(8), 993–1001. ISSN 21905517. Available at: <http://dx.doi.org/10.1007/s13204-015-0400-3>
- [78] MAMAT, M.H., SAHDAN, M.Z., KHUSAIMI, Z., AHMED, A.Z., ABDULLAH, S. and RUSOP, M. Influence of doping concentrations on the aluminum doped zinc oxide thin films properties for ultraviolet photoconductive sensor applications. *Optical Materials* [online]. 2010, **32**(6), 696–699. ISSN 09253467. Available at: <http://dx.doi.org/10.1016/j.optmat.2009.12.005>
- [79] AVADHUT, Y.S., WEBER, J., HAMMARBERG, E., FELDMANN, C. and SCHMEDTAUFDER GÜNNE, J. Structural investigation of aluminium doped ZnO nanoparticles by solid-state NMR spectroscopy. *Physical Chemistry Chemical Physics* [online]. 2012, **14**(33), 11610–11625. ISSN 14639076.
- [80] KELCHTERMANS, A., ELEN, K., SCHELLENS, K., CONINGS, B., DAMM, H., BOYEN, H.G., D’HAEN, J., ADRIAENSENS, P., HARDY, A. and VAN BAEL, M.K. Relation between synthesis conditions, dopant position and charge carriers in aluminium-doped ZnO nanoparticles. *RSC Advances* [online]. 2013, **3**(35), 15254–15262. ISSN 20462069.
- [81] BO, R., ZHANG, F., BU, S., NASIRI, N., DI BERNARDO, I., TRAN-PHU, T., SHRESTHA, A., CHEN, H., TAHERI, M., QI, S., ZHANG, Y., MULMUDI, H.K., LIPTON-DUFFIN, J., GASPERA, E. Della and TRICOLI, A. One-Step Synthesis of Porous Transparent Conductive Oxides by Hierarchical Self-Assembly of Aluminum-Doped ZnO Nanoparticles. *ACS Applied Materials and Interfaces* [online]. 2020, **12**(8), 9589–9599. ISSN 19448252.
- [82] ZHANG, X., WU, J., WANG, J., YANG, Q., ZHANG, B. and XIE, Z. Low-Temperature All-Solution-Processed Transparent Silver Nanowire-Polymer/AZO Nanoparticles Composite Electrodes for Efficient ITO-Free Polymer Solar Cells. *ACS Applied Materials and Interfaces* [online]. 2016, **8**(50), 34630–34637. ISSN 19448252.
- [83] GEDYE, R., SMITH, F., WESTAWAY, K., ALI, H., BALDISERA, L., LABERGE, L. and ROUSELL, J. The use of microwave ovens for rapid organic synthesis. *Tetrahedron Letters* [online]. 1986, **27**(3), 279–282.

ISSN 00404039.

- [84] ZHU, Y.J. and CHEN, F. Microwave-assisted preparation of inorganic nanostructures in liquid phase. *Chemical Reviews* [online]. 2014, **114**(12), 6462–6555. ISSN 15206890.
- [85] HOWE, A.G.R., MIEDZIAK, P.J., MORGAN, D.J., HE, Q., STRASSER, P. and EDWARDS, J.K. One pot microwave synthesis of highly stable AuPd@Pd supported core-shell nanoparticles. *Faraday Discussions* [online]. 2018, **208**, 409–425. ISSN 13645498.
- [86] BLANCO-ANDUJAR, C., ORTEGA, D., SOUTHERN, P., PANKHURST, Q.A. and THANH, N.T.K. High performance multi-core iron oxide nanoparticles for magnetic hyperthermia: Microwave synthesis, and the role of core-to-core interactions. *Nanoscale* [online]. 2015, **7**(5), 1768–1775. ISSN 20403372.
- [87] GARCÍA, S., ZHANG, L., PIBURN, G.W., HENKELMAN, G. and HUMPHREY, S.M. Microwave synthesis of classically immiscible rhodium-silver and rhodium-gold alloy nanoparticles: Highly active hydrogenation catalysts. *ACS Nano* [online]. 2014, **8**(11), 11512–11521. ISSN 1936086X.
- [88] IQBAL, N., KADIR, M.R.A., MAHMOOD, N.H., SALIM, N., FROEMMING, G.R.A., BALAJI, H.R. and KAMARUL, T. Characterization, antibacterial and in vitro compatibility of zinc-silver doped hydroxyapatite nanoparticles prepared through microwave synthesis. *Ceramics International* [online]. 2014, **40**(3), 4507–4513. ISSN 02728842.
- [89] SCHÜTZ, M.B., XIAO, L., LEHNEN, T., FISCHER, T. and MATHUR, S. Microwave-assisted synthesis of nanocrystalline binary and ternary metal oxides. *International Materials Reviews* [online]. 2017, **6608**(December), 1–34. ISSN 0950-6608. Available at: <https://www.tandfonline.com/doi/full/10.1080/09506608.2017.1402158>
- [90] BILECKA, I. and NIEDERBERGER, M. Microwave chemistry for inorganic nanomaterials synthesis. *Nanoscale* [online]. 2010, **2**(8), 1358. ISSN 2040-3364. Available at: <http://xlink.rsc.org/?DOI=b9nr00377k>
- [91] KAPPE, C.O., DALLINGER, D., MURPHREE, S.S. and WARREN, P. Microwave theory. In: *Practical Microwave Synthesis for Organic Chemists* [online]. 2007, p. 11–42. ISBN 978-3-527-32097-4.
- [92] KOZAKOVA, Z., KURITKA, I., KAZANTSEVA, N.E., BABAYAN, V., PASTOREK, M., MACHOVSKY, M., BAZANT, P. and SAHA, P. The formation mechanism of iron oxide nanoparticles within the microwave-assisted solvothermal synthesis and its correlation with the structural and magnetic properties. *Dalton Transactions* [online]. 2015, **44**(48), 21099–21108. ISSN 14779234.
- [93] SERNELIUS, B.E., BERGGREN, K.F., JIN, Z.C., HAMBERG, I. and GRANQVIST, C.G. Band-gap tailoring of ZnO by means of heavy Al doping. *Physical Review B* [online]. 1988, **37**(17), 10244–10248.

ISSN 01631829.

- [94] DJERDJ, I., ARČON, D., JAGLIČIĆ, Z. and NIEDERBERGER, M. Nonaqueous synthesis of metal oxide nanoparticles: Short review and doped titanium dioxide as case study for the preparation of transition metal-doped oxide nanoparticles. *Journal of Solid State Chemistry* [online]. 2008, **181**(7), 1571–1581. ISSN 00224596.
- [95] KANDULNA, R., CHOUDHARY, R.B. and MAJI, P. Ag-doped ZnO Reinforced Polymeric Ag:ZnO/PMMA Nanocomposites as Electron Transporting Layer for OLED Application. *Journal of Inorganic and Organometallic Polymers and Materials* [online]. 2017, **27**(6), 1760–1769. ISSN 15741451.
- [96] MANZHI, P., KUMARI, R., ALAM, M.B., UMAPATHY, G.R., KRISHNA, R., OJHA, S., SRIVASTAVA, R. and SINHA, O.P. Mg-doped ZnO nanostructures for efficient Organic Light Emitting Diode. *Vacuum* [online]. 2019, **166**(November 2018), 370–376. ISSN 0042207X. Available at: <https://doi.org/10.1016/j.vacuum.2018.10.070>
- [97] CHOI, Y.-J., GONG, S.C., PARK, C.-S., LEE, H.-S., JANG, J.G., CHANG, H.J., YEOM, G.Y. and PARK, H.-H. Improved performance of organic light-emitting diodes fabricated on Al-doped ZnO anodes incorporating a homogeneous Al-doped ZnO buffer layer grown by atomic layer deposition. *ACS Applied Materials and Interfaces* [online]. 2013, **5**, 3650–3655. ISSN 1944-8252.
- [98] BUONSANTI, R. and MILLIRON, D.J. Chemistry of doped colloidal nanocrystals. *Chemistry of Materials* [online]. 2013, **25**(8), 1305–1317. ISSN 08974756.
- [99] CHEN, W. *Doped nanomaterials and nanodevices. Vol. 1, Vol. 1.*, Stevenson Ranch: American Scientific Publishers, 2010. ISBN 1588831108 9781588831101 1588831078 9781588831071.
- [100] PHAN, C.M. and NGUYEN, H.M. Role of Capping Agent in Wet Synthesis of Nanoparticles. *Journal of Physical Chemistry A* [online]. 2017, **121**(17), 3213–3219. ISSN 15205215.
- [101] LI, C.C., CHANG, S.J., SU, F.J., LIN, S.W. and CHOU, Y.C. Effects of capping agents on the dispersion of silver nanoparticles. *Colloids and Surfaces A: Physicochemical and Engineering Aspects* [online]. 2013, **419**, 209–215. ISSN 18734359. Available at: <http://dx.doi.org/10.1016/j.colsurfa.2012.11.077>
- [102] WILSON, D. and LANGELL, M.A. XPS analysis of oleylamine/oleic acid capped Fe₃O₄ nanoparticles as a function of temperature. *Applied Surface Science* [online]. 2014, **303**, 6–13. ISSN 01694332. Available at: <http://dx.doi.org/10.1016/j.apsusc.2014.02.006>
- [103] AZAD MALIK, M., O'BRIEN, P. and REVAPRASADU, N. Synthesis of TOPO-capped Mn-doped ZnS and CdS quantum dots. *Journal of Materials Chemistry* [online]. 2001, **11**(9), 2383–2387. ISSN 13645501.

- [104] DLAMINI, N.N., RAJASEKHAR PULLABHOTLA, V.S.R. and REVAPRASADU, N. Synthesis of triethanolamine (TEA) capped CdSe nanoparticles. *Materials Letters* [online]. 2011, **65**(9), 1283–1286. ISSN 0167577X. Available at: <http://dx.doi.org/10.1016/j.matlet.2011.01.050>
- [105] BHAWAWET, N., ESSNER, J.B., ATWOOD, J.L. and BAKER, G.A. On the non-innocence of the imidazolium cation in a rapid microwave synthesis of oleylamine-capped gold nanoparticles in an ionic liquid. *Chemical Communications* [online]. 2018, **54**(54), 7523–7526. ISSN 1364548X.
- [106] CUN, Y., SONG, C., ZHENG, H., WANG, J., MAI, C., LIU, Y., LI, J., YU, D., WANG, J., YING, L., PENG, J. and CAO, Y. Modifying the organic/metal interface *via* solvent vapor annealing to enhance the performance of blue OLEDs. *Journal of Materials Chemistry C* [online]. 2019. ISSN 2050-7526. Available at: <http://xlink.rsc.org/?DOI=C9TC01092K>
- [107] HANEMANN, T. and SZABÓ, D.V. Polymer-nanoparticle composites: From synthesis to modern applications. *Materials* [online]. 2010, **3**(6), 3468–3517. ISSN 19961944.
- [108] CHOI, Y.J., PARK, H.H., GOLLEDGE, S. and JOHNSON, D.C. A study on the incorporation of ZnO nanoparticles into MEH-PPV based organic-inorganic hybrid solar cells. *Ceramics International* [online]. 2012, **38**(SUPPL. 1), S525–S528. ISSN 02728842. Available at: <http://dx.doi.org/10.1016/j.ceramint.2011.05.068>
- [109] FRIEND, R.H., GYMER, R.W., HOLMES, A.B., BURROUGHES, J.H., MARKS, R.N., TALIANI, C., BRADLEY, D.D.C., SANTOS, D.A. Dos, BREDAS, J.L., LOGDLUND, M. and SALANECK, W.R. Electroluminescence in conjugated polymers. *Nature* [online]. 1999, **397**(6715), 121–128. ISSN 00280836.
- [110] HUANG, J., XU, Z., ZHAO, S., LI, Y., ZHANG, F., SONG, L., WANG, Y. and XU, X. Organic/inorganic heterostructures for enhanced electroluminescence. *Solid State Communications* [online]. 2007, **142**(7), 417–420. ISSN 00381098.
- [111] LUKA, G., NITTLER, L., LUSAKOWSKA, E. and SMERTENKO, P. Electrical properties of zinc oxide – Tetracene heterostructures with different n-type ZnO films. *Organic Electronics: physics, materials, applications* [online]. 2017, **45**, 240–246. ISSN 15661199. Available at: <http://dx.doi.org/10.1016/j.orgel.2017.03.031>
- [112] NIKHIL, PANDEY, R.K., SAHU, P.K., SINGH, M.K. and PRAKASH, R. Fast grown self-assembled polythiophene/graphene oxide nanocomposite thin films at air-liquid interface with high mobility used in polymer thin film transistors. *Journal of Materials Chemistry C* [online]. 2018, **6**(37), 9981–9989. ISSN 20507526.
- [113] PETRELLA, A., CURRI, M.L., STRICCOLI, M., AGOSTIANO, A. and

- COSMA, P. Photoelectrochemical properties of ZnO nanocrystals/MEH-PPV composite: The effects of nanocrystals synthetic route, film deposition and electrolyte composition. *Thin Solid Films* [online]. 2015, **595**, 157–163. ISSN 00406090. Available at: <http://dx.doi.org/10.1016/j.tsf.2015.10.077>
- [114] BANO, N., ZAMAN, S., ZAINELABDIN, A., HUSSAIN, S., HUSSAIN, I., NUR, O. and WILLANDER, M. ZnO-organic hybrid white light emitting diodes grown on flexible plastic using low temperature aqueous chemical method. *Journal of Applied Physics* [online]. 2010, **108**(4), 1–6. ISSN 00218979.
- [115] WRIGHT, M. and UDDIN, A. Organic-inorganic hybrid solar cells: A comparative review. *Solar Energy Materials and Solar Cells* [online]. 2012, **107**, 87–111. ISSN 09270248. Available at: <http://dx.doi.org/10.1016/j.solmat.2012.07.006>
- [116] HEWIDY, D., GADALLAH, A.S. and FATTAH, G.A. Hybrid electroluminescent device based on MEH-PPV and ZnO. *Physica B: Condensed Matter* [online]. 2017, **507**(September 2016), 46–50. ISSN 09214526.
- [117] WILLANDER, M., NUR, O., ZAMAN, S., ZAINELABDIN, A., BANO, N. and HUSSAIN, I. Zinc oxide nanorods/polymer hybrid heterojunctions for white light emitting diodes. *Journal of Physics D: Applied Physics* [online]. 2011, **44**(22), 224017. ISSN 0022-3727.
- [118] AYDN, C., ABD EL-SADEK, M.S., ZHENG, K., YAHIA, I.S. and YAKUPHANOGLU, F. Synthesis, diffused reflectance and electrical properties of nanocrystalline Fe-doped ZnO via sol-gel calcination technique. *Optics and Laser Technology* [online]. 2013, **48**, 447–452. ISSN 00303992.
- [119] CHO, S., JUNG, S.H. and LEE, K.H. Morphology-controlled growth of ZnO nanostructures using microwave irradiation: From basic to complex structures. *Journal of Physical Chemistry C* [online]. 2008, **112**(33), 12769–12776. ISSN 19327447.
- [120] YIN, J., GAO, F., WEI, C. and LU, Q. Water Amount Dependence on Morphologies and Properties of ZnO nanostructures in Double-solvent System. *Scientific Reports* [online]. 2014, **4**, 1–7. ISSN 20452322.
- [121] BILECKA, I. and NIEDERBERGER, M. New developments in the nonaqueous and/or non-hydrolytic sol-gel synthesis of inorganic nanoparticles. *Electrochimica Acta* [online]. 2010, **55**(26), 7717–7725. ISSN 00134686.
- [122] SAHOO, T., KIM, M., BAEK, J.H., JEON, S.R., KIM, J.S., YU, Y.T., LEE, C.R. and LEE, I.H. Synthesis and characterization of porous ZnO nanoparticles by hydrothermal treatment of as pure aqueous precursor. *Materials Research Bulletin* [online]. 2011, **46**(4), 525–530. ISSN 00255408. Available at: <http://dx.doi.org/10.1016/j.materresbull.2011.01.002>

- [123] MEMAR, A., PHAN, C.M. and TADE, M.O. Controlling particle size and photoelectrochemical properties of nanostructured WO₃ with surfactants. *Applied Surface Science* [online]. 2014, **305**, 760–767. ISSN 01694332. Available at: <http://dx.doi.org/10.1016/j.apsusc.2014.03.194>
- [124] ZHANG, Y., SHAH, T., DEEPAK, F.L. and KORGEL, B.A. Surface Science and Colloidal Stability of Double-Perovskite Cs₂AgBiBr₆ Nanocrystals and Their Superlattices. *Chemistry of Materials* [online]. 2019, **31**(19), 7962–7969. ISSN 15205002.
- [125] GYERGYEK, S., MAKOVEC, D. and DROFENIK, M. Colloidal stability of oleic- and ricinoleic-acid-coated magnetic nanoparticles in organic solvents. *Journal of Colloid and Interface Science* [online]. 2011, **354**(2), 498–505. ISSN 00219797.
- [126] ANŽLOVAR, A., KOGEJ, K., OREL, Z.C. and ŽIGON, M. Impact of inorganic hydroxides on ZnO nanoparticle formation and morphology. *Crystal Growth and Design* [online]. 2014, **14**(9), 4262–4269. ISSN 15287505.
- [127] SHARIFI DEHSARI, H., HALDA RIBEIRO, A., ERSÖZ, B., TREMEL, W., JAKOB, G. and ASADI, K. Effect of precursor concentration on size evolution of iron oxide nanoparticles. *CrystEngComm* [online]. 2017, **19**(44), 6694–6702. ISSN 14668033.
- [128] KIM, K. Do, CHOI, D.W., CHOA, Y.H. and KIM, H.T. Optimization of parameters for the synthesis of zinc oxide nanoparticles by Taguchi robust design method. *Colloids and Surfaces A: Physicochemical and Engineering Aspects* [online]. 2007, **311**(1–3), 170–173. ISSN 09277757.
- [129] MANZHI, P., ALAM, M.B., KUMARI, R., KRISHNA, R., SINGH, R.K., SRIVASTAVA, R. and SINHA, O.P. Li-doped ZnO nanostructures for the organic light emitting diode application. *Vacuum* [online]. 2017, **146**, 462–467. ISSN 0042207X. Available at: <https://doi.org/10.1016/j.vacuum.2017.07.018>
- [130] CHEN, G., LIU, F., LING, Z., ZHANG, P., WEI, B. and ZHU, W. Efficient organic light emitting diodes using solution-processed alkali metal carbonate doped ZnO as electron injection layer. *Frontiers in Chemistry* [online]. 2019, **7**(MAR), 1–9. ISSN 22962646.
- [131] JAMATIA, T., SKODA, D., URBANEK, P., SEVCIK, J., MASLIK, J., MUNSTER, L., KALINA, L. and KURITKA, I. Microwave-assisted synthesis of Fe_xZn_{1-x}O nanoparticles for use in MEH-PPV nanocomposites and their application in polymer light-emitting diodes. *Journal of Materials Science: Materials in Electronics* [online]. 2019. ISSN 0957-4522. Available at: <http://link.springer.com/10.1007/s10854-019-01473-z>
- [132] JAYATHILAKE, D.S.Y., PEIRIS, T.A.N., SAGU, J.S., POTTER, D.B., WIJAYANTHA, K.G.U., CARMALT, C.J. and SOUTHEE, D.J. Microwave-Assisted Synthesis and Processing of Al-Doped, Ga-Doped,

- and Al, Ga Codoped ZnO for the Pursuit of Optimal Conductivity for Transparent Conducting Film Fabrication. *ACS Sustainable Chemistry and Engineering* [online]. 2017, **5**(6), 4820–4829. ISSN 21680485.
- [133] SOUSA, D.M., ALVES, L.C., MARQUES, A., GASPAR, G., LIMA, J.C. and FERREIRA, I. Facile Microwave-assisted Synthesis Manganese Doped Zinc Sulfide Nanoparticles. *Scientific Reports* [online]. 2018, **8**(1), 1–7. ISSN 20452322.
- [134] LU, C.H., BHATTACHARJEE, B. and CHEN, S.Y. Microwave synthesis of manganese-ion-doped zinc sulfide nano-phosphors using a novel monomer. *Journal of Alloys and Compounds* [online]. 2009, **475**(1–2), 116–121. ISSN 09258388.
- [135] MIRZAEI, A. and NERI, G. Microwave-assisted synthesis of metal oxide nanostructures for gas sensing application: A review. *Sensors and Actuators, B: Chemical* [online]. 2016, **237**, 749–775. ISSN 09254005. Available at: <http://dx.doi.org/10.1016/j.snb.2016.06.114>
- [136] MEULENKAMP, E.A. Synthesis and Growth of ZnO Nanoparticles [online]. 1998, **5647**(98), 5566–5572.
- [137] MA, Y., CHOI, T.W., CHEUNG, S.H., CHENG, Y., XU, X., XIE, Y.M., LI, H.W., LI, M., LUO, H., ZHANG, W., SO, S.K., CHEN, S. and TSANG, S.W. Charge transfer-induced photoluminescence in ZnO nanoparticles. *Nanoscale* [online]. 2019, **11**(18), 8736–8743. ISSN 20403372.
- [138] RAJA, K., RAMESH, P.S. and GEETHA, D. Spectrochimica Acta Part A : Molecular and Biomolecular Spectroscopy Structural , FTIR and photoluminescence studies of Fe doped ZnO nanopowder by co-precipitation method. *Spectrochimica Acta Part a: Molecular and Biomolecular Spectroscopy* [online]. 2014, **131**, 183–188. ISSN 1386-1425. Available at: <http://dx.doi.org/10.1016/j.saa.2014.03.047>
- [139] COZZOLI, P.D., KORNOWSKI, A. and WELLER, H. Colloidal synthesis of organic-capped ZnO nanocrystals via a sequential reduction-oxidation reaction. *Journal of Physical Chemistry B* [online]. 2005, **109**(7), 2638–2644. ISSN 15206106.
- [140] KHORSAND ZAK, A., ABD. MAJID, W.H., ABRISHAMI, M.E. and YOUSEFI, R. X-ray analysis of ZnO nanoparticles by Williamson-Hall and size-strain plot methods. *Solid State Sciences* [online]. 2011, **13**(1), 251–256. ISSN 12932558.
- [141] JAMATIA, T., SKODA, D., URBANEK, P., MUNSTER, L., SEVCIK, J. and KURITKA, I. Microwave-assisted particle size-controlled synthesis of ZnO nanoparticles and its application in fabrication of PLED device. *Journal of Physics: Conference Series* [online]. 2019, **1310**(1). ISSN 17426596.
- [142] GOH, E.G., XU, X. and MCCORMICK, P.G. Effect of particle size on the UV absorbance of zinc oxide nanoparticles. *Scripta Materialia* [online]. 2014, **78–79**, 49–52. ISSN 13596462.

- [143] BRUS, L.E. Electron-electron and electron-hole interactions in small semiconductor crystallites: The size dependence of the lowest excited electronic state. *The Journal of Chemical Physics* [online]. 1984, **80**(9), 4403–4409. ISSN 00219606.
- [144] NORTON, D.P., HEO, Y.W., IVILL, M.P., IP, K., PEARTON, S.J., CHISHOLM, M.F. and STEINER, T. ZnO: growth, doping and processing. *Materials Today* [online]. 2008, **7**(6), 34–40. Available at: <https://www.sciencedirect.com/science/article/pii/S1369702104002871>
- [145] SRIKANT, V. and CLARKE, D.R. On the optical band gap of zinc oxide. *Journal of Applied Physics* [online]. 1998, **83**(10), 5447–5451. ISSN 00218979.
- [146] SATTLER, K.D. *Handbook of Nanophysics Nanoparticles and Quantum Dots* [online]. B.m.: Taylor & Francis, 2011. ISBN 9781420075458. Available at: <https://www.taylorfrancis.com/books/9780429193163>
- [147] PELANT, I. and VALENTA, J. *Luminescence Spectroscopy of Semiconductors* [online]. Oxford: Oxford University Press, 2012. ISBN 9780191738548.
- [148] MORKOÇ, H. and ÖZGÜR, Ü. *Zinc Oxide: Fundamentals, Materials and Device Technology* [online]. B.m.: Wiley-VCH Verlag GmbH & Co. KGaA, 2009 [accessed. 2020-06-29]. ISBN 9783527408139. Available at: https://www.worldcat.org/title/zinc-oxide-fundamentals-materials-and-device-technology/oclc/474280809&referer=brief_results
- [149] MUSA, I., MASSUYEAU, F., FAULQUES, E. and NGUYEN, T.P. Investigations of optical properties of MEH-PPV/ZnO nanocomposites by photoluminescence spectroscopy. *Synthetic Metals* [online]. 2012, **162**(19–20), 1756–1761. ISSN 03796779.
- [150] URBÁNEK, P., KUŘITKA, I., DANIŠ, S., TOUŠKOVÁ, J. and TOUŠEK, J. Thickness threshold of structural ordering in thin MEH-PPV films. *Polymer (United Kingdom)* [online]. 2014, **55**(16), 4050–4056. ISSN 00323861.
- [151] URBÁNEK, P., KUŘITKA, I., ŠEVČÍK, J., TOUŠKOVÁ, J., TOUŠEK, J., NÁDAŽDY, V., NÁDAŽDY, P., VÉGSÖ, K., ŠIFFALOVIČ, P., RUTSCH, R. and URBÁNEK, M. An experimental and theoretical study of the structural ordering of the PTB7 polymer at a mesoscopic scale. *Polymer* [online]. 2019, **169**(February), 243–254. ISSN 00323861. Available at: <https://linkinghub.elsevier.com/retrieve/pii/S0032386119301880>
- [152] SHANKAR, J.S., ASHOK KUMAR, S., PERIYASAMY, B.K. and NAYAK, S.K. Studies on Optical Characteristics of Multicolor Emitting MEH-PPV/ZnO Hybrid Nanocomposite. *Polymer - Plastics Technology and Engineering* [online]. 2018, **58**(2), 1–10. ISSN 15256111. Available at: <https://doi.org/10.1080/03602559.2018.1466171>
- [153] KAYANI, Z.N., ABBAS, E., SADDIQA, Z., RIAZ, S. and NASEEM, S. Photocatalytic, antibacterial, optical and magnetic properties of Fe-doped

- ZnO nano-particles prepared by sol-gel. *Materials Science in Semiconductor Processing* [online]. 2018, **88**(May), 109–119. ISSN 13698001. Available at: <https://doi.org/10.1016/j.mssp.2018.08.003>
- [154] HASSAN, M.M., KHAN, W., AZAM, A. and NAQVI, A.H. Effect of size reduction on structural and optical properties of ZnO matrix due to successive doping of Fe ions. *Journal of Luminescence* [online]. 2014, **145**(August), 160–166. ISSN 00222313. Available at: <http://dx.doi.org/10.1016/j.jlumin.2013.06.024>
- [155] KANCHANA, S., CHITHRA, M.J., ERNEST, S. and PUSHPANATHAN, K. Violet emission from Fe doped ZnO nanoparticles synthesized by precipitation method. *Journal of Luminescence* [online]. 2016, **176**, 6–14. ISSN 00222313. Available at: <http://dx.doi.org/10.1016/j.jlumin.2015.12.047>
- [156] KARAMAT, S., RAWAT, R.S., LEE, P., TAN, T.L. and RAMANUJAN, R. V. Structural, elemental, optical and magnetic study of Fe doped ZnO and impurity phase formation. *Progress in Natural Science: Materials International* [online]. 2014, **24**(2), 142–149. ISSN 10020071. Available at: <http://dx.doi.org/10.1016/j.pnsc.2014.03.009>
- [157] CHANG, T.-W.F., MUSIKHIN, S., BAKUEVA, L., LEVINA, L., HINES, M.A., CYR, P.W. and SARGENT, E.H. Efficient excitation transfer from polymer to nanocrystals. *Applied Physics Letters* [online]. 2004, **84**(21), 4295–4297. ISSN 0003-6951.
- [158] PIENKA, M., DYAKONOV, V., MEISSNER, D., ROGACH, A., TALAPIN, D., WELLER, H., LUTSEN, L. and VANDERZANDE, D. Photoinduced charge transfer in composites of conjugated polymers and semiconductor nanocrystals. *Nanotechnology* [online]. 2004, **15**(1), 163–170. ISSN 09574484.
- [159] MALLIKA, A.N., RAMACHANDRAREDDY, A., SOWRIBABU, K. and VENUGOPAL REDDY, K. Synthesis and optical characterization of aluminum doped ZnO nanoparticles. *Ceramics International* [online]. 2014, **40**(8 PART A), 12171–12177. ISSN 02728842. Available at: <http://dx.doi.org/10.1016/j.ceramint.2014.04.057>
- [160] KUMAR, R.S., SATHYAMOORTHY, R., SUDHAGAR, P., MATHESWARAN, P., HRUDHYA, C.P. and KANG, Y.S. Effect of aluminum doping on the structural and luminescent properties of ZnO nanoparticles synthesized by wet chemical method. *Physica E: Low-Dimensional Systems and Nanostructures* [online]. 2011, **43**(6), 1166–1170. ISSN 13869477. Available at: <http://dx.doi.org/10.1016/j.physe.2011.01.022>
- [161] HARTNER, S., ALI, M., SCHULZ, C., WINTERER, M. and WIGGERS, H. Electrical properties of aluminum-doped zinc oxide (AZO) nanoparticles synthesized by chemical vapor synthesis. *Nanotechnology* [online]. 2009, **20**(44). ISSN 09574484.

- [162] PARHOODEH, S., ZARGAR SHOUSHARI, M. and FARBOD, M. Efficient absorption of H₂S by aluminum doped zinc oxide nanoparticles. *Materials Letters* [online]. 2012, **78**, 188–191. ISSN 0167577X. Available at: <http://dx.doi.org/10.1016/j.matlet.2012.03.039>
- [163] ECHRESH, A. and ZARGAR SHOUSHARI, M. Synthesis of Al-doping ZnO nanoparticles via mechanochemical method and investigation of their structural and optical properties. *Materials Letters* [online]. 2013, **109**, 88–91. ISSN 0167577X. Available at: <http://dx.doi.org/10.1016/j.matlet.2013.07.059>
- [164] SEVCIK, J., URBANEK, P., DAVID, S., JAMATIA, T., NADAZDY, V., URBANEK, M., ANTOS, J., MUNSTER, L. and KURITKA, I. Role of aluminum-doped ZnO nanoparticles in thin nanocomposite active layer in fabrication of green/yellow and orange polymer LED. *To be submitted*. 2020.
- [165] LUO, L., ROSSELL, M.D., XIE, D., ERNI, R. and NIEDERBERGER, M. Microwave-assisted nonaqueous sol-gel synthesis: From Al:ZnO nanoparticles to transparent conducting films. *ACS Sustainable Chemistry and Engineering* [online]. 2013, **1**(1), 152–160. ISSN 21680485.
- [166] LU, J.G., FUJITA, S., KAWAHARAMURA, T., NISHINAKA, H., KAMADA, Y., OHSHIMA, T., YE, Z.Z., ZENG, Y.J., ZHANG, Y.Z., ZHU, L.P., HE, H.P. and ZHAO, B.H. Carrier concentration dependence of band gap shift in n-type ZnO:Al films. *Journal of Applied Physics* [online]. 2007, **101**(8). ISSN 00218979.
- [167] MRIDHA, S. and BASAK, D. Aluminium doped ZnO films: Electrical, optical and photoresponse studies. *Journal of Physics D: Applied Physics* [online]. 2007, **40**(22), 6902–6907. ISSN 00223727.
- [168] WANG, Z.G., ZU, X.T., ZHU, S. and WANG, L.M. Green luminescence originates from surface defects in ZnO nanoparticles. *Physica E: Low-Dimensional Systems and Nanostructures* [online]. 2006, **35**(1), 199–202. ISSN 13869477.
- [169] JANOTTI, A. and VAN DE WALLE, C.G. Fundamentals of zinc oxide as a semiconductor. *Reports on Progress in Physics* [online]. 2009, **72**(12). ISSN 00344885.
- [170] ŠEVČÍK, J. *Preparation and characterisation of nanocomposite thin films applicable in organic electronics* [online]. B.m., 2019. Tomas Bata University in Zlin. Available at: http://digilib.k.utb.cz/bitstream/handle/10563/45889/ševčík_2019_teze.pdf?sequence=4&isAllowed=y
- [171] QIAN, L., ZHENG, Y., CHOUDHURY, K.R., BERA, D., SO, F., XUE, J. and HOLLOWAY, P.H. Electroluminescence from light-emitting polymer/ZnO nanoparticle heterojunctions at sub-bandgap voltages. *Nano Today* [online]. 2010, **5**(5), 384–389. ISSN 17480132. Available at: <http://dx.doi.org/10.1016/j.nantod.2010.08.010>

[172] ZHAO, S.L., KAN, P.Z., XU, Z., KONG, C., WANG, D.W., YAN, Y. and WANG, Y.S. Electroluminescence of ZnO nanorods/MEH-PPV heterostructure devices. *Organic Electronics: physics, materials, applications* [online]. 2010, **11**(5), 789–793. ISSN 15661199. Available at: <https://www.sciencedirect.com/science/article/pii/S1566119910000315?via%3Dihub>

LIST OF TABLES

Table 3.1 Scheme of reactions to study the role of water and oleic acid.	26
Table 3.2 Reaction scheme of ZnO nanoparticles at varied ZnO molar precursor concentrations.	28
Table 3.3 ZnO nanoparticles synthesis doped with Fe, Al and dopants.	29
Table 4.1 Average particle size and band gaps of different ZnO samples.	34
Table 4.2 DLS analysis, average particle size and crystallite size of ZnO samples.	42
Table 4.3 Correlation of band gap (from Tauc plot), average particle size (TEM) of ZnO samples.	45
Table 4.4 Band gap values, absorption maxima peaks and emission maxima peaks as calculated from Brus equation.	47
Table 4.5 Table showing the experimental values for comparison with Brus equation prediction.	48
Table 4.6 Contents of Zn and Fe according to the synthesis protocol and concentration of Fe in the product as calculated from precursor content and as measured by EDS [131].	53
Table 4.7 Zeta average and polydispersity index, average crystallite and particle size of ZnO and $\text{Fe}_x\text{Zn}_{1-x}\text{O}$ nanoparticle dispersions [131].	54
Table 4.8 Corelation between average particle size and band gap of ZnO and Fe-ZnO [131].	57
Table 4.9 De-convoluted $\text{Fe}^{2+}/\text{Fe}^{3+}$ peak positions at the binding energy (BE) scale [131].	60
Table 4.10 Al concentration calculated from amounts of reaction precursors in comparison with Al-dopant concentration as obtained from EDS analysis.	65
Table 4.11 Hydrodynamic diameter, PdI and average particle size of Al-doped ZnO samples as estimated by XRD and TEM.	65
Table 4.12 Comparison of average particle size and bandgaps of undoped ZnO and Al-doped ZnO at different dopant concentrations.	69

LIST OF FIGURES

Fig. 1.1 Colloidal Au nanoparticle with different particle sizes [1].....	5
Fig. 1.2 Top-down and bottom-up approaches of nanoparticle synthesis [26].	7
Fig. 1.3 Difference between conventional and MW-heated reaction as a function of time ($t_1 \ll t_2$) [89].	12
Fig. 1.4 (a) Dipolar heating mechanism (b) ionic heating mechanism [91].	13
Fig. 1.5 Illustration of the increase in band gap in nanometre range.	14
Fig. 1.6 Molecular structure of MEH-PPV.	16
Fig. 3.1 Molecular structure of oleic acid.	27
Fig. 3.2 Schematic diagram of Fe-doped ZnO PLED device [131].	30
Fig. 4.1 XRD diffractogram of ZnO nanoparticles.	32
Fig. 4.2 Analysis of water and oleic acid on different ZOA and ZNP samples observed in TEM images.	33
Fig. 4.3 DRUV-Vis of powdered ZnO nanoparticles in different reaction conditions.	34
Fig. 4.4 Tauc plot of ZNP and ZOA powdered sample.	35
Fig. 4.5 Normalised room temperature PL emission spectra of pure ZnO samples.	36
Fig. 4.6 FT-IR of ZnO nanoparticles in MIR region.	37
Fig. 4.7 FT-IR spectra of ZnO ZNP and ZOA samples in FIR (far infrared) region.	37
Fig. 4.8 XRD peaks of ZnO-1, ZnO-2, ZnO-3 and ZnO-4 [141].	38
Fig. 4.9 TEM micrographs of ZnO samples [141].	39
Fig. 4.10 DLS of ZnO-1 colloidal dispersion (graphical output as obtained from the dedicated original data processing software).	40
Fig. 4.11 DLS of ZnO-2 colloid (graphical output as obtained from the dedicated original data processing software).	41
Fig. 4.12 DLS of ZnO-3 dispersion (graphical output as obtained from the dedicated original data processing software).	41
Fig. 4.13 DLS of colloidal dispersion of ZnO-4 (graphical output as obtained from the dedicated original data processing software).	42
Fig. 4.14 TGA of ZnO- 2.	43
Fig. 4.15 UV-Vis absorption spectra of colloidal ZnO samples (inset: normalised curve) [141].	44
Fig. 4.16 Tauc plot of ZnO powdered samples [141].	44

Fig. 4.17 Room-temperature fluorescence spectra of ZnO colloidal samples (inset: normalised peaks) [141].	45
Fig. 4.18 Room temperature PL of ZnO/MEH-PPV nanocomposites and MEH-PPV [141].	48
Fig. 4.19 XRD diffractogram of ZnO and Fe-ZnO nanoparticles [131].	50
Fig. 4.20 TEM micrograph of Fe-ZnO samples [131].	51
Fig. 4.21 TGA/DSC graph of Fe-10 Z [131].	52
Fig. 4.22 FT-IR of Fe-ZnO powdered samples [131].	52
Fig. 4.23 DLS size distribution by the intensity of Fe-1 Z nanoparticles dispersed in toluene. (graphical output as obtained from the dedicated original data processing software) [131].	54
Fig. 4.24 DLS size distribution by the intensity of Fe-5 Z nanoparticles dispersed in toluene. (graphical output as obtained from the dedicated original data processing software) [131].	55
Fig. 4.25 DLS size distribution by the intensity of Fe-10 Z nanoparticles dispersed in toluene. (graphical output as obtained from the dedicated original data processing software) [131].	55
Fig. 4.26 UV-Vis spectra of pure and F-ZnO colloids [131].	56
Fig. 4.27 Tauc plot and DRUV-Vis of ZnO and Fe-ZnO powders [131].	57
Fig. 4.28 Fluorescence spectra of ZnO and Fe-doped ZnO colloids [131].	58
Fig. 4.29 Narrow scan XPS core spectra of Fe 2p of the $Fe_xZn_{1-x}O$, sample $x=0.0$ [131].	59
Fig. 4.30 Narrow scan XPS core spectra of Fe 2p of the $Fe_xZn_{1-x}O$, sample, $x=0.05$ [131].	60
Fig. 4.31 Narrow scan XPS core spectra of Zn $2p_{3/2}$ of the $Fe_xZn_{1-x}O$ samples (a) $x = 0.01$, (b) $x = 0.05$ and (c) $x = 0.1$ [131].	61
Fig. 4.32 Room temperature PL spectra of pure MEH-PPV, ZnO/MEHPPV and $Fe_xZn_{1-x}O$ /MEH-PPV nanocomposites [131].	62
Fig. 4.33 XRD peaks of ZnO and Al-ZnO powders [164].	63
Fig. 4.34 TEM micrograph of undoped ZnO and Al-doped ZnO nanoparticles dispersed in toluene.	64
Fig. 4.35 DLS of Al- 1Z colloidal sample (graphical output as obtained from the dedicated original data processing software)	66
Fig. 4.36 DLS of Al- 5Z colloidal dispersion (graphical output as obtained from the dedicated original data processing software)	66
Fig. 4.37 DLS of Al- 10Z colloid (graphical output as obtained from the dedicated original data processing software)	67

Fig. 4.38 TGA of Al-1Z powdered sample.	67
Fig. 4.39 FT-IR of Al-doped ZnO powder.	68
Fig. 4.40 UV-Vis spectra of ZnO and Al-ZnO colloids, inset: normalised data [164].	69
Fig. 4.41 Band gap calculation of ZnO and Al-ZnO powder using Tauc plot; inset, DRUV-Vis of ZnO and Al-doped samples [164].	70
Fig. 4.42 Room temperature PL spectra of pure and Al-doped ZnO colloids [164].	71
Fig. 4.43 PL spectra of neat MEH-PPV and Al- ZME nanocomposites [164]. ...	71
Fig. 4.44 Luminance of two pixels of ZnO-3/MEH-PPV PLED device at 10 V.	72
Fig. 4.45 (a) Chromaticity diagram (CIE 1931) of PLED devices fabricated with neat MEH-PPV, (b) magnified region the chromatic diagram, and (c) colour spectrum of MEH-PPV diode.	74
Fig. 4.46 Electroluminescence of ZnO/MEH-PPV and neat MEH-PPV diode [170].	75
Fig. 4.47 (a) Colour space representation of neat MEH-PPV and ZnO/MEH-PPV samples, (b) image enlarged from the chromatic plot, and (c) EL spectrum of ZnO/MEH-PPV 1 diode @ 10 V.	76
Fig. 4.48 Electroluminescence of Fe-Z/MEH-PPV, Z/MEH-PPV and MEH-PPV samples [170].	77
Fig. 4.49 (a) CIE 1931 diagram for PLED devices with Fe- Z/MEH-PPV samples as active layer, (b) enlarged image of the chromaticity plot, and (c) EL colour spectrum of the Fe-doped MEH-PPV diodes.	78
Fig. 4.50 Electroluminescence of Al-Z/MEH-PPV, Z/MEH-PPV and MEH-PPV samples [170].	79
Fig. 4.51 (a) The chromatic diagram of MEH-PPV and Al-Z/MEH-PPV samples, (b) expanded image of the chromatic plot, and (c) EL spectrum of Al- Z 1/MEH-PPV diode.	80
Fig. 4.52 Comparison of the best performing PLEDs from each sample series with the reference diode.	81

LIST OF ABBREVIATIONS

BSE	Back scattering electron
CCD	Charged couple device
CVD	Chemical vapour deposition
DEG	Diethylene glycol
DLS	Dynamic light scattering
DRUV-Vis	Diffuse reflectance ultraviolet visible spectroscopy
DSC	Differential scanning calorimetry
EDS	Electron dispersive spectroscopy
EL	Electroluminescence spectroscopy
FT-IR	Fourier-transform infrared spectroscopy
HDA	Hexadecylamine
HOMO	Highest occupied molecular orbital
ITO	Indium tin oxide
I-V	Current-voltage
LUMO	Lowest unoccupied molecular orbital
MEH-PPV	Poly[2-methoxy-5-(2-ethylhexyloxy)-1,4-phenylene vinylene]
NBE	Near-band-edge
OA	Oleic acid
OLED	Organic light-emitting diode
OPV	Organic photovoltaic cell
PEDOT:PSS	poly(3,4-ethylenedioxythiophene) polystyrene sulfonate
PdI	Polydispersity index
PLED	Polymer light-emitting diode
PL	Photoluminescence
PSC	Polymer solar cells
PVA	Polyvinyl alcohol
PVD	Physical vapour deposition

SEM	Scanning electron microscope
TEA	Triethylamine
TEM	Transmission electron microscope
TGA	Thermogravimetric analysis
TOPO	Trioctylphosphine oxide
UV-Vis	Ultraviolet visible spectroscopy
XPS	X-ray photoelectron spectroscopy
XRD	X-ray diffraction

LIST OF SYMBOLS

A	Absorbance
Acac	Acetylacetonate
Å	Angstrom
β	Full-width half maximum
c	Molar concentration
d	Crystallite size
d	Spacing between diffracting planes
d(H)	Hydrodynamic diameter of particles in liquid media
D	Translational diffusion coefficient
ε	Molar absorption coefficient
ε'	Dielectric constant
ε''	Dielectric loss
eV	Electron volt
E	Energy of the incident photon
$E_{g(bulk)}$	band gap energy of the bulk semiconductor
$E_{g(nano)}$	band gap of a semiconductor nanoparticle
$E_{g(tr)}$	energy needed to create the lowest exciton energy
F(R)	Kubelka-Munk function
h	Planck's constant
K	Grain shape dependent
k	Boltzmann's constant
kV	Kilovolt
l	Optical path length
M_w	Molecular weight
mA	Milliampere
mmol	Millimole
m_e^*	effective mass of excited electron

m_h^*	effective mass of excited hole
η	Dynamic viscosity
n_{Zn}	Molar concentration of zinc
n_{Fe}	Molar concentration of iron
n_{Al}	Molar concentration of aluminium
nm	nanometre
OAc	Acetate
O _i	Oxygen interstitial
O _{Zn}	Oxygen substitute in zinc site
R	Absolute reflectance
r	radius of the semiconductor
$\tan \theta$	Loss tangent
T	Absolute temperature
μL	Microlitre
V _O	Oxygen vacancies
V _{Zn}	Zinc vacancies
ν	Frequency of the incident photon
Zn _i	Zinc interstitial
Zn _O	Zinc substitute in oxygen site
λ	Wavelength of the incident X-ray
λ_{max}	Absorption peak maxima

CURRICULUM VITAE

Personal information

Name and surname	Thaiskang Jamatia
Nationality	Indian
Date of birth	6 th October 1990
Address	nám. T. G. Masaryka 3050, 760 01 Zlín
Mobile number	+420 776643431
Email	jamatia@utb.cz

Education

2016-present	Tomas Bata University in Zlín, PhD, Faculty of Technology, Chemistry and Materials Technology, Technology of Macromolecular Compounds
Internship Sept. 2019- Dec. 2019	Freemovers Exchange Program ETH Zurich, Rämistrasse 101, 8092 Zürich, Switzerland
2010-2015	Karunya University, Integrated Masters in Science (MSc), Nanoscience and Technology, Coimbatore, India
2007-2010	Hindi Higher Secondary School Agartala, India

List of projects

- IGA/CPS/2017/008 Preparation and characterization of nanoparticles and thin nanocomposite films made thereof – member of the research team- Project leader.
- IGA/CPS/2018/007 Development and studies of conductive nanocomposite systems applicable in polymer electronics – member of the research team- Member of research team.
- IGA/CPS/2019/007 Development and study of conductive nanocomposite materials for electronic and electrotechnical applications –Member of research team.
- GA19-23647S
(2019-2021) Investigation of Correlation Among cation distribution, particle size and physical properties of intelligent spinel ferrite nanomaterials- Member of research team.

LIST OF PUBLICATIONS

Journal articles

1. Jamatia, T; Skoda, D; Urbanek, P; Sevcik, J; Maslik, J; Munster, L; Kalina, L; Kuritka, I. *Microwave-assisted synthesis of $Fe_xZn_{1-x}O$ nanoparticles for use in MEH-PPV nanocomposites and their application in polymer light-emitting diodes*. Journal of Materials Science: Materials in Electronics (2019) 30:11269–11281. DOI: <https://doi.org/10.1007/s10854-019-01473-z>.
2. Yadav, R. S.; Kuritka, I; Vilcakova, J; Jamatia, T; Machovsky, M; Skoda, D; Urbanek, P; Masar, M; Urbánek, M; Kalina, L; Havlica, J. *Impact of sonochemical synthesis condition on the structural and physical properties of $MnFe_2O_4$ spinel ferrite nanoparticles*. Ultrasonics Chemistry-Volume 61, March 2020, 104839. DOI: <https://doi.org/10.1016/j.ultsonch.2019.104839>.
3. Sevcik, J; Urbanek, P; Skoda, D; Jamatia, T; Nadazdy, V; Urbanek, M; Antos, J; Munster, L; Kuritka, I. Role of aluminum-doped ZnO nanoparticles in thin nanocomposite active layer in fabrication of green/yellow and orange polymer LED. To be submitted. 2020.

International conference proceedings (active presentation)

1. Jamatia, T; Skoda, D; Urbanek, P; Munster, L; Sevcik, J; Kuritka, I. *Tailoring of band gap and optical properties of ZnO nanoparticles by doping with Fe*. In: 22nd International Conference and Expo on Nanoscience and Molecular Nanotechnology, Frankfurt, Germany. DOI: 10.4172/2157-7439-C1-059.
2. Jamatia, T; Skoda, D; Urbanek, P; Munster, L; Sevcik, J; Kuritka, I. *Microwave-assisted particle size-controlled synthesis of ZnO nanocolloids and its application in fabrication of PLED devices*: Applied Nanotechnology and Nanoscience International Conference, Berlin, Germany 2018, Journal of Physics: Conference series. DOI: 10.1088/1742-6596/1310/1/012012

Other conference contributions

3. Ševčík J; Škoda D.; Jamatia T.; Antoš J.; Urbánek P.; Kuřitka I. *Bandgap engineering of ZnO nanoparticles for polymer active layers in leds*: Plastko: sborník příspěvků z konference, 18. - 19. dubna 2018.

4. Ševčík J; Škoda D.; Jamatia T.; Antoš J.; Urbánek P.; Kuřitka I. *ZnO Particle Bandgap Engineering for Polymer Nanocomposites as Active Layers in LEDs*: Polymers : site of advanced horizons and ambits : May 2-4, 2018 Zlín, Czech Republic : P-SAHA 18 UTB.
5. Yadav R. S.; Kuřitka I.; Vilčáková J.; Škoda D.; Urbánek P.; Machovský M.; Jamatia T.; Masař M. *Particle Size, Cation Distribution and Magnetic Properties of Intelligent Spinel Ferrite Nanoparticles and its Application*: 2nd Global Conference on Magnetism and Magnetic Materials (GCMMM-2019), 25-26 July, Rome, Italy.

Thaiskang Jamatia

**Preparation and characterisation of fillers for polymer
nanocomposite layers usable in electronics**

Příprava a charakterizace plniv pro polymerní nanokompozitní vrstvy
využitelné v elektronice

Doctoral Thesis

Print run: printed electronically

Typesetting: Thaiskang Jamatia

This publication did not pass through editorial or stylistic revision.

Year of Publication 2020